

# Fabrication and Measurement of LT-GaAs Photoconductive Antennas and Arrays

A thesis submitted in partial fulfillment  
of the requirements for the degree of  
Master of Science in Electrical Engineering

by

Zachary Paul Uttley  
University of Arkansas  
Bachelor of Science in Electrical Engineering, 2021

August 2023  
University of Arkansas

This thesis is approved for recommendation to the Graduate Council.

---

Magda El-Shenawee, Ph.D.  
Thesis Director

---

Hugh Churchill, Ph.D.  
Committee Member

---

Morgan Ware, Ph.D.  
Committee Member

## Abstract

This thesis presents the fabrication and measurement of LT-GaAs based terahertz (THz) photo conductive antennas (PCAs) and arrays. The LT-GaAs THz PCAs are fabricated to serve as reference devices to new 2D material black phosphorous (BP) based THz PCAs. The LT-GaAs and BP devices have identical metallic electrodes, allowing for a comparison of emitted THz intensity and bandwidth. All PCAs have been measured using an open bench pulsed time-domain spectroscopy (TDS) system with a usable bandwidth from 0.1-4 THz, pumped with a 780nm Ti:Sapphire femtosecond laser. The results have shown LT-GaAs devices outperforming BP devices in signal amplitude and bandwidth at identical DC bias voltages and pump powers. Three other electrode shape designs were achieved: circular, slotted, and fractal, fabricated on LT-GaAs. The effect of electrode shape on the amplitude and bandwidth of the THz pulse has been experimentally characterized. A comparison of all four shapes has shown that the bowtie electrodes provide a nominal increase in pulse amplitude under identical biasing conditions. Further, a polarization study using an x-cut quartz rotator was conducted, validating that all four electrode shapes are highly linearly polarized. Results show that the co-polarized THz pulse is two orders of magnitude greater than the cross-polarized THz pulse. In addition, two element THz PCAs with electrode spacings of 75 $\mu$ m, 150 $\mu$ m, and 300 $\mu$ m have been investigated. A novel feed network using two beam splitters has been designed, and implemented into the existing open bench TDS system. This feed network gives individual control over the position and path length of the beams feeding each elements. Further, a DC bias splitting PCB and switchboard were designed to allow each element to be turned on and off, aiding in laser alignment validation. The measurement of all three devices have shown the array THz pulse having a higher amplitude than either individual element, however, an insignificant effect on the array bandwidth has been observed.

## Acknowledgements

The work presented in this thesis is funded by the National Science Foundation under grant number 1948255. The project title is, “Efficient THz Emission Using Thin Black Phosphorus Photoconductive Absorber and loss-free Dielectric Light Trapping.” The principal investigator (PI) of this project is Dr. Magda El-Shenawee, along with Dr. Hugh Churchill (Co-PI)

I would like to give special thanks to Dr. Magda El-Shenawee, her unwavering focus helped me to see what it takes to succeed. I thank Jose Batista for providing comprehensive training on device measurements, and for always being available when I needed technical advice. I would also like to thank Dr. Hugh Churchill and Dr. Morgan Ware, for serving as members of my committee and providing advice and insight that helped me push through challenges. Without the use of Dr. Hugh Churchill’s lab, the devices fabricated and measured in this work would not have been possible.

I acknowledge and thank my mother and father, Kristy and Paul Uttley, my siblings, Haley Hawn and Carter Uttley, and my close friends Gus Williams, Kyle Gerdes, Adam Fowler, and Anna Fowler for their support, advice, and friendship during the past two years. I also thank my wife, Morgan Burns, for supporting me daily outside of the lab, reminding me to stay focused and work, without her I would never have been able to complete this work.

Finally, I would like to express my gratitude to my colleagues, Bilal Pirzada, and Nikita Gurjar, for aiding in my research when needed. Thank you to Mahmudal Doha, Michael Mastalish, Jeb Stacy, and Shiva Davari for training me on all things fabrication, and providing advice when needed. Thank you to Dr. Mittendorff and Dr. Han of University of Duisburg-Essen for their willingness to perform the pump-probe measurements of the LT-GaAs wafers used in this work.

## Table of Contents

Chapter 1: Introduction .....	1
1.1 Motivation .....	1
1.2 THz Photoconductive Antenna Overview .....	2
1.3 LT-GaAs Carrier Dynamics .....	4
1.4 Black Phosphorous-Based THz PCA .....	5
1.5 PCA Electrode Geometry .....	7
1.6 THz PCA Fabrication Methods .....	9
1.7 Thesis Chapter Roadmap .....	11
Chapter 2: LT-GaAs THz Photoconductive Antenna Fabrication .....	13
2.1 Computer Aided Design (CAD) and Proximity Effect Correction (PEC) .....	13
2.2 LT-GaAs Wafer Growth and Sample Preparation .....	17
2.3 EBL Exposure and Pattern Development .....	24
2.4 Etching Electrode Features .....	37
2.5 Thermal Evaporation and Packaging .....	39
2.6 Fabrication Conclusions .....	46
Chapter 3: TeraAlign System and Device Measurements .....	47
3.1 TeraAlign System Overview .....	47
3.1.1 TeraAlign Component Layout .....	47
3.1.2 TeraAlign PCA Alignment Procedure .....	50

3.2 LT-GaAs THz PCA Voltage and Power Study .....	60
3.3 LT-GaAs THz PCA Polarization Study .....	63
3.4 LT-GaAs THz PCA Electrode Shape Comparison .....	67
3.5 LT-GaAs THz PCA Measurement Summary .....	71
Chapter 4: LT-GaAs THz Array Feed Network and PCA design .....	72
4.1 Antenna Array Background .....	72
4.2 THz PCA Array Feed Network Approaches and Challenges .....	73
4.3 LT-GaAs THz PCA Array Design and Fabrication .....	75
4.4 Beam Splitting Feed Network Design.....	77
4.5 THz PCA Array Alignment Procedure .....	80
4.6 THz PCA Array Measurements .....	83
4.7 THz PCA Array Conclusions.....	90
Chapter 5: Conclusions and Future Work.....	92
Bibliography .....	95
Appendix A: LT-GaAs Optical Pump THz Probe Measurements.....	102
Appendix B: Black Phosphorus THz PCA Measurements.....	106

## List of Figures

Figure 1.2-1: Cross section of THz PCA and Si lens [17].	3
Figure 1.2-2: Conventional THz PCA device structure fabricated on LT-GaAs substrate [18].	4
Figure 1.4-1: Crystal structure diagram of BP showing two distinct crystal directions [17].	6
Figure 1.4-2: BP/hBN THz PCA structure [17].	7
Figure 1.5-1: Electrode-based improvements of THz PCAs [17].	9
Figure 1.6-1: Diagram of typical photolithography process.	10
Figure 1.6-2: Simplified diagram of EBL process.	11
Figure 2.1-1: Bowtie emitter electrodes including dimensions of active area.	13
Figure 2.1-2: Full bowtie THz PCA emitter design, positive (blue), negative (red).	14
Figure 2.1-3: Diagram of overexposure due to proximity effect.	15
Figure 2.1-4: Comparison of PEC and non-PEC devices.	16
Figure 2.1-5: CAD of electrode shapes. (a) bowtie, (b) fractal, (c) slotted, (d) circular.	17
Figure 2.2-1: As grown 2" LT-GaAs wafer used in fabrication of THz PCAs.	19
Figure 2.2-2: Diced section of LT-GaAs wafer, ready to be used in fabrication.	20
Figure 2.2-3: LT-GaAs sample on hot plate.	21
Figure 2.2-4: LT-GaAs sample on vacuum chuck of spin coater.	22
Figure 2.2-5: PMMA A2 and A4 thickness based on spinning speed [52].	23
Figure 2.2-6: PMMA coated LT-GaAs sample.	24
Figure 2.3-1: (a) Main JEOL EBL system. (b) Information status screen.	26
Figure 2.3-2: EBL cassette with LT-GaAs sample held in place for writing.	26
Figure 2.3-3: (a) top edge of the LT-GaAs. (b) bottom edge of the same sample.	27

Figure 2.3-4: (a) reference point located on EBL cassette. (b) example coordinates with respect to center of LT-GaAs sample.....	28
Figure 2.3-5: (a) main EBL software window. (b) EOS adjustment window. ....	30
Figure 2.3-6: Aperture adjustment knob with aperture 1 selected.....	31
Figure 2.3-7: Main stage control screen in EBL user software. ....	31
Figure 2.3-8: Probe current adjustment window showing LENS 2/3 slider. ....	32
Figure 2.3-9: Calibration menu within EBL software. ....	33
Figure 2.3-10: SE image of cassette reference mark used for locating LT-GaAs sample.....	34
Figure 2.3-11: Exposure GUI with various sectioned used during exposure setup labeled. ....	35
Figure 2.3-12: Fully developed EBL patterns. (a) slotted, (b) circular, (c) fractal. ....	36
Figure 2.4-1: Fully metalized bowtie electrodes with fractal etch mask patterned in PMMA. ....	37
Figure 2.4-2: (a) slotted etch mask before etching. (b) over etched slots after 30 seconds. ....	38
Figure 2.4-3: (a) slot results with different etch times. (b) slots etched for 2.5 seconds. ....	39
Figure 2.5-1: Thermal evaporator chuck with top metal finger holding LT-GaAs chip. ....	40
Figure 2.5-2: Inside of thermal evaporator showing 4 material bays. ....	41
Figure 2.5-3: Thermal evaporator chuck holding two metalized LT-GaAs samples. ....	42
Figure 2.5-4: Bond pad of THz PCA showing unwanted metal after lift off. ....	43
Figure 2.5-5: (a) shows the front of the chip carrier with THz PCA mounted on the back, the actual antenna is visible in the center through the hole in the carrier. (b) shows the back, with nail polish adhesive visible around edged of LT-GaAs chip.....	44
Figure 2.5-6: Wire bonds connecting the bond pads of a THz PCA to the chip carrier. ....	45
Figure 3.1-1: Top-down view of entire TeraAlign system showing critical components. ....	48
Figure 3.1-2: (a) simplified diagram of optical side. (b) simplified diagram of THz side. ....	50

Figure 3.1-3: Top-down view of THz side of TeraAlign system. ....	51
Figure 3.1-4: (a) beam splitter and card setup. (b) projected bowtie image. (c) projected circular image. (d) beam diagram for reflection alignment setup.....	52
Figure 3.1-5: Stacked alignment stage with axis knobs for x, y, and z labeled.....	53
Figure 3.1-6: Main TeraPulse software screen showing location of acquisition setup. ....	54
Figure 3.1-7: TestPanel login screen showing connected instrument.....	55
Figure 3.1-8: Expanded measurement config menu with various settings for SlowScan. ....	56
Figure 3.1-9: SlowScan of THz PCA from -100ps to 100ps with pulse occurring around -15ps.	57
Figure 3.1-10: Main measurement screen within TeraPulse software.....	58
Figure 3.1-11: (a) time and frequency domain plots of aligned reference emitter with no pinhole. (b) same emitter and alignment with 1mm pinhole in signal path.....	59
Figure 3.2-1: Normalized pulse amplitude vs laser power from 0.5mW to 6mW.....	61
Figure 3.2-2: Normalized pulse amplitude vs DC bias from 4.2V to 63V .....	62
Figure 3.3-1: Render of experimental setup for polarization study. ....	65
Figure 3.3-2: Polarization data for all four LT-GaAs electrode shapes and commercial emitter.	66
Figure 3.4-1: Time domain and spectrum data from all four electrode shapes including commercial emitter. ....	68
Figure 3.4-2: Simulated surface photocurrent density for all four electrode shapes [18].....	69
Figure 3.4-3: Simulated and experimental results of spectrum, S11, and photocurrent study for all four electrode designs of THz PCAs as reported in [18]. ....	70
Figure 4.3-1: Two element THz PCA array.....	75
Figure 4.3-2: (a) Switch board PCB. (b) Dual bias array PCB.....	76
Figure 4.3-3: CAD model of dual bias voltage array.....	77



Figure 4.4-1: Simulated beam-splitting array feed setup.....	77
Figure 4.4-2: Beam-splitting THz PCA array feed network.....	79
Figure 4.4-3: NIR lens with and without 500mm EFL lens .....	80
Figure 4.5-1: Card reflection during array alignment.....	82
Figure 4.6-1: Time domain and Spectrum of THz PCA Arrays.....	85
Figure 4.6-2: Split bias switch function validation measurements.....	87
Figure 4.6-3: Time domain and Spectrum of Dual Bias THz PCA Arrays.....	89
Figure A-1: Optical Pump THz Probe System Setup.....	102
Figure A-2: LT-GaAs wafer 1 pump-probe results.....	103
Figure A-3: LT-GaAs wafer 2 pump-probe results.....	103
Figure B-1: Time domain and spectrum of BP device 1.....	106
Figure B-2: Time domain and spectrum of BP device 2.....	107
Figure C-1: Time domain and spectrum of THz Arrays.....	107

## **Chapter 1: Introduction**

### **1.1 Motivation**

The THz band is a spectral band that consists of frequencies lying between 100 GHz and 10 THz. This band in the electromagnetic spectrum has historically been investigated far less than its neighboring bands, infrared and optical. In recent years however, the THz band has seen a significant influx in research, leading to the discovery of new and useful applications within the THz band across a wide range of disciplines. The next generation of 6G communication will likely utilize the THz band to facilitate terabit-per-second data transmission [1]–[3]. New THz imaging methods are improving medical imaging, especially in breast cancer tumor margin detection, seeking to improve the success rate of tumor excision and reduce the need for repeat surgeries [4], [5]. Other THz imaging techniques are being used for non-destructive failure analysis of electronics and fault detection in semiconductor materials, which can allow for high-resolution imaging of internal and integrated circuits without the need to destroy the devices being studied [6], [7]. Advances in security, with the ability to sense for dangerous materials like drugs or explosives and identify their make-up is possible with THz spectroscopy, creating safer environments in places where security is top priority, such as airports, large events, and federal buildings [8], [9]. All of the mentioned advances in THz applications share a similar need, that is more efficient THz sources. Current THz antennas exist in many forms, including but not limited to microstrip antennas, horn antennas, lens antennas, and photoconductive antennas (PCA), all of which are prone to high losses, as well as manufacturing defects due to their small size, many devices requiring fabrication of sub-micron features [10]. The challenge of increasing the efficiency, creating phased antenna arrays, as well as improving other characteristics like

directivity and beam steering/shaping drive much of the work being done, due to the integral role that THz antennas will play in the future of THz technology and devices.

In this thesis work, the goal is to fabricate LT-GaAs emitters, such that they can be compared to black phosphorus THz PCAs of an identical electrode design. LT-GaAs is by far the preferred substrate for the fabrication of THz PCAs [11]. The use of LT-GaAs is due to its relative ease in growth, as well as its favorable carrier dynamics, such as sub picosecond carrier lifetime, and high mobility compared to conventionally grown GaAs [12], [13]. The search for new materials to fabricate THz PCAs with is ongoing and motivates the use of BP as a possible photoconductive substrate. Other materials such as InGaAs/InAlAs have been shown to possess similar carrier dynamics to LT-GaAs, and are being investigated for use in both THz emitters and detectors [14]–[16]. In the case of all new materials being studied, the comparison to conventional LT-GaAs emitters I generally made, as it has historically been the standard material used in THz PCAs. For this reason, the main focus of this work is to create LT-GaAs emitters such that a comparison can be made to identical emitters fabricated using BP as the photoconductive substrate.

## **1.2 THz Photoconductive Antenna Overview**

Photoconductive antennas (PCAs) are one of many ways to generate THz frequency radiation. In general, the driving theory behind THz PCAs consists of transforming a femtosecond optical pulse provided by a pump laser, into a coherent THz time-domain pulse through the use of conductive electrodes (conventionally some type of dipole) excited with a DC bias voltage that have been fabricated onto a semiconductor substrate with appropriate carrier dynamics to facilitate the optical-to-THz conversion.

When the optical pulse is incident on the semiconductor material within the gap of the electrodes, free carriers are generated, which are then driven in the DC bias field. This driving of

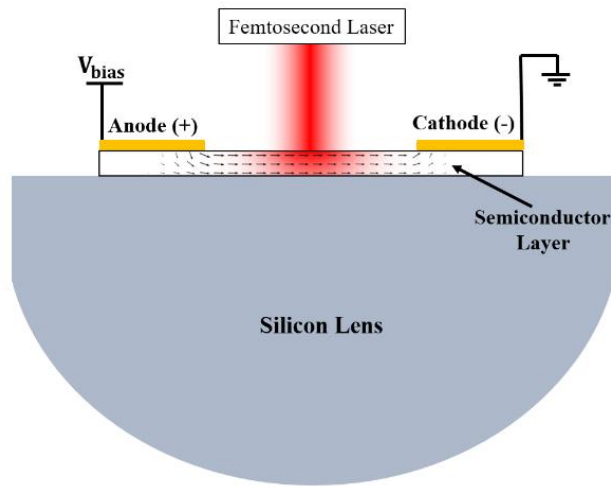


Figure 1.2-1: Cross section of THz PCA and Si lens [17].

free carriers creates a surface current pulse on the semiconductor, which acts as the current source for the antenna. From there, the antenna emits a THz pulse consisting of a wide range of frequencies ( $\sim 0.1$ -6 THz).

The semiconductor material that the THz PCAs are fabricated on must be chosen such that its carrier dynamics meet the requirements for generation of THz radiation. The main characteristic of a semiconductor material that is suitable for use in THz PCA devices, is its carrier lifetime. The semiconductor must have a sub picosecond carrier lifetime in order to ensure that recombination of free carriers does not happen after the optical pulse is fully absorbed by the material, as this effect widens the time-domain pulse, and reduces the overall THz bandwidth of the antennas. While this is one of the most important characteristics of the semiconductor substrate, mobility also plays a key role in determining the performance of the devices in terms of optical to THz efficiency, bandwidth, and signal to noise ratio (SNR) [11]. The most used semiconductor materials for fabricating THz PCAs is Gallium Arsenide (GaAs).

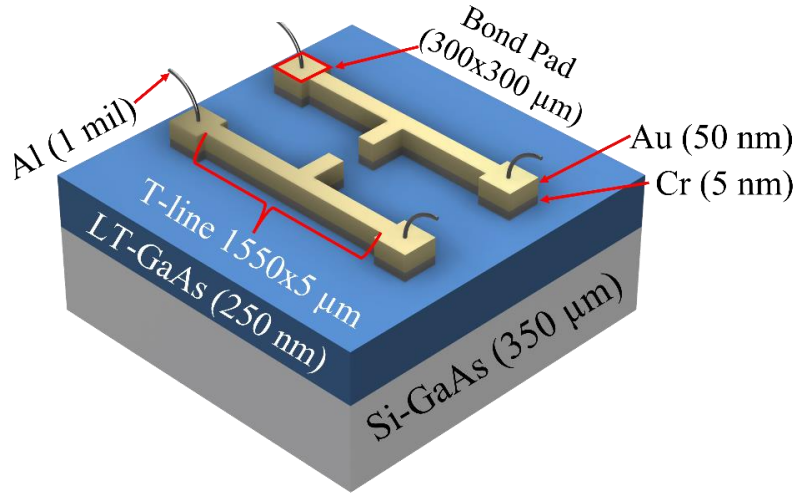


Figure 1.2-2: Conventional THz PCA device structure fabricated on LT-GaAs substrate

[18].

Conventionally, the THz PCA devices consist of a LT-GaAs layer grown on top of Semi Insulating GaAs (SI-GaAs). The antenna electrodes are then fabricated on top of the LT-GaAs layer, where they can later have a DC bias voltage applied via wire bonding to a chip carrier. Above in fig 1.2-2, the full device stack of a LT-GaAs based THz PCA can be seen showing the substrate stack of SI-GaAs and LT-GaAs, as well as the metallic electrode bilayer of Cr/Au.

### 1.3 LT-GaAs Carrier Dynamics

GaAs grown at low temperatures ( $\sim 180\text{-}300^\circ\text{C}$ ), referred to as Low Temperature Gallium Arsenide (LT-GaAs) has been reported by many to have a sub picosecond carrier lifetime as low as 0.4 ps [12], [13], [19], [20]. When growing LT-GaAs, there are two main processes that dictate the majority of the resulting materials carrier dynamics. First, the growth temperature of the material, and second, the anneal temperature and time. When GaAs is grown using molecular beam epitaxy (MBE) at a low temperature with an intentional excess of As flux, the resulting GaAs will contain a 1-2% excess of arsenic [12]. This excess arsenic in the material results in lower resistivity

in the as-grown material due to hopping conduction [21]. In order to recover its high resistivity, an important parameter for THz PCA devices, the material is then annealed at a high temperature (400-1000°C), where the excess arsenic will precipitate out, leaving behind metallic arsenic clusters within the GaAs material. The annealing temperature can have a major influence on the size and spacing of the resulting arsenic precipitates, with reported values ranging from ~10 nm diameter clusters at the low end of annealing temperatures (~600°C), up to ~19 nm at the high end of annealing temperatures (~1000°C), with all samples having the same growth temperature of 250°C [22]. However, increasing the initial growth temperature has been found to reduce the arsenic cluster diameter across all annealing temperatures. For example, when the LT-GaAs was grown at 320°C, the diameter of clusters ranged from ~7 nm (lowest annealing temperature), to ~15 nm (highest annealing temperature) [22]. These As cluster are defects in the GaAs that create electron traps in the material, which reduces the carrier lifetime of the material by trapping free electrons before they can recombine with holes. This effect, when compared to conventionally grown GaAs reduces the carrier lifetime by a factor of 1000 [12]. The anneal temperature and time play a key role in the final materials carrier dynamics, the trend being as anneal temperature and time increase, the carrier lifetime increases. However, as the annealing temperature increases, the mobility of the material also increases, this trade-off of carrier lifetime and mobility require careful tuning of the LT-GaAs growth process in order to create a material that has a sub picosecond carrier lifetime, but also a high mobility.

#### **1.4 Black Phosphorous-Based THz PCA**

In recent years, material scientists have begun to increase the amount of research focused on the use of 2D materials. Among these materials is black phosphorous (BP). BP generally exists as a bulk crystal, which can then be exfoliated into nano scale 2D flakes. In recent years, the use

of BP as an active layer material for optoelectronic devices, including THz PCAs has been investigated [23]–[26]. BP is an anisotropic semiconductor material that exhibits carrier dynamics in line with that of LT-GaAs. The reported hole mobility at room temperature in BP has been reported to be as high as  $5200 \text{ cm}^2/(\text{Vs})$ , with a sub picosecond carrier lifetime of  $\sim 0.36 \text{ ps}$  [17], [27], [28]. The crystal structure of BP consists of two unique axes, labeled armchair and zig-zag [29].

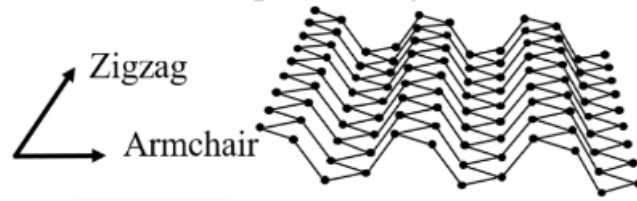


Figure 1.4-1: Crystal structure diagram of BP showing two distinct crystal directions [17].

These can be clearly seen above in fig 1.4-1, where the difference in crystal lattice structure across each axis is clearly seen. Due to the two distinct crystal directions in the BP lattice, the material has optical properties that are dependent on the polarization of the incoming light [30]. In terms of the optical absorption, at 780 nm, a common wavelength used for exciting THz PCAs, BP exhibits a 20% increase in absorption when exposed to light polarized along the armchair direction as opposed to the zig-zag [31]. Beyond its attractive optical properties, BP also has thickness dependent, and therefore tunable electrical properties, with a direct band gap energy ranging from 0.3 eV when in its bulk crystal form, up to 2 eV when in nanoscale flake form, allowing BP to act as a useful material well into the infrared range [32]. While these characteristics give BP the possibility of being a great active layer material for THz PCAs, there are major

discrepancies in the reporting of the carrier dynamics of BP. The values of  $5200 \text{ cm}^2/(\text{Vs})$  for the hole mobility, and  $\sim 0.36 \text{ ps}$  carrier lifetime represent the highest reported findings, while others have reported hole mobilities as low as  $850 \text{ cm}^2/(\text{Vs})$ , and carrier lifetimes as high as  $1800 \text{ ps}$  [33], [34]. These discrepancies in reported values are attributed to the difficulty in measurement of these properties, further, sample preparation and measurement setup play a key role in the validity and consistency of these measurements. Even with a wide range of reported values for optical characteristics of BP, it remains a potential candidate for use in THz PCAs. Overall, the structure of the BP PCA versus the LT-GaAs PCA is very similar, the difference being that a BP device does not need to be fabricated on LT-GaAs, but can use high resistivity silicon wafers to fabricate electrodes, the transfer a 2D flake of BP onto the antenna gap to act as the active layer material. An adaptation of a conventional THz PCA structure, now using a BP active layer can be seen below in fig 1.4-2.

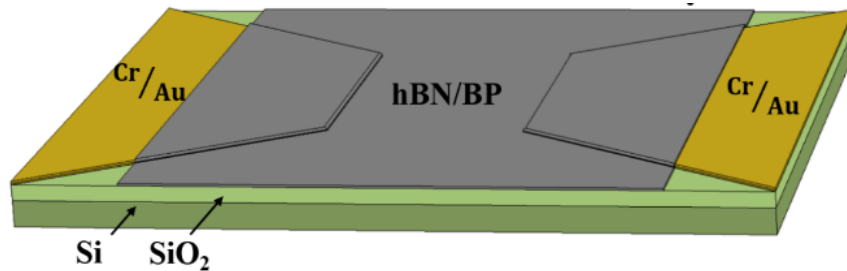


Figure 1.4-2: BP/hBN THz PCA structure [17].

## 1.5 PCA Electrode Geometry

Electrode geometry, specifically the gap of the PCA, plays an important role in determining many performance factors of the final device. From bandwidth to pulse amplitude, small changes in the design of the active area (gap) of the antenna can be used to tune a PCA to function in a



specific way. In effort to improve the efficiency and bandwidth of THz PCAs, many researchers have attempted using alternate electrode shapes, or other active area engineering techniques. Many of these efforts are focused on increasing the optical absorption of the active area material, as higher absorption results in a higher density of generated free carriers, and therefore higher THz pulse amplitude. While the conventional dipole antennas, shown below in fig 1.5-1 (a) has rectangular electrodes, alternate electrode shapes can have a multitude of effect on the resulting devices performance, from increasing overall signal amplitude due to higher optical-to-THz conversion efficiency, to widening the bandwidth of the resulting THz pulse. For example, using a spiral shaped antenna, researchers have reported being able to increase the overall signal amplitude of a THz pulse as compared to a conventional bowtie shaped dipole antenna by factor of 4 [35]. The use of interdigitated electrodes has been shown to increase bandwidth in THz PCA devices up to 8 THz, while allowing for a compact, high efficiency design [36]. In an effort to increase the optical-to-THz conversion efficiency, complex structures can be fabricated above the electrodes to increase absorption in the substrate. Plasmonic nano disk arrays fabricated on top of the electrodes have been reported to increase the power absorbed by the substrate from the optical pump, resulting in peak-to-peak THz pulse amplitudes 4 to 10 times greater than bare electrodes [37]. Other groups have reported using ZnO nanorods in the active area (gap) of the THz PCA to increase absorption using back reflections, resulting in a 4-fold THz power increase [38].

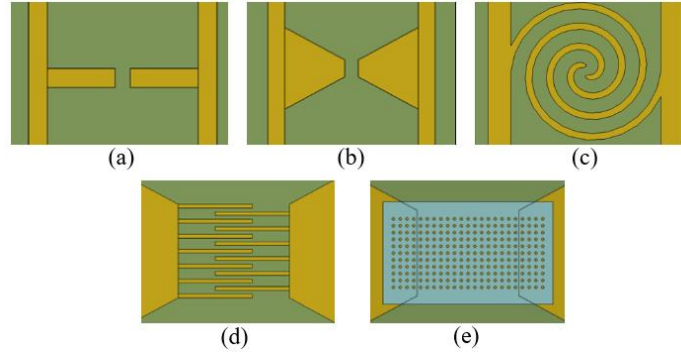


Figure 1.5-1: Electrode-based improvements of THz PCAs [17].

## 1.6 THz PCA Fabrication Methods

Fabrication of THz PCA devices employs many well-known techniques and can be accomplished in multiple ways. The main task is to be able to accurately pattern the designed electrodes for the PCA onto the selected substrate. There are two main technologies that can be employed to accomplish this. First, basic masked photolithography. By first coating a substrate in a photosensitive resist, it can then be selectively exposed to light, using a reflective mask to block light in certain areas and create the desired pattern in the resist.

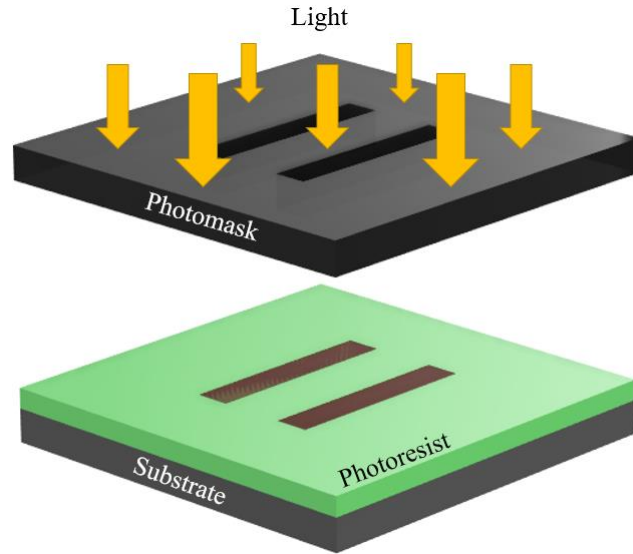


Figure 1.6-1: Diagram of typical photolithography process.

Phase shifting photolithography masks have existed for decades and improved the resolution of photolithography into the  $<1$  micron range [39]. Since then, advancements in photolithography have pushed the resolution into the nano scale, allowing for its use in devices much smaller than most THz PCAs [40]–[42]. This method of photolithography is a masked process, meaning it requires the fabrication of a unique photomask for each design. While this makes design changes take longer, it allows for many devices to be fabricated simultaneously by patterning an array of devices on a large piece of substrate, then dicing them into individual devices later.

An alternative fabrication method of THz PCAs uses electron beam lithography (EBL). This process uses a direct write method, where a focused beam of electrons is steered using a magnetic field in order to selectively expose areas of a resist coated substrate.

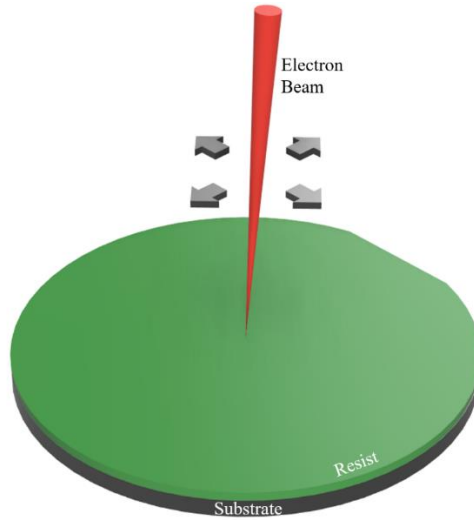


Figure 1.6-2: Simplified diagram of EBL process.

Because this method moves a single focused point to essentially draw the patterns, only one device can be fabricated at a time. While unable to simultaneously fabricate multiple devices, EBL uses no masks, meaning new design iterations can be fabricated without the need to create a new photomask. EBL also has a much higher resolution when compared to general masked photolithography, being able to write pattern features in the sub 10 nanometer range [43], [44]. More recently, EBL and resist technology has increased the feature resolution to less than 1 nanometer [45]. This ultra-high resolution allows for active area engineering of THz PCAs, adding the capability of patterning plasmonic structures over the PCAs to increase absorption of light into the semiconductor substrate.

## 1.7 Thesis Chapter Roadmap

This thesis consists of five chapters. First, this chapter, which provides background information and motivation regarding THz PCAs, their role and usage over various industries, and introduce two key technologies utilized for realizing physical devices. Chapter two will cover in

depth the specific fabrication processes used to create the devices studied in this work, detailing each step, and describing the tools and techniques used in this case. Chapter three will cover measurements of the THz PCAs, including a detailed description of the time-domain spectroscopy system used to characterize the devices. Next, in Chapter four, THz PCA arrays will be discussed, focusing on the feeding challenges and measurements of devices with more than one photoconductive element. Finally, chapter five will include discussion and conclusion of this thesis as a whole and go on to describe the possible future endeavors of this work.

## Chapter 2: LT-GaAs THz Photoconductive Antenna Fabrication

### 2.1 Computer Aided Design (CAD) and Proximity Effect Correction (PEC)

In order to fabricate a THz PCA device, it must first be thoroughly designed in some type of computer aided design (CAD) program. In the case of the devices studied in this work, AutoCAD by AutoDesk is used for all pattern design. In the case of the PCA design used in this work, past graduate students in this group have worked to comprehensively design, model, and simulate the antenna gap dimensions to verify their THz performance [17], [46]. The conclusion of this work determined that an antenna gap side of 5x4 microns was optimal for THz emission at 780 nm excitation wavelength. The dimensions of the gap in the bowtie PCA can be seen below in fig 2.1-1.

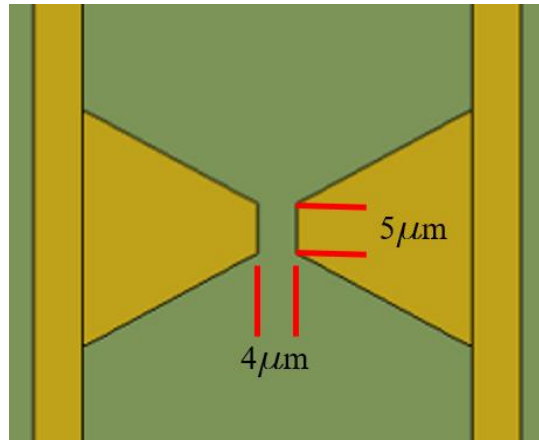


Figure 2.1-1: Bowtie emitter electrodes including dimensions of active area.

After modeling has confirmed the usability of a specific gap dimension, the design can be drawn in CAD to begin the process of creating the write files for use in fabrication. In the instance of these devices, EBL will be utilized for fabrication. The full CAD design consists of three main sections. First, the electrodes, which surround the active area of the antenna, and largely dictate

the function of the PCA. Next, the transmission lines, which serve to carry the DC bias voltage from the measurement setup to the electrodes, creating the bias field that will drive the free carriers created by the incident laser excitation. Finally, the bond pads, which provide sufficient area for electrically connecting the on-chip device to a chip carrier and PCB that will interface with the spectroscopy system. A full view of the THz bowtie PCA including all three regions can be seen below in fig 2.1-2.

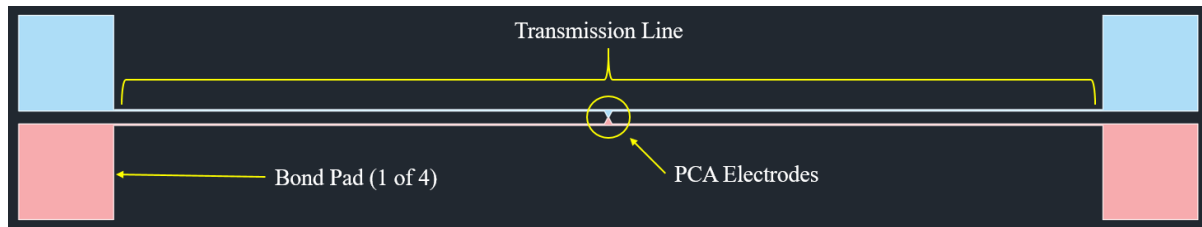


Figure 2.1-2: Full bowtie THz PCA emitter design, positive (blue), negative (red).

From here, the CAD design can be converted to an appropriate file format to be read by the EBL system, in this case, a GDSII file. At this point, the design could be fabricated as it is, however due to the small feature size, some “bleeding” of the electron beam, due to the proximity effect, can cause small features to be washed out in the final design [47], [48]. This effect is due to the electron beam passing through the photoresist, then scattering off the semiconductor substrate surface, and exposing areas of the resist that should have remained unexposed. A diagram of this scattering effect can be seen below in fig 2.1-3, where the yellow dotted arrows show the scattering of electrons off the substrate, into areas surrounding the intended exposure area. The size of the surrounding area that is exposed is greatly influenced by the dosage of the electron beam, or charge units per area. Because of this, the proximity effect can be minimized by fracturing

the designed pattern into small sections and modulating the dosage in each area depending on the required feature size and resolution.

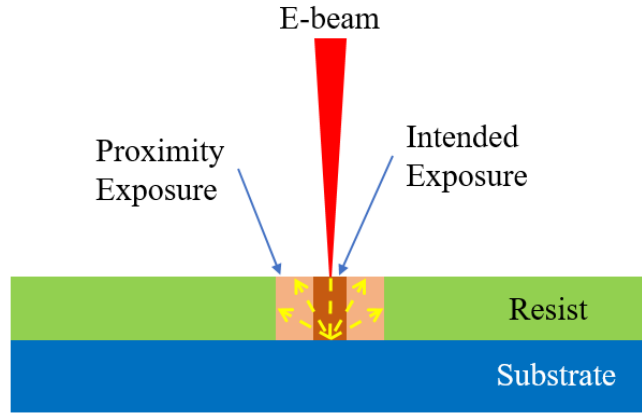


Figure 2.1-3: Diagram of overexposure due to proximity effect.

Beyond the effect of electron backscattering from the substrate, there is also forward scattering, where the electrons disperse from the top of the resist down, creating a larger exposed area closer to the resist-substrate boundary than at the surface of the resist [49]–[51]. The proximity effect correction fracturing in this work is done using Beamfox software. Below in fig 2.1-4 (a), the original CAD model of a circular THz PCA can be seen. After exposure via EBL, the resulting pattern is shown in fig 2.1-4 (b), where the dotted circle highlights the overexposure due to forward and backward scattering of electrons. After proximity effect correction, the pattern is fractured and the dosage at each point is modulated according to the software’s algorithm, the now fractured pattern is shown in fig 2.1-4 (c), with the resulting exposure in fig 2.1-4 (d). The difference in pattern resolution between fig 2.1-4 (b) and (d) can clearly be seen. Before PEC, the small sharp corners of the circular electrode where it meets the transmission line is completely overexposed, and after using PEC, is nearly identical to the intended design. Other small features in the four



designs studied in this work also suffer from the proximity effect, specifically the corners of the small triangles in the fractal design shown below in fig 2.1-4 (b), and the 1-micron by 10-micron slots in the electrodes shown in (c).

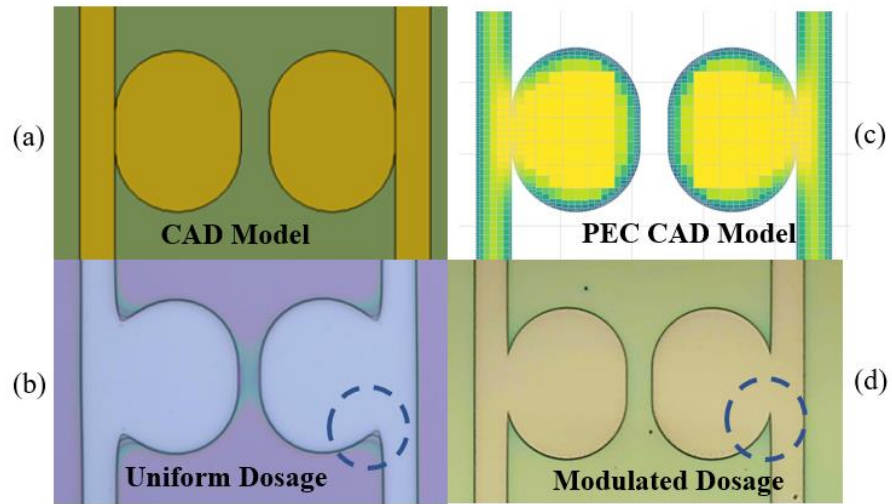


Figure 2.1-4: Comparison of PEC and non-PEC devices.

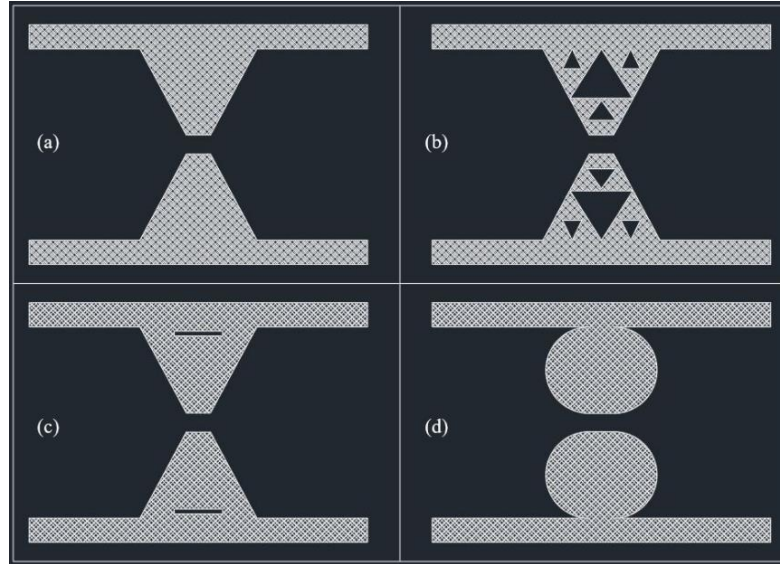


Figure 2.1-5: CAD of electrode shapes. (a) bowtie, (b) fractal, (c) slotted, (d) circular.

## 2.2 LT-GaAs Wafer Growth and Sample Preparation

In order for the THz PCAs described in this work to function, the semiconductor substrate that they are fabricated on, in this case LT-GaAs must meet specific criteria. Notably, the mobility must be sufficiently high, and the carrier lifetime must be below or near one picosecond. LT-GaAs meets these requirements, but the specific values of mobility and carrier lifetime can vary based on the growth parameters used to grow each individual wafer. As previously explained in section 1.3, the growth temperature, and anneal temperature play a critical role in the forming of arsenic defects in the crystal lattice of LT-GaAs, these defects allow for ultrafast recombination of free carriers by acting as recombination centers. To study the effect that growth and anneal temperature have on the final performance of the THz devices, two wafers, each with unique growth specifications, were used throughout the fabrication process. Both wafers were grown at the

University of California Los Angeles (UCLA) by Dr. Baolai Liang. The growth parameters used in wafer one and wafer two, as well as the layer thicknesses can be seen below.

Table 1: LT-GaAs Growth Parameters

	<b>Wafer 1</b>	<b>Wafer 2</b>
<b>Substrate material/thickness</b>	SI-GaAs / 500 $\mu\text{m}$	SI-GaAs / 350 $\mu\text{m}$
<b>Buffer layer (GaAs) thickness/growth temperature</b>	50 nm / 580°C	50 nm / 580°C
<b>LT-GaAs layer thickness/growth temperature</b>	500 nm / 258°C	250 nm / 250°C
<b>Anneal temperature/time</b>	590°C / 10 min.	525°C / 10 min.

As seen in the table, both wafers are grown on the same starting substrate, which is semi-insulating gallium arsenide, with varying thicknesses. The first wafer having a thickness of 500-microns, a common wafer thickness to deal with when growing semiconductor materials. The second wafer was grown on a 350-micron thick wafer, which was fabricated in order to match the thickness of commercial THz PCAs used in the time domain spectroscopy system employed to characterize the PCAs later. This was done to make a more uniform comparison between the devices fabricated in this work, and the industrially fabricated devices used for calibration of the system. Next, a buffer layer of gallium arsenide is grown on top of the carrier wafer in order to smooth the surface, and prepare it for the low temperature growth process. The buffer layers in both wafers are identical in thickness and growth temperature. The low temperature layer is then grown, in the case of the first wafer a thicker 500 nm layer is grown at 258°C, while in the second

wafer, a low temperature layer of 250 nm is grown at slightly lower temperature of 250°C. Once the growth is completed, both wafers are annealed for ten minutes, with a temperature of 590°C in the first wafer, and 525°C in the second wafer. As discussed in section 1.3, when the material is annealed at a higher temperature, the mobility and carrier lifetime tend to increase as well, meaning that wafer 1 should have a slightly higher mobility than wafer 2, however, wafer 2 should have a lower carrier lifetime, and therefore faster device response. The results of optical pump THz probe measurements resulting in values for carrier lifetime, carrier concentration, and mobility can be seen in Appendix A. Both wafers appear identical and are two inches in diameter. Fig 2.2-1 below shows an example of one LT-GaAs wafer before being diced into device-sized samples. After wafer growth is completed, the first step in wafer preparation for device fabrication is dicing. Dicing is the process in which the wafer is separated into individual pieces, each of which a THz PCA can be fabricated on.

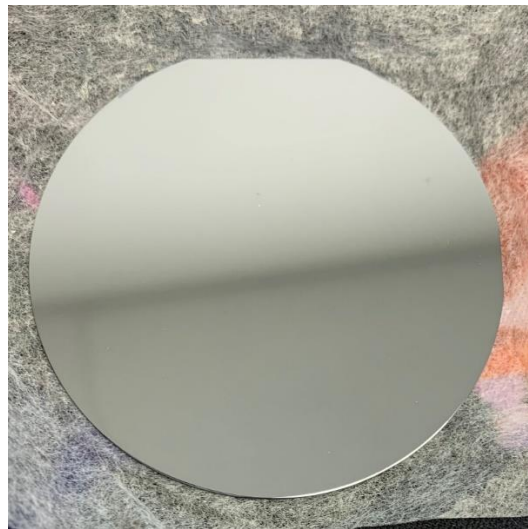


Figure 2.2-1: As grown 2" LT-GaAs wafer used in fabrication of THz PCAs.

This is a trivial procedure and can be done with a scribe by making a small scratch on the edge of the wafer, and breaking the wafer over the edge of a glass microscope slide, which unzips the crystal lattice, creating a straight break in the wafer. Through dicing, the wafer can be sectioned into many pieces, as shown below in fig 2.2-2.



Figure 2.2-2: Diced section of LT-GaAs wafer, ready to be used in fabrication.

Once device sized samples are procured, they must be spin coated in a electron sensitive resist to be used in the EBL process. In the case of all fabrication in this work, polymethyl methacrylate (PMMA) is utilized. This is a positive resist, meaning that the areas exposed to the electron beam will be softened and removed as opposed to negative resist, where the exposed areas are hardened, and the unexposed areas can be removed. The process of spin coating is as follows. First, the sample must be cleaned. This is done by first soaking the sample in acetone and submerging it in an ultrasonic bath to agitate it, removing any surface debris or oils. Next, the sample is similarly soaked and sonicated in isopropyl alcohol (IPA), then blown dry with nitrogen

gas. Once the sample is dried, it is placed on a hot plate at 180°C in order to ensure any moisture is evaporated as seen below in fig 2.2-3.



Figure 2.2-3: LT-GaAs sample on hot plate.

The sample is then transferred to the chuck of a spin coating machine, where it is held down by the force of a vacuum. With the sample secured to the spin coating machine, the PMMA resist is applied to the surface of the sample using a dropper, as the final layer will have a thickness of a few hundred nanometers, a very small amount can be used. The sample is then spun at a predetermined speed to achieve the desired thickness. An example of a LT-GaAs sample mounted on the vacuum chuck of a spin coater can be seen below in fig 2.2-4.



Figure 2.2-4: LT-GaAs sample on vacuum chuck of spin coater.

The speed at which the sample is spun can be varied to achieve different thickness. The final thickness of the resist not only depends on the speed it is spun at, but also the viscosity of the resist used. PMMA is diluted using anisole, the ratio so which is denoted as A2, or A4 in the case of this work. Each dilution has a unique spin curve that must be followed to ensure that the thickness of the resist is correct in the final device. Below in fig 2.2-5 are the spin curves for PMMA A2 and A4 showing the thickness achievable at different spin speeds.

An important factor to consider is the final thickness of the metallic electrode layer for the THz PCA. In general, the thickness of the metal applied to the device after EBL patterning can be half of the thickness of the PMMA layer in order to have success lift-off of the PMMA, leaving behind the desired pattern.

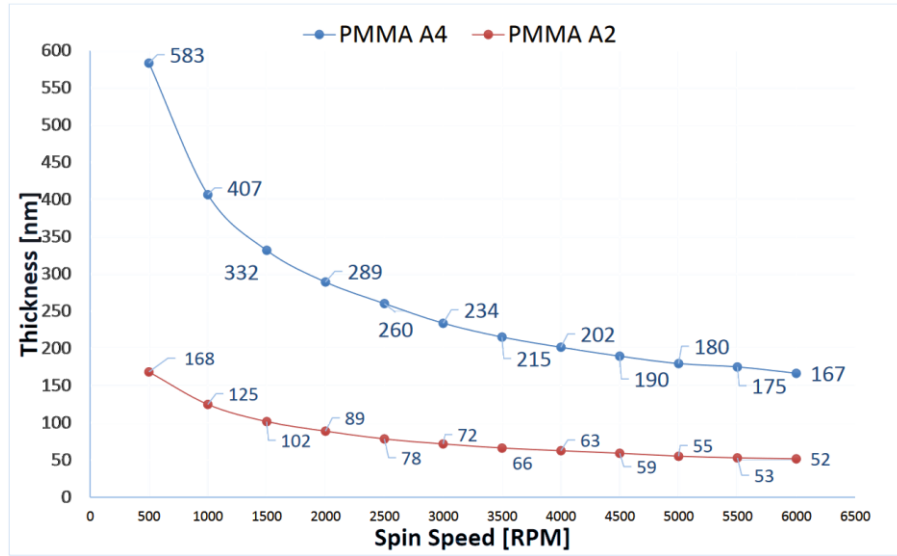


Figure 2.2-5: PMMA A2 and A4 thickness based on spinning speed [52].

In the case of this work, two thickness of PMMA are used, first, where small details are not an issue, as in the standard bowtie electrodes, PMMA A4 spun at 4000 RPM, resulting in a 200 nm thick layer is applied, allowing for a total metal thickness of up to 100 nm to be evaporated in a later steps, however, this thick of a resist layer results in more electron scattering during the EBL exposure process, resulting in more overexposure, and a loss in small feature resolution. In the case of small feature size, such as in the slotted, fractal, and circular THz PCAs, PMMA A2 is spun at 1500 RPM resulting in layer thickness of 100 nm, limiting the total metal thickness to 50 nm, but allowing for small features to be realized. A PMMA coated sample can be seen below in fig 2.2-6 where the different colors represent small differences in resist thickness.

Once spin coated in resist, the sample is again placed on a hot plate at 180°C, which vaporized the anisole dilutant, leaving behind a hardened PMMA layer. Once completed, the sample is fully prepared and ready for exposure in EBL.



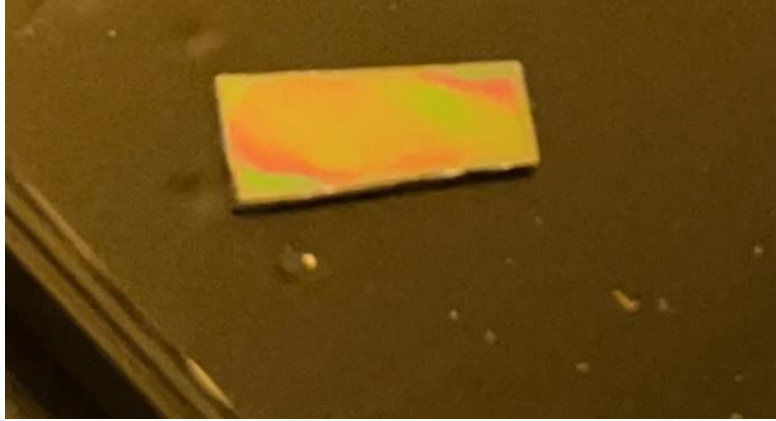


Figure 2.2-6: PMMA coated LT-GaAs sample.

### 2.3 EBL Exposure and Pattern Development

Exposing the diced and spin coated LT-GaAs samples in EBL is the process that creates the stencil that will alter have metal evaporated onto it in order to form the electrodes of the THz PCA. The basic concept of EBL as well as masked photolithography has been previously explained in section 1.6. In the case of the THz PCAs studied in this work, all fabrication has been done using EBL. The reason for utilizing EBL as the sole fabrication method for these devices has several reasons. First, the availability of lithography tools at the time of fabrication was only EBL. Second, while photolithography would drastically reduce the time taken to produce each device, any changes in the design would require a new photomask to be fabricated, which can be time consuming and costly. With the direct write technology of EBL, single devices can be patterned on small samples without the need of a mask aligner, or photomask, which has made design changes through the fabrication process trivial.

Before the sample can be loaded into the EBL machine, it must be secured in the EBL cassette. This is a metal apparatus that holds the sample in the EBL machine while the writing

process is happening. To mount the LT-GaAs sample in the EBL cassette, it must first be removed from the EBL machine. Because EBL is a high vacuum process, various chamber exchanges must happen in order to maintain the inner vacuum of the system. The specific EBL system utilized for this fabrication is a JEOL JBX-5500 50kV EBL system. There is a status screen mounted directly to the EBL machine that indicates various pressures and stage statuses of the cassette within the EBL machine. Fig 2.3-1 (a) below shows the location of the main information screen of the EBL machine, while fig 2.3-1 (b) shows the information displayed on the screen. As labeled in the figure, the transfer rods on the system are used to move the cassette between the two main chambers of the system. VG1 is the inner write chamber, where the cassette and sample are located during a write, while VG2 is the transfer antechamber that is used to remove the cassette from the EBL machine without losing the high vacuum within the VG1 chamber. The information screen shows the status of cassette, the green light left of “home position” indicating that the cassette is within the VG1 chamber, and the green light to the left of “holder on/off” indicating that the transfer rods are locked onto the cassette, ensuring that it cannot move forward or back on its own.

To remove the cassette from the system, the transfer rods must be slowly inserted from VG2 to VG1, this must happen slowly to ensure the vacuum is not lost, which will require a full reset of the EBL system before a write can proceed. Before the transfer rods can be inserted into VG1, the brown button labeled open on the information screen seen in fig 2.3-1 (b) must be pressed, which opens a valve between VG2 and VG1 to facilitate the cassette transfer. Once the transfer rods are fully inserted into the VG1 chamber, the cassette can be slowly removed from VG1, and into VG2. After the cassette is slowly transferred to VG2, the blue close button should be pressed, which isolated the two chambers once again. VG2 can then be vented by pressing the blue vent button on the info screen seen in fig 2.3-1 (b).

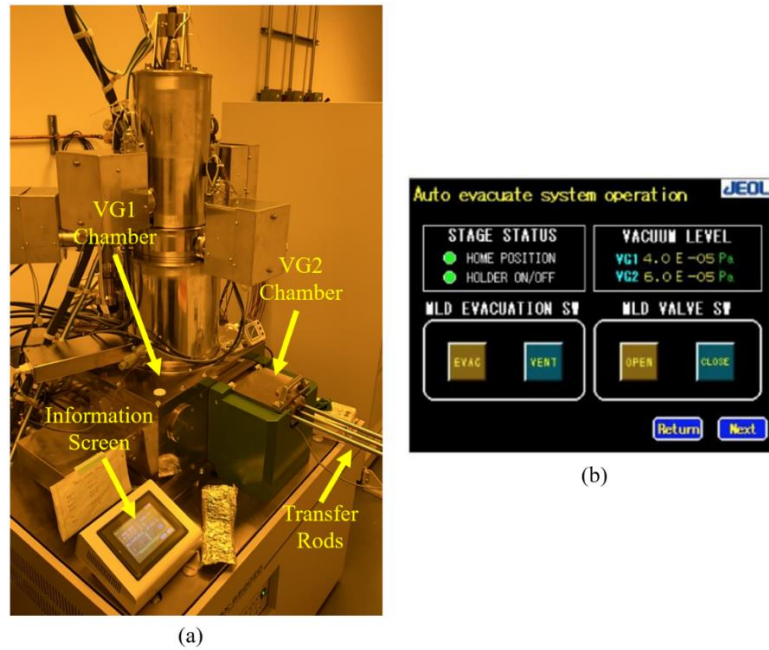


Figure 2.3-1: (a) Main JEOL EBL system. (b) Information status screen.

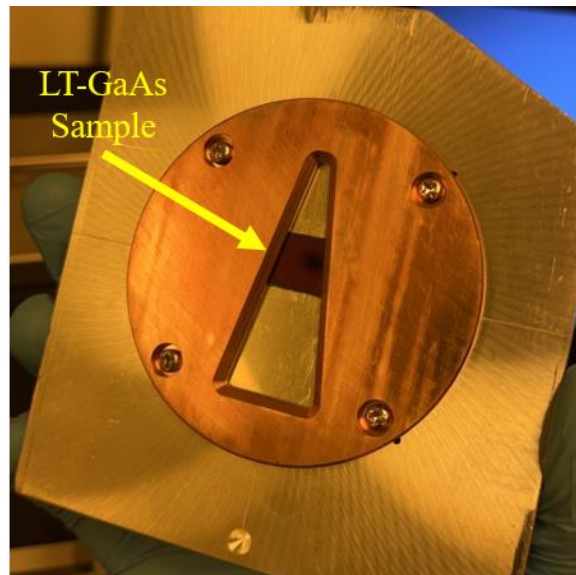


Figure 2.3-2: EBL cassette with LT-GaAs sample held in place for writing.

This process isolates the VG2 chamber from VG1 then brings VG2 to atmospheric pressure, where it can be opened, and the cassette removed. The EBL cassette with a LT-GaAs chip sample can be seen below in fig 2.3-2.

Once the cassette is removed and the LT-GaAs sample is mounted into the workable area, which is the triangular area surrounded by copper, the whole cassette can be put onto a profile projector, to locate the center of the chip with respect to a known calibration spot on the cassette.

The process of finding the center of the chip consists of two parts. First, the top edge of the sample is located on the monitor as seen in fig 2.3-3 (a). From here, the digital coordinate read out can be set to zero to act as a reference, the profile projector is then moved directly down until the bottom edge is located as seen above in fig 2.3-3 (b). Next, the distance traveled, as seen on the coordinate read out can be divided by two, and moved to that value, which represents the midpoint between the top and bottom edge of the sample.

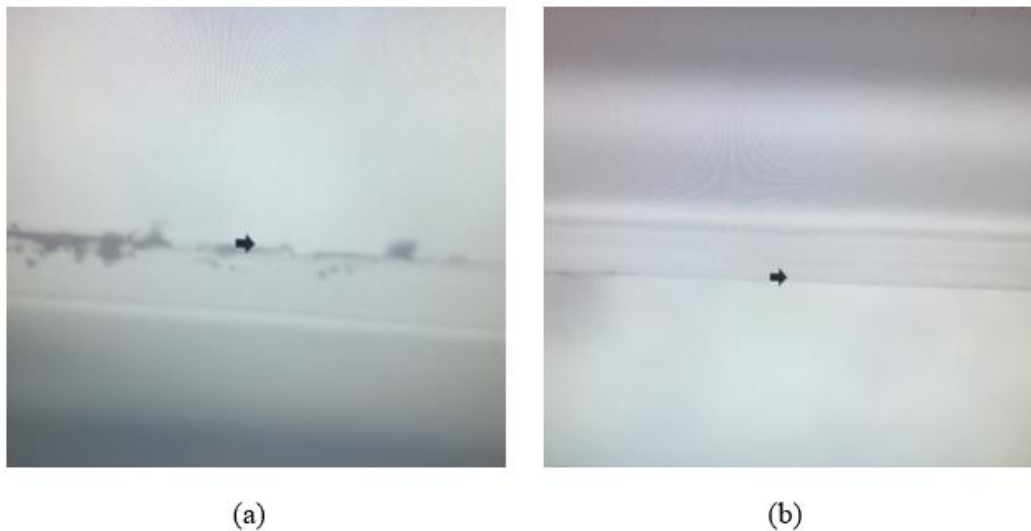


Figure 2.3-3: (a) top edge of the LT-GaAs. (b) bottom edge of the same sample.

This same process is repeated, now in the horizontal direction, referencing the edges of the writable area of the cassette, as the chip edges cannot be seen. When the profile projector has been positioned in the center of the sample, the coordinates are reset to (0, 0). Finally, the known reference location is found on the cassette, and the coordinates displayed on the digital read out are recorded. A similar process will later be done under the scanning electron microscope within the EBL system, using the same reference location, so that the system can locate the center of the sample to write the pattern. The reference location of the cassette is shown below in fig 2.3-4 (a), with an example of the coordinate readout shown in fig 2.3-4 (b).



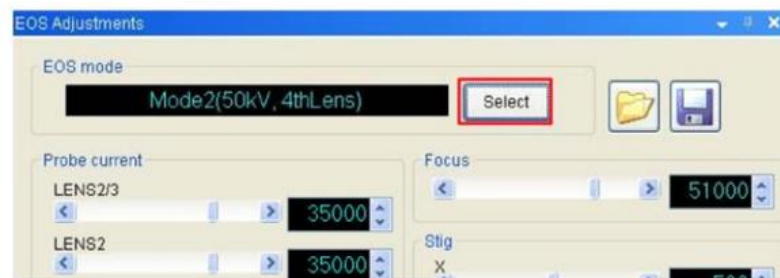
Figure 2.3-4: (a) reference point located on EBL cassette. (b) example coordinates with respect to center of LT-GaAs sample.

Once the relative center of the sample is identified and recorded, the EBL cassette can be reloaded into the EBL system for the exposure procedure. To reload the cassette, the VG2 chamber

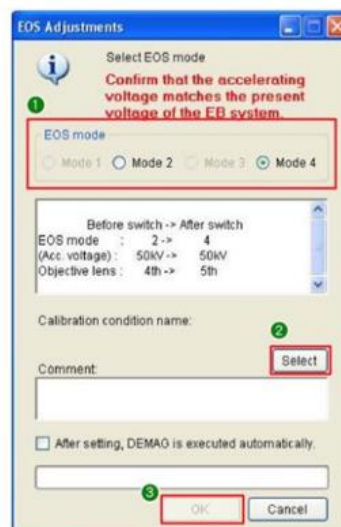
must first be taken to atmospheric pressure by pressing the “vent” button on the information screen. Once the venting process is complete, the chamber is placed back into the VG2 chamber, the lid is closed, and the chamber is evacuated by pressing the “evac” button on the information screen. Once pressed, the system will begin lowering the pressure in the VG2 chamber. The information screen should be monitored while the pressure drops, and the cassette should remain in the VG2 chamber until the pressure falls below  $1.5\text{E-}4$  Pa. Once this pressure is reached, the valve between the VG2 and VG1 chamber can be opened by pressing the “open” button, which will quickly lower the pressure even further due to the difference in pressure between VG2 and VG1. The cassette should then slowly be inserted using the transfer rods into the VG1 chamber. It is important to watch the pressure in the VG2 chamber during this transfer process, as moving too quickly will increase the pressure in the chambers, resulting in a vacuum error if it reaches above  $9.0\text{E-}4$  Pa. Once the cassette is fully inserted, the transfer rods can be backed out completely, and the valve can be closed by pressing the “close” button on the information screen.

Once the cassette is fully loaded into the EBL system, all operations will take place within the EBL software. First, the EOS mode must be selected, which defines which lenses, and acceleration voltage the EBL system will operate with, depending on the smallest feature size and resist type used in fabrication, other EOS modes can be selected, but all devices studied in this work utilize mode 4, which uses the 4<sup>th</sup> lens in the EBL system, with an acceleration voltage of 50kV. Below in fig 2.3-5 (a), the EOS mode selection button, and EOS adjustment window can be seen in (a) and (b) respectively. Once the EOS mode is selected, the “Selection” button within the EOS adjustment window should be pressed, and the calibration file for the current write can be selected. These calibration files are created by JEOL personnel and include the many settings for proper operation of the EBL system; however, the specifics of these settings are unknown to

general users of the EBL system. Before pressing the “OK” button to finalize and commit these settings, a physical adjustment knob seen in fig 2.3-6 on the EBL system must be checked to ensure the proper aperture of the system is being used. There are 4 apertures, which correspond to different writable areas that the EBL system can use without having to physically move the chip within the chamber. For this work aperture 2 is utilized, so ensuring the knob has aperture 2 selected should be done before committing the calibration settings.



(a)



(b)

Figure 2.3-5: (a) main EBL software window. (b) EOS adjustment window.



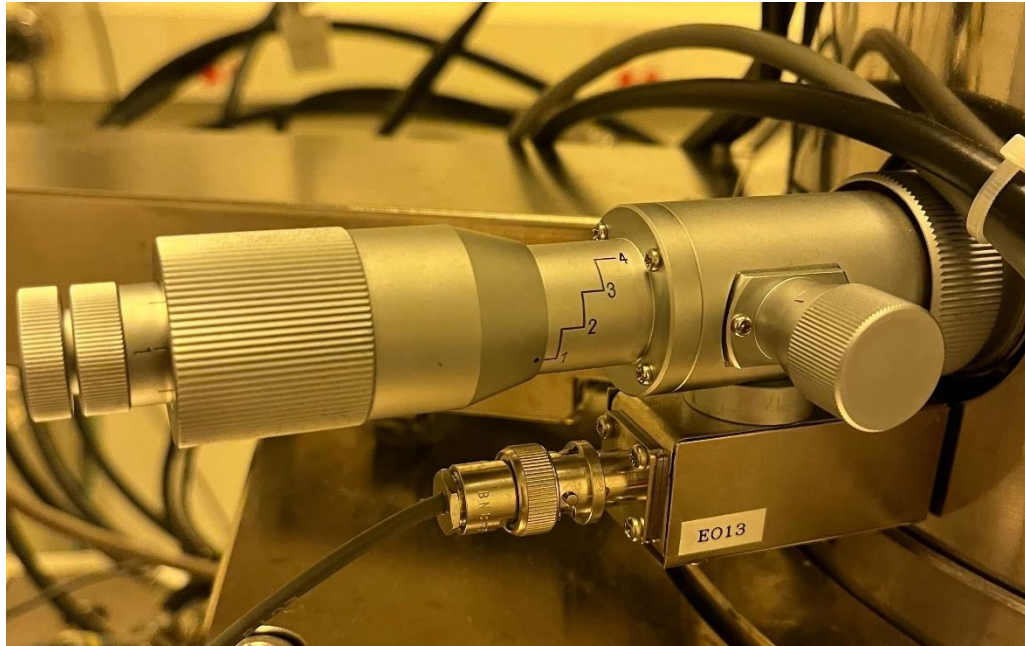


Figure 2.3-6: Aperture adjustment knob with aperture 1 selected.

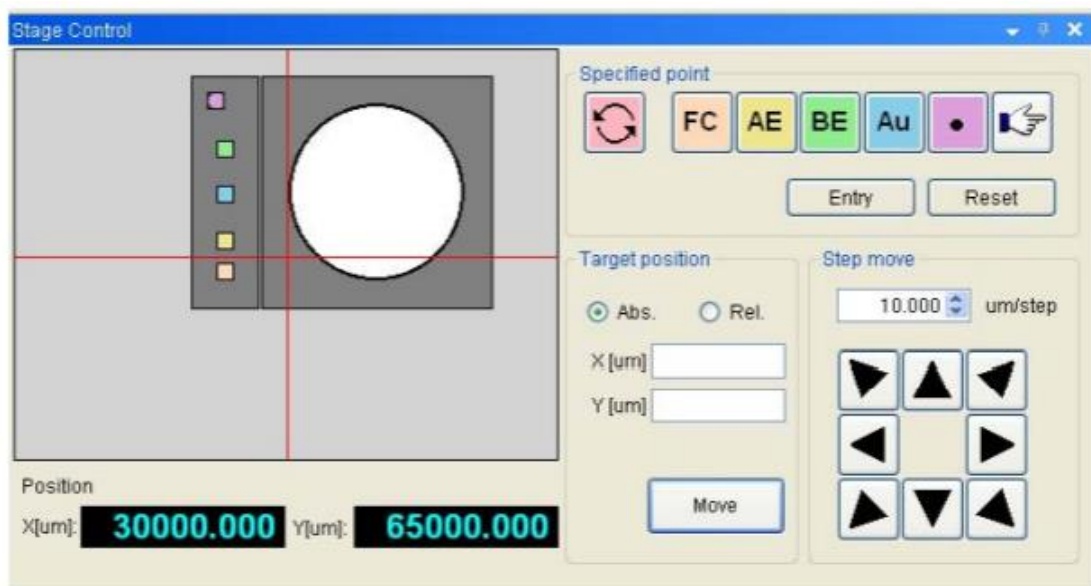


Figure 2.3-7: Main stage control screen in EBL user software.



Once the proper aperture has been selected, and the calibration file is committed, manual calibration can take place. First, the current in the faraday cup must be checked to ensure it matches the current expected from the calibration file being used, in the case of this work 1 nA. To check the current, the “FC” button shown above in fig 2.3-7 on the main GUI of the EBL software should be selected, then the “Move” button can be pressed. This will move the cassette within the system to the proper position to measure the FC current. Once moved, the beam can be turned on, and the current can be read from the bottom right corner of the software, not pictured in the figure. If the read current does not match the expected value, it can be adjusted using the slider labeled “LENS 2/3” under the probe current window shown below in fig 2.3-8.



Figure 2.3-8: Probe current adjustment window showing LENS 2/3 slider.

Once the FC current is correct, the cassette can be moved to the AE position, and the scanning electron image (SE image) can be selected from the display drop down menu. The center of the SE image should be aligned with the corner of the cassette mark in the microscope window, then the “entry” button, followed by the “AE” button should be selected, confirming the position of the AE mark. This same process is then repeated with the BE mark. After these three manual calibrations have been performed, auto calibration can be started. To begin this process, the button

labeled “Calibration” in the main GUI of the EBL software can be pressed, which will open the calibration window shown below in fig 2.3-9.

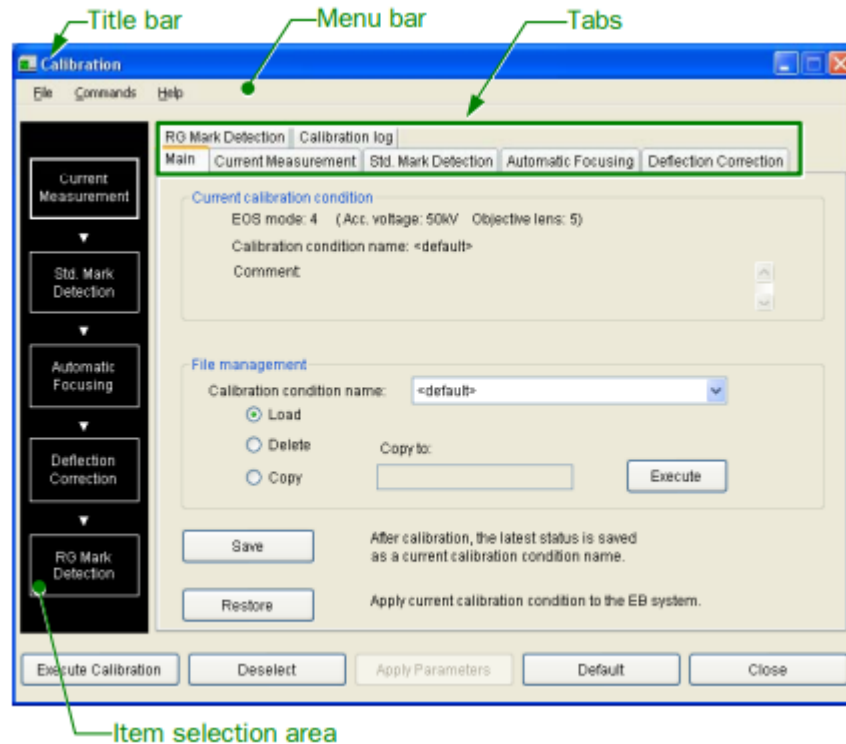


Figure 2.3-9: Calibration menu within EBL software.

First, the calibration file that was previously selected in the EOS adjustment window should be selected again under the drop-down menu labeled “calibration condition name.” Once selected, the button next to “load” should be selected, and the restore button should be pressed. Next, the first four calibration procedures on the left side of the menu should be selected, they are: “Current measurement”, “Std mark detection”, “Automatic focusing”, and “Deflection correction.” Once selected, the execute button at the bottom of the menu can be pressed, and auto calibration will occur.

Once auto calibration has been completed, the mark found early on the cassette under the profile projector must be found using the SE image in order to orient chip in the EBL system. This is done by selecting the SE image from the display drop down menu, then entering the known general coordinated of the mark into the X and Y coordinate boxes and selecting move. Once the cassette is moved, it should be fine-tuned using the arrows in the software until the mark is centered in the crosshairs of the viewing window as shown below in fig 2.3-10. This is the same cassette mark highlighted by the dashed red circle in fig 2.3-4 (a), now seen under the scanning electron (SE) microscope within the EBL system as opposed to the profile projector used for finding the chip center. Once found, the coordinates of this mark should be recorded, and using a premade excel document utilized by all general EBL users, a coordinate transformation is done to the previously found coordinates on the profile projector, giving new coordinated that allow the EBL system to know exactly where the chip sample within the cassette is at.



Figure 2.3-10: SE image of cassette reference mark used for locating LT-GaAs sample.

From here, the sample is ready to have the pattern exposed. To do so, the exposure menu must be opened by pressing the exposure button in the main EBL software window. This will open the exposure menu shown below in fig 2.3-11.

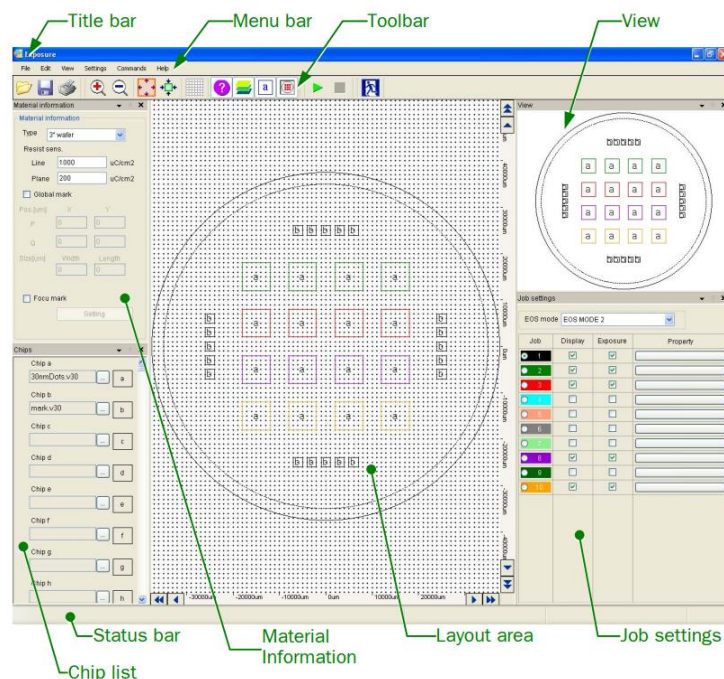


Figure 2.3-11: Exposure GUI with various sectioned used during exposure setup labeled.

First, the proper cassette or sample shape should be selected in the material information section from the drop-down menu labeled type, the example exposure above shows a 2" wafer, but this can differ depending on the fabrication being done. In the case of this work the cassette labeled "BZ-Z1..." is used. Next, the line and plane values should be set. These define the dosage parameters that will be used for the write. In the case of the LT-GaAs PCAs fabricated here, a modulated dosage will be used due the proximity effect correction done during the pattern preparation step, meaning the value entered in the "plane" section will serve as a base dosage, and

will be multiplied depending on what pattern layer is being written. In the case of a non-modulated dosage,  $850 \mu\text{C}/\text{cm}^2$  for PMMA A4, and  $400 \mu\text{C}/\text{cm}^2$  for PMMA A2 should be used. This dosage should be experimentally found and will change with different resists and thicknesses. Once set, the chip pattern can be uploaded by pressing the “...” button next to chip a in the chip list section. From here, the pattern to be written should be browsed for and selected. Once uploaded, it can be dragged from the chip list, onto the cassette, and its coordinates can be entered by right clicking the chip and selecting properties. When the coordinates are entered, the chip should snap to the location of the LT-GaAs sample within the cassette. Finally, the green play button in the top toolbar can be pressed, initiating the EBL exposure. Once complete, the unloading procedure detailed earlier should be followed to remove the cassette, remove the LT-GaAs sample, and then reload the now empty cassette into the EBL system.

The patterned chip must now be developed in order to remove the exposed areas. This process has two steps. First, the chip should be submerged in an MIBK:IPA solution for exactly 60 seconds to dissolve the exposed areas of resist, after which the chip should be rinsed in IPA, then blown dry with nitrogen gas.

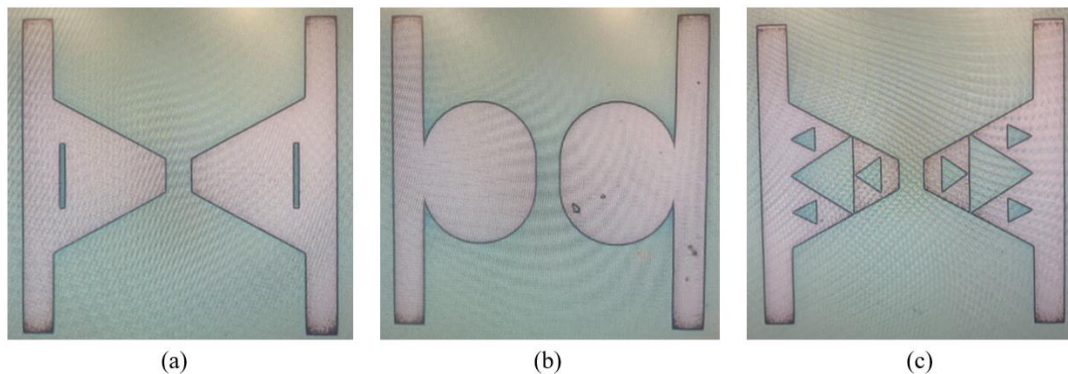


Figure 2.3-12: Fully developed EBL patterns. (a) slotted, (b) circular, (c) fractal.

This completes the EBL exposure and development process, after which the pattern can be inspected for accuracy under an optical microscope. Examples of developed patterns of three different electrode shapes of THz PCAs can be seen above in fig 2.3-12.

## 2.4 Etching Electrode Features

As an alternative method do using proximity effect correction (PEC). The small features can be patterned into an etch layer on top of blank electrodes and the slots or fractals can be etched into the metal. The process for creating the etch mask is very similar to the spin coating and patterning process described in sections 2.2 and 2.3 above. First, a patterned and metalized THz PCA must be completed, in this case, the device will have bowtie electrodes with no features present. The exact same spin coating process used to prepare the blank LT-GaAs samples is followed to create a layer of PMMA resist on top of the THz PCA. Once this layer has been created, the design features, either fractals or slots in the case of this work, are patterned into the PMMA etch layer and developed. An example of a patterned and developed etch layer on top of metalized electrodes can be seen below in fig 2.4-1.

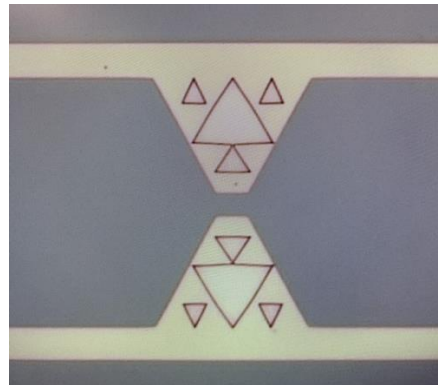


Figure 2.4-1: Fully metalized bowtie electrodes with fractal etch mask patterned in PMMA.

Once patterned, the device can be etched by submerging it in gold etchant, followed by chromium etchant to remove both layers of metal, forming the desired features in the electrodes. It is important to note that the time spent in the etchant is extremely critical and must be found experimentally to avoid over etching of the features. Below in fig 2.4-2 (b) is an example of an attempted slot etching using the manufacture recommended etch time of 30 seconds, which resulted in extremely over etched features, showcasing the importance of finding proper etch time for each feature through experimentation.



Figure 2.4-2: (a) slotted etch mask before etching. (b) over etched slots after 30 seconds.

Through trial and error, a proper etch time can be found that results in a well-defined and dimensionally accurate slot as shown below in fig 2.4-3 (b). Here the etch time experiments are shown, and the resulting slotted antenna using the proper etch time can be seen as well. All dimensions shown in fig 2.4-3 (a) are in microns. As shown, with an etch time of 2.5 seconds very accurate slots can be formed using etching. However, there are several drawbacks to this approach, leading to PEC being preferred in all cases.



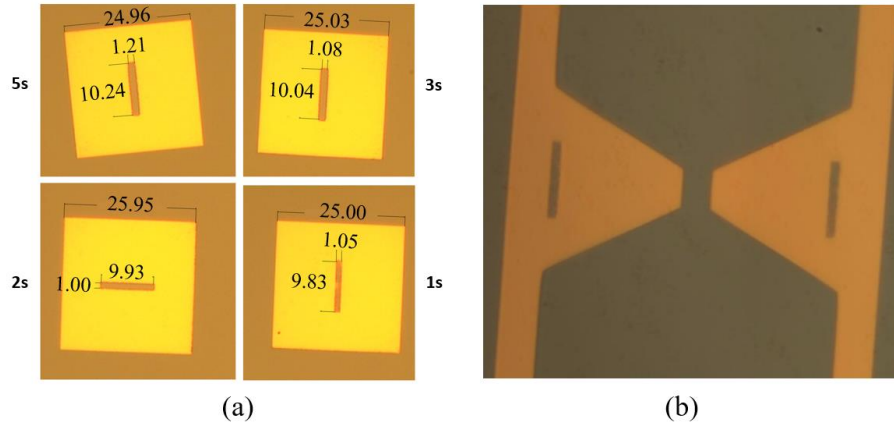


Figure 2.4-3: (a) slot results with different etch times. (b) slots etched for 2.5 seconds.

First, etching requires many additional steps, doubling the complexity and time it takes to produce a device. Next, PMMA, which is the only resist used to fabricate all devices shown in this work, has relatively poor etch resistance, which can result in inconsistency protection of the gold surfaces that should not be etched, due to this, even using the same etch time on each sample can result in random errors to the slot.

Finally, some pattern areas experience a loss of dimensional accuracy in places that are not practical to etch out, an example being the sharp corners between the transmission line and electrodes of the circular PCA. In cases like this, it is much more practical to improve the overall accuracy during the initial pattern exposure by using PEC, as opposed to attempting to go back and etch out small areas while maintaining the overall shape of the circular electrode.

## 2.5 Thermal Evaporation and Packaging

In order for the THz PCAs to conduct the DC bias voltage applied to them, they must be metalized. As shown in fig 1.2-2 in the previous chapter, the electrodes and transmission lines of the PCAs consist of two layers of metal. First, a 5nm layer of chromium is deposited to act as an



adhesion layer, this is necessary due to the weak adhesion force of gold to the surface of the LT-GaAs. The chromium adheres strongly to the surface of the PCA and creates a surface that will allow the much thicker 50nm layer of Au to adhere to. In order to evaporate the metals onto the PCA, it must first be secured to a chuck that will mount inside the evaporator. The chip is held in place by two metal fingers that press on the surface of the chip. When mounting the sample, care must be taken to ensure the metal fingers to not cover or touch any part of the patters. Below in fig 2.5-1, a LT-GaAs sample can be seen mounted to the golden chuck of the thermal evaporator.



Figure 2.5-1: Thermal evaporator chuck with top metal finger holding LT-GaAs chip.

Once the chip is secured in the chuck, the entire assembly can be mounted with the sample facing down into the evaporator, which houses multiple material bays where different metals are stored for evaporation. A control wheel can be turned to change the material being evaporated in order to deposit multiple layers of metal during a single vacuum cycle. Below in fig 2.5-2, the

thermal evaporator used in this work can be seen, with labels showing the chuck mounting location, the material bays, and the manual shutter, used to block the evaporation until a consistent rate of evaporation is observed.

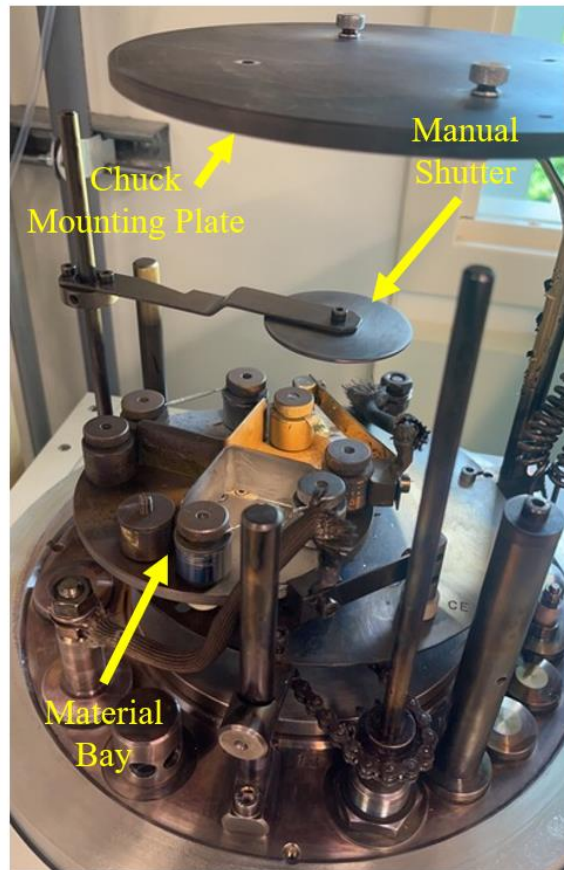


Figure 2.5-2: Inside of thermal evaporator showing 4 material bays.

Once the chip is mounted and a vacuum is pulled on the evaporator, current is passed through the metal of choice until it begins to evaporate upward toward the sample. A crystal detector is used to monitor the rate at which the metal evaporates. Ideally the manual shutter should remain closed until a rate of  $\sim 1\text{nm/s}$  of metal is observed to be evaporated, at which point the manual shutter is opened, and the desired amount of metal is deposited onto the sample. In the case

of this work, chromium is deposited to a thickness of 5nm, then the material bay is rotated to gold, and 50nm are deposited. Once the metal has been deposited, the chamber can be vented, and the chuck can be removed. Below in fig 2.5-3, two metalized samples can be seen still on the chuck of the evaporator, now coated in gold.



Figure 2.5-3: Thermal evaporator chuck holding two metalized LT-GaAs samples.

Finally, all of the deposited metal not desired for the pattern of the PCA must be removed. This is achieved by soaking the entire chip in acetone to remove the PMMA layer, essentially peeling off a stencil, leaving behind the metalized THz PCA. The chip must soak for a minimum of 12 hours in order to obtain consistent lift off results. In cases where some metal is left behind, particularly between the transmission lines of the PCAs, short amounts of sonication (typically 5-10 seconds) can be used to aid in the removal of the excess PMMA and gold. An example of unwanted metal remaining on the chip after lift-off can be seen below in fig 2.5-4.

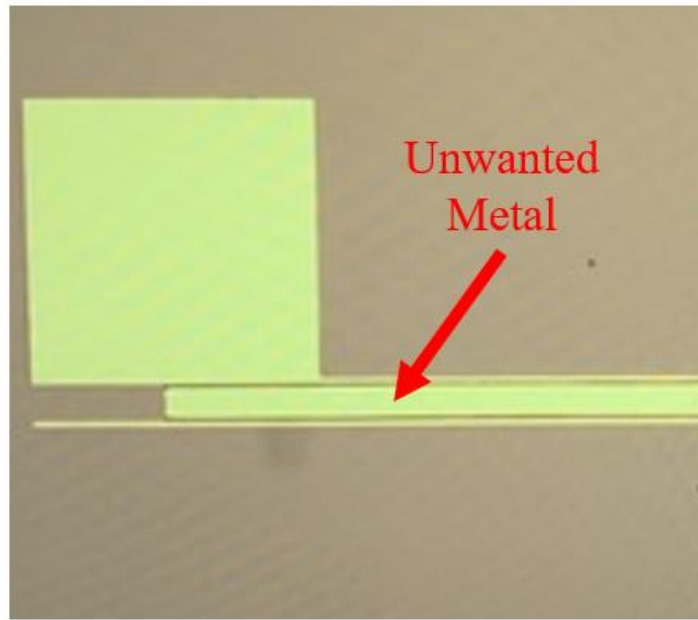


Figure 2.5-4: Bond pad of THz PCA showing unwanted metal after lift off.

Once lift off has been completed, the THz PCA must be mounted, and wire bonded to a chip carrier so that it can be electrically connected to the measurement setup for characterization. This process consists of gluing the chip into a carrier that has a hole drilled in the middle to allow for the pump laser to be incident on the surface of the PCA. To do this, a small amount of clear nail polish is applied around the hole of the chip carrier, then the carrier is lowered onto the surface of the PCA and left to dry for a minimum of 15 minutes before handling. The front and back of a carrier with a mounted PCA can be seen below in fig 2.5-5 (a) and (b) respectively.

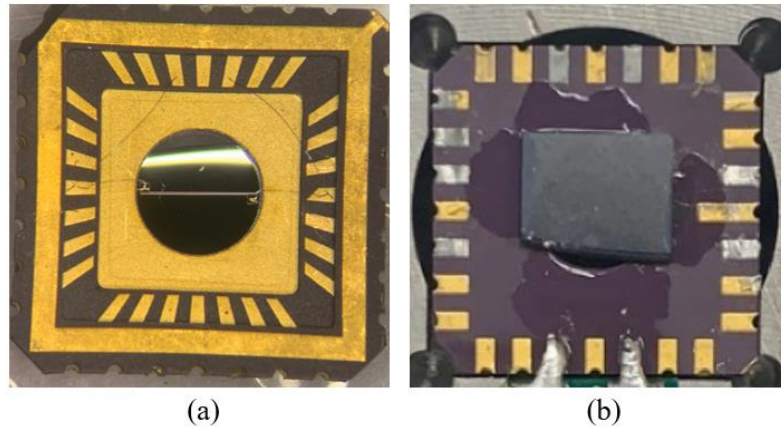


Figure 2.5-5: (a) shows the front of the chip carrier with THz PCA mounted on the back, the actual antenna is visible in the center through the hole in the carrier. (b) shows the back, with nail polish adhesive visible around edged of LT-GaAs chip.

The purpose of mounting the chip to the back of the carrier is to allow for a silicon lens to later directly contact the back of the THz PCA to focus and facilitate measurements of the THz beam that propagates through the chip and out the back.

Once mounted in a carrier, the PCA must be wire-bonded to the carrier. This is done using 1 mil Al wire bonding thread and an ultrasonic wedge bonder. The basic process for this procedure consists of touching one of the pads located around the edge of the front face of the chip carrier with the wire bonding wedge, which will ultrasonically press and secure one end of the bonding thread to the surface, then move the wedge to one of the bond pads of the THz PCA, completing the connection. In the case of these devices, two bonds are required, one for signal, and one for ground of the DC bias voltage. Below in fig 2.5-6 an example of a bonded chip with both wire bonds labeled can be seen.

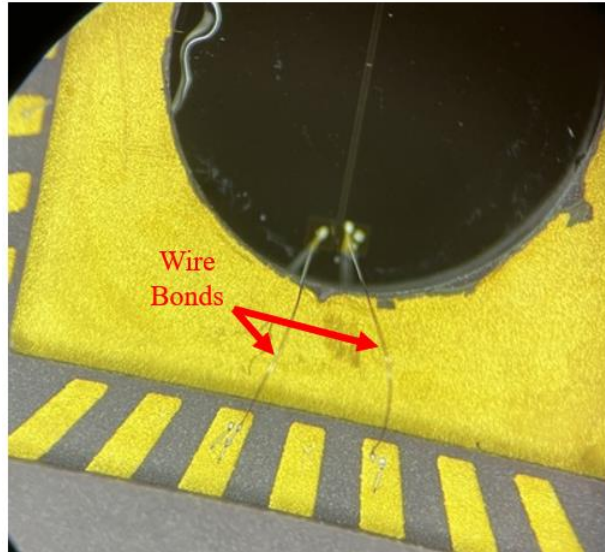


Figure 2.5-6: Wire bonds connecting the bond pads of a THz PCA to the chip carrier.

Once the LT-GaAs chip has been mounted and bonded to the chip carrier, it must be soldered to a PCB that can interface directly with the measurement system in order to receive the DC bias voltage. This PCB was designed as part of this thesis work, and is based on the commercial PCBs used for the measurement system that all PCA characterization in this work has utilized. The PCB design is very basic, using a U.FL header to connect from the measurement system, and simply connecting the signal and ground from the header directly to the two pads of the chip carrier that are wire bonded. It is not critical to ensure that signal or ground go to specific electrodes, as reversing the polarity of the bias voltage simply inverts the resulting THz pulse. Once soldered and secured in device mount, packaging of the THz PCAs is complete, and the devices are ready to be tested in the time-domain spectroscopy system.

## 2.6 Fabrication Conclusions

In conclusion, the fabrication of all THz PCAs described in this work consist of six main steps. First, the dimensions of the devices are defined in AutoCAD software and processed using Beamfox to apply PEC to the design. Second, the LT-GaAs samples are diced, and prepared for EBL by spin coating them in PMMA A2 or A4 electron beam resist with a thickness of 100nm or 200nm respectively. Third, the antenna design is patterned in the resist using a 50kV EBL system, and developed for 60 seconds in an MIBK:IPA solution. Fourth, the devices are metalized through thermal evaporations, depositing a 5nm layer of chromium followed by a 50nm layer of gold. Fifth, the device is soaked in acetone for a minimum of 12 hours to remove all excess metal leaving behind the metalized PCA design. Finally, the samples are mounted in chip carrier, wire bonded, and soldered to the interface PCB for electrical connectivity to the measurement system.

The step of etching is omitted from the final fabrication procedure due to the additional complexity and time it adds to fabrication. Furthermore, while etching can provide acceptable dimensional accuracy of small electrode features, it is less consistent and more difficult than using PEC, which proved the same results in less time, and less effort, requiring only a single EBL step to complete.

## **Chapter 3: TeraAlign System and Device Measurements**

### **3.1 TeraAlign System Overview**

In order to measure the performance of all devices throughout this thesis work, an open bench time domain spectroscopy system is utilized. This system requires careful alignment of an optical pump laser to the antenna gap of the THz PCAs and is hence referred to as the TeraAlign system.

Because the TeraAlign system uses a laser that is open to the room, it is important to wear proper eye protection to prevent any accidental exposure of the beam to one's eyes by stray beams. OD 4+ goggles should be worn at all times when in the same room of the system while the laser is turned on.

#### **3.1.1 TeraAlign Component Layout**

The TeraAlign system consists of two major sections, first, a set of optical components used to condition and steer the laser pulse, referred to as the optical section. The second part of the system consist of two alignment stages that are used to position the laser pulse in the gap of the THz PCAs, and then align the resulting THz pulse from the emitter to the detector for measurements, referred to as the THz section. Below in fig 3.1-1, a top-down view of the TeraAlign system can be seen with both sections, as well as the major components within each section labeled with numbers. Each numbered component will be identified and have its role in the system explained below. Additionally, an in depth review of the TeraAlign system can is done in [46].

The previously mentioned optical side of the system consists of the components labeled 1 through 9. The THz side of the system consists of components 10 through 16.



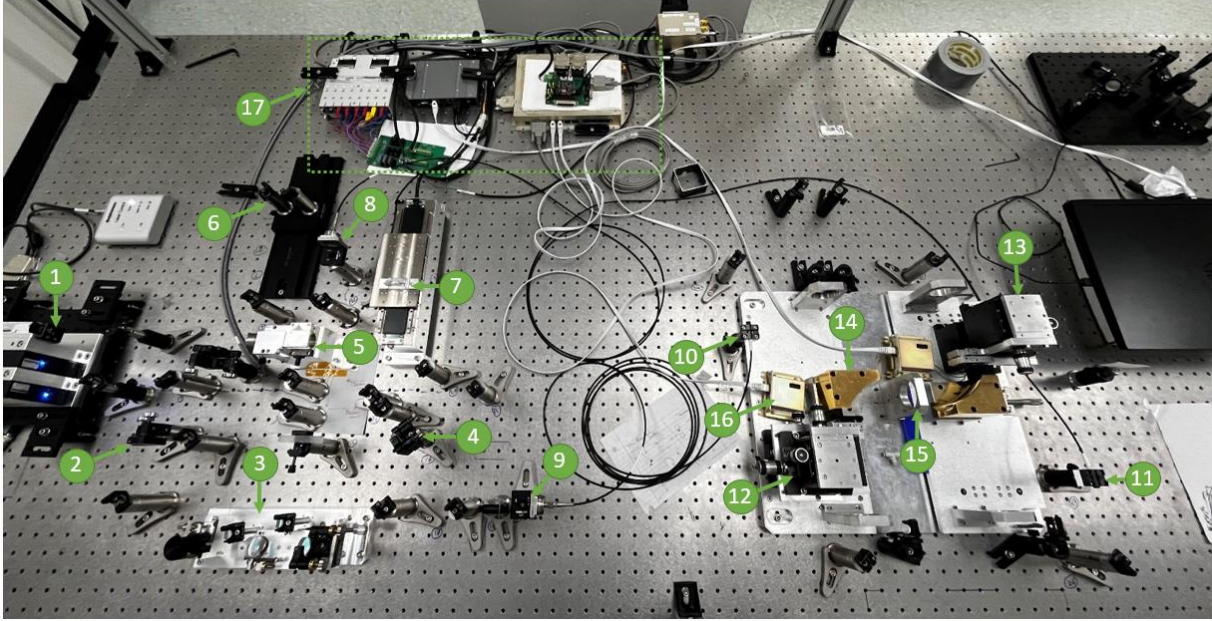


Figure 3.1-1: Top-down view of entire TeraAlign system showing critical components.

To begin, the (1) label points to the optical pump of the system, which is a 780nm femtosecond pulsed laser. This laser has a power output of  $\sim 85\text{mW}$  and feeds the entire system. By the time the laser pulse reaches the emitter and detector, the incident power is 5mW and 6mW respectively. Moving to (2), this component is a half-wave plate that horizontally polarized the laser pulse in order to match the polarization of the grating in the group velocity distributor (GVD), labeled (3). The GVD plays a critical role in the TeraAlign system controlling the compression of the temporal laser pulse, adjustments to the GVD can take the pulse width of the laser from several hundred femtoseconds, down to  $\sim 92$  femtoseconds, which can be measured using an autocorrelation device that will be covered in a later section. The component labeled (4) is a 60/40 beam splitter, which creates the two laser paths for emitter and detector, 40% of the power being sent down the emitter path, and 60% of the power down the detector path. Next, component (5) is

the RSDL. The RSDL is a fast delay line that consists of a rhomboid that is oscillated using a galvanometer. This oscillation can create a sweeping delay of up to 40ps, which creates the measurement viewing window. Without the RSDL oscillating, the measurement would be a single point in time, providing now useful data. The next component, labeled (6), is a manual delay line, this consists of two mirrors at 90 degrees to each other mounted on a sliding dove tail stage. This delay line takes an input beam and reflects an output beam parallel to the input. By sliding the stage forward or backward, the path of the beam on the emitter side can be shortened or lengthened respectively, which changes the resulting measured pulse's location in time. Now on the detector path, component (7) is nearly identical to manual delay line (6), however this line is motorized, allowing for a large sweep in delay. Using this motorized slow delay line, scans of ~700ps can be taken, which can aid finding a pulse when its location is not already known. Components (8) and (9) are fiber optic port inputs for the emitter and detector paths respectively. The input beams are carefully aligned to the center of these ports to carry the power to the THz side of the system.

Now on the THz side of the system, we begin with the output of the fiber ports. The output of the detector side fiber port is labeled as component (10), while the emitter side fiber port output is (11). (12) and (13) are identical stacked alignment stages used for laser and THz alignment of the emitter and detector respectively. These stages will be covered in depth in the following section of this thesis. The emitter side golden ellipsoidal mirror is labeled (14), this guides the THz emission from emitter to detector, including a second golden ellipsoidal mirror directly to the left of (14). The metal mount labeled (15) is used for introducing brass pinholes into the system, used for filtering low frequencies from the measured THz pulses, as well as ensuring the THz signal is passing through the precise center of the system. In a traditional THz spectroscopy setup, this is where a material sample would be placed to be characterized in the path of the THz beam. The

small box labeled (16) is the peripheral electronics that connect the PCB of the THz PCA to the electronics of the system, allowing for the application of the DC bias voltage. There is a similar peripheral box for the detector side not labeled but shown in the figure. Finally, not part of either section of the system, (17) points to a dashed box that surrounds all electronics controlling the system. These electronics are all designed and manufactured by TeraView LLC in the UK, who developed, installed, and provided training for the TeraAlign system. A simplified diagram of the TeraAlign system can be seen below in fig 3.1-2 showing a simplified laser path through both the optical and THz sections in (a) and (b) respectively.

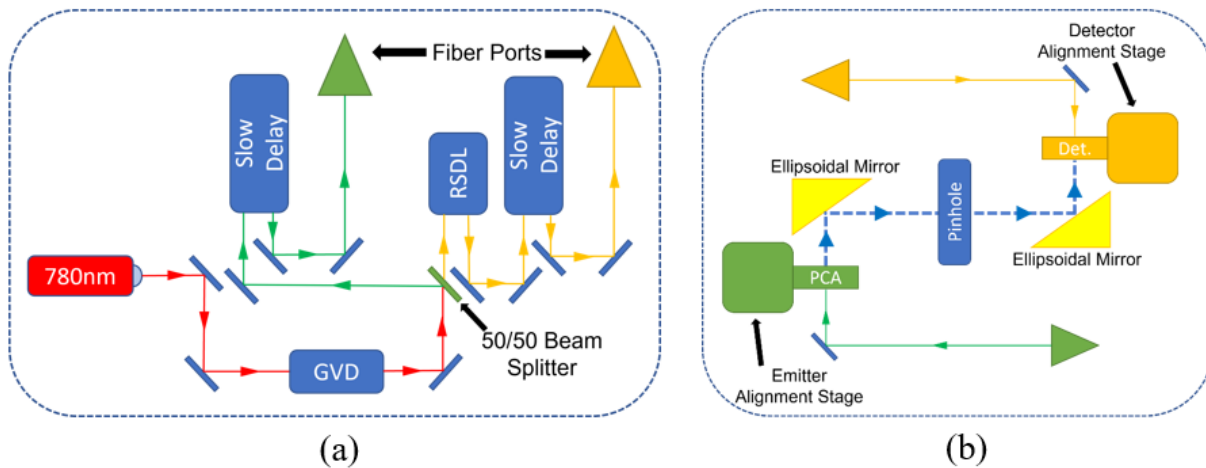


Figure 3.1-2: (a) simplified diagram of optical side. (b) simplified diagram of THz side.

### 3.1.2 TeraAlign PCA Alignment Procedure

The most critical task when measuring the performance of any THz PCA in the TeraAlign system is the alignment of the laser to the antenna gap, as well as the emitted THz beam from emitter and detector. This procedure consists of many steps that can be iterated numerous times to improve the overall alignment and ensure consistent data is gathered from many THz PCAs. The

first step in beginning an alignment is mounting a hyper hemispherical silicon lens, the actual THz PCA, and an NIR lens that focuses the laser beam from a ~3mm spot size down to ~5-micron spot size to fit in the electrode gap (4 x 5 microns). Below in fig 3.1-3 is a top-down view of the THz section of the TeraAlign system showing the mounting positions of the emitter, detector, and both NIR lenses.

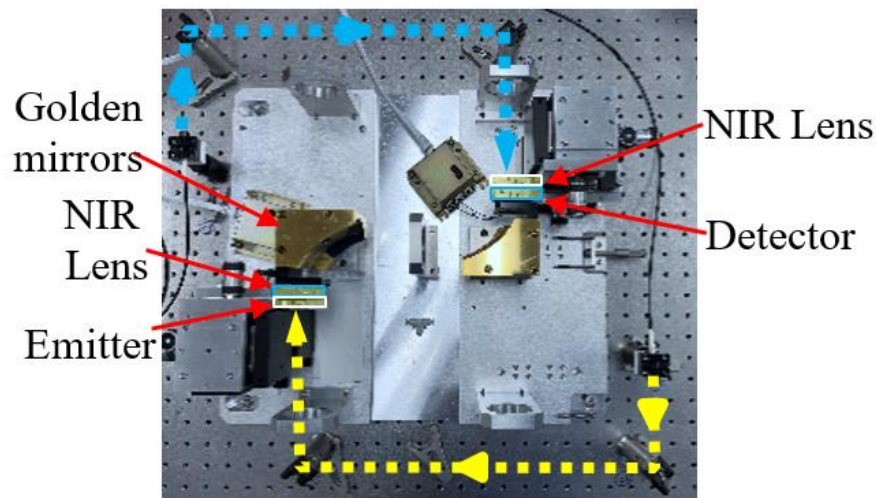


Figure 3.1-3: Top-down view of THz side of TeraAlign system.

In between the emitter (outlined in blue) is a hyper hemispherical silicon lens whose function is to focus the THz pulse emission from the emitter. This lens makes direct contact with the back of the LT-GaAs in the chip carrier and is held in place between the chip and a metal flexure. Next, the NIR lens (outlined in white), is then mounted behind the emitter. As previously mentioned, this lens focuses the incoming laser beam down to ~5 microns in order to confine the power to the gap of the PCA. Once mounted, the position of the laser on the surface of the PCA must be found and steered in order to ensure it is incident on the area between the electrodes. This

can be achieved using a beam splitter and a blank card to view a projected image of the PCA. Below in fig 3.1-4, the setup for the projected image can be seen in along with a diagram of the incoming and outgoing beams as well as images of bowtie and circular PCA electrodes as seen through an infrared camera.

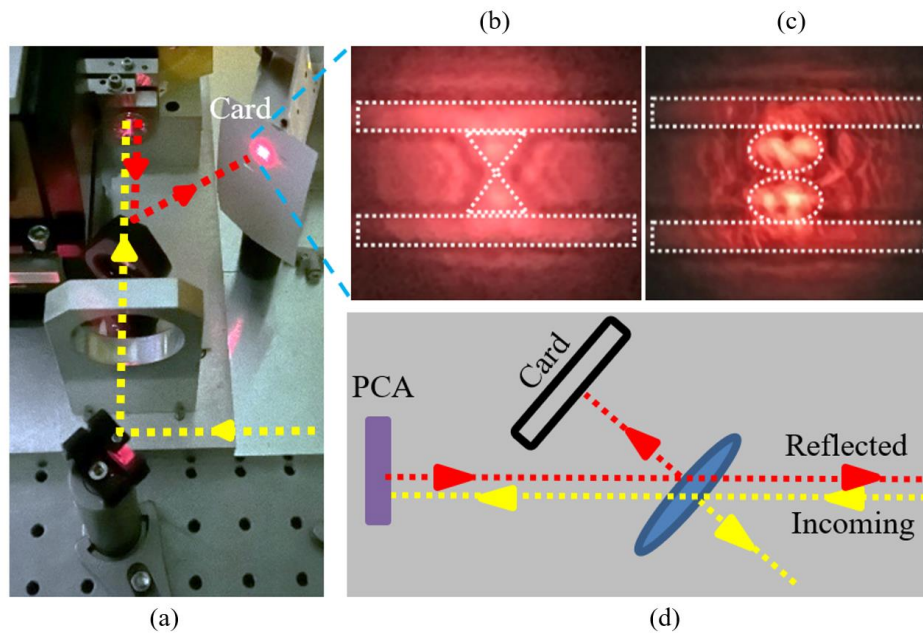


Figure 3.1-4: (a) beam splitter and card setup. (b) projected bowtie image. (c) projected circular image. (d) beam diagram for reflection alignment setup

Once the laser has been located, it must be adjusted and focused into the gap of the PCAs. This is done using the two alignment stages of the THz section of the TeraAlign system. Below in fig 3.1-5 is one of the stacked stages with its axes labeled.

The alignment stages consist of two identical sections, the top section is the laser alignment section, moving the NIR lens with respect to the PCA, which changes the location of the laser on the PCA. The bottom section is the THz alignment stage, which moves both the NIR



lens and the emitter at the same time with respect to the ellipsoidal golden mirror, essentially steering the THz beam in order to align it to the detector gap to be measured.

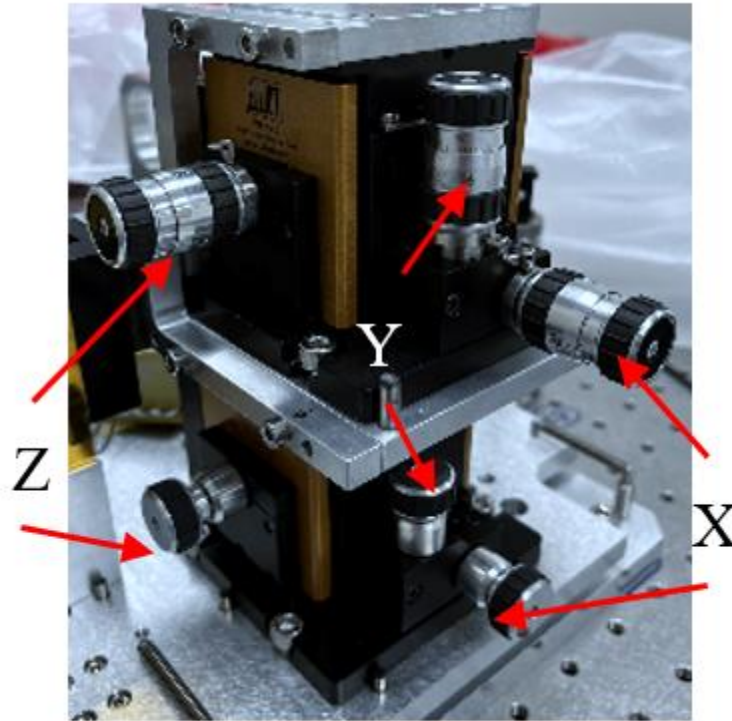


Figure 3.1-5: Stacked alignment stage with axis knobs for x, y, and z labeled.

When viewing the reflected image of the PCA electrodes, only the top stage (laser alignment) should be adjusted. The x and y axis knobs control the location of the laser on the surface of the PCA, while the z axis knob controls the focus of the laser. In the case of (b) and (c) in fig 3.1-4, the size of the laser spot can be seen to be much larger than the electrodes of the PCAs. This is only to take images of the reflected electrodes, in practice, the z axis adjustment of the laser alignment stage would be adjusted until the PCA surface lies within the focal plane of the lens.

Once the laser is centered in the gap, and focused to the point where it can no longer be adjusted by sight, the resulting signal can be viewed in order to further align the system.

In general, the first step after completing the laser alignment is to run what is called a slow scan within the TeraView provided TestPanel software. In order to operate any part of the system via the connected computer, it must first be initialized within a separate piece of software called TeraPulse. This is done through the following steps:

1. Open the TeraPulse software located on the desktop of the connected system laptop.
2. Login to the system using the provided password.
3. Under the top drop-down menu labeled “Instrument” select the first option called “Acquisition Setup”
4. Wait for the motorized delay line to complete its full sweep.
5. The system is now initialized and the TeraPulse software can be closed.

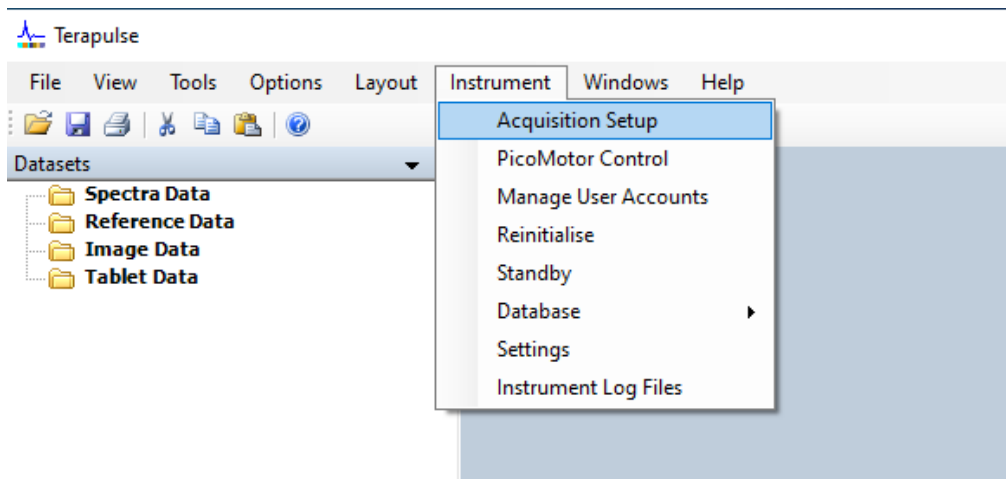


Figure 3.1-6: Main TeraPulse software screen showing location of acquisition setup.

Once the TeraAlign system has been initialized, the TeraPulse software can be closed, and the TestPanel software, which is also located on the laptop desktop can be opened. From here the system password can be entered and the “claim instrument” button can be pressed to allow control of the TeraAlign system.

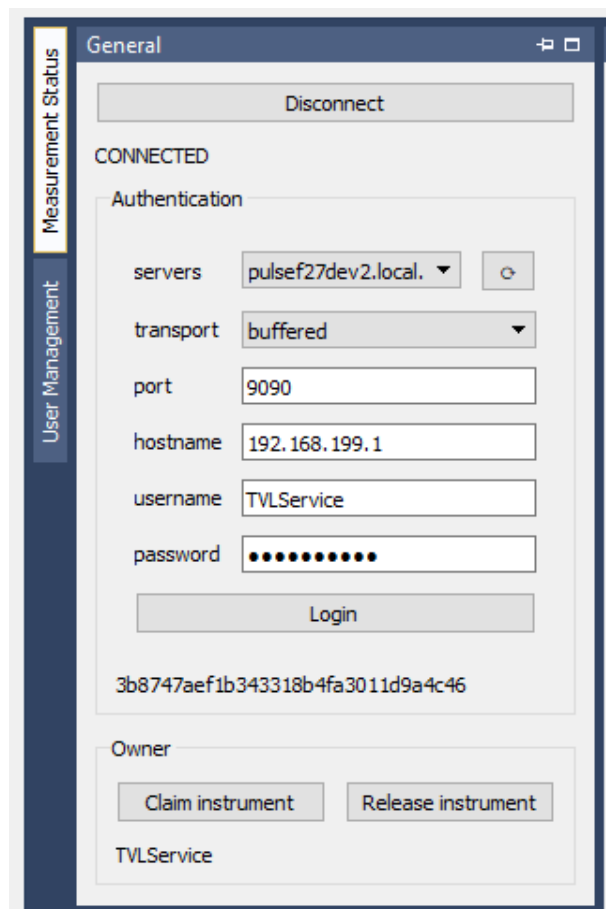


Figure 3.1-7: TestPanel login screen showing connected instrument.

Once claimed, the side tab labeled “Measurement Config” can be opened, and the “read” button pressed to populate the settings with the last scan run. From here, the drop-down menu labeled “Scanner” should be opened, and “SlowScan” selected. Once selected, pressing “write”



followed by “read” will ensure the correct settings options are available. From here the various settings can be adjusted, from number of averages at each point, to the start and stop positions of the motorized delay line. The maximum range of the motorized delay line is from -339ps to +461ps, although the entire range should rarely be scanned as under normal circumstances the THz pulse should lie somewhere between -100ps and +100ps. Once the scan settings have been entered, the “write” button, followed by the “commit” button can be pressed, storing the settings and sending them to the system. When ready, the “Run” button can be pressed and the scan will begin. Typical settings for a SlowScan can be seen below in fig 3.1-8.

The screenshot shows the 'Measurement Config' window with the following settings:

- ID:** 1537
- Name:** Measurement name
- Description:** Measurement description
- Module:** Transmission (Core)
- Scanner:** Slowscan
- Co-averages:** 2
- Optical Delay Start:** -100.000
- Optical Delay End:** 100.000
- Number of points:** 2049

The JSON configuration on the right is as follows:

```
{
  "_class_": "tvlsystem.meas_config.ActiveMeasConfig",
  "description": "Measurement description",
  "id": 1537,
  "module_name": "Transmission (Core)",
  "name": "Measurement name",
  "scanner_config": {
    "_class_":
      "tvlsystem.acquisition_params.SlowsanAcquisitionParams",
    "coaverages": 2,
    "number_of_points": 2049,
    "optical_delay_end": 100.0,
    "optical_delay_start": -100.0,
    "waveform_rate": 15.0
  },
  "scanner_name": "Slowsan"
}
```

Buttons at the bottom include 'read', 'write', 'Revert', 'Commit', and 'Modified'.

Figure 3.1-8: Expanded measurement config menu with various settings for SlowScan.

Once completed, the measured data will be displayed in the main window, and if the laser was aligned well, an obvious THz pulse should be seen. Zooming into the plot, the location in time

that the pulse occurs at can be recorded for use in the TeraPulse software. An example of a completed SlowScan can be seen below in fig 3.1-9.

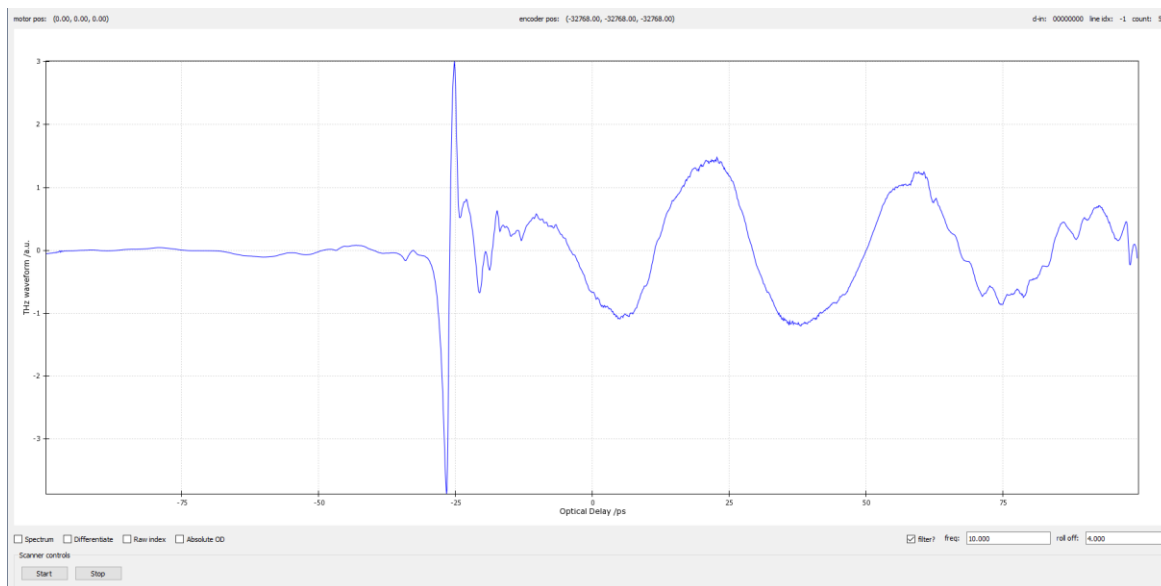


Figure 3.1-9: SlowScan of THz PCA from -100ps to 100ps with pulse occurring around -15ps.

After the pulse is located, the TestPanel software can be closed, and the TeraPulse software can be opened. TeraPulse is where the majority of measurements and alignment takes place, and it where live scans, referred to as SpectraSeries scans take place. Even though the system has already been initialized, the acquisition setup must be repeated in order to claim the instrument in TeraPulse, because the system has already been initialized however, the motorized delay line will not do a sweep. Now, the green play button shown below in fig 3.1-10 can be pressed to begin a live SpectraSeries scan. This is where the lower section of the alignment stages, or THz stage, comes into play. First, the pulse should be centered in the viewing window by using the left and right stage movement buttons in the right-side setting window within TeraPulse. Once centered,

the pulse shape should be optimized until it is as narrow as possible. This is done using only the top (THz) section of the alignment stage. Once initially optimized, the bottom alignment stage will only be used while a 1mm brass pinhole is placed into the mount between the golden mirrors. In general, introducing this pinhole will reduce the signal amplitude anywhere from 50-90% depending on the initial alignment position of the THz beam. In cases where the beam is extremely misaligned, the pinhole may completely block the signal. With the pinhole in place, the x and y axis knobs of the bottom section of the alignment stages can be manipulated in order to position the beam in the center of the pinhole.

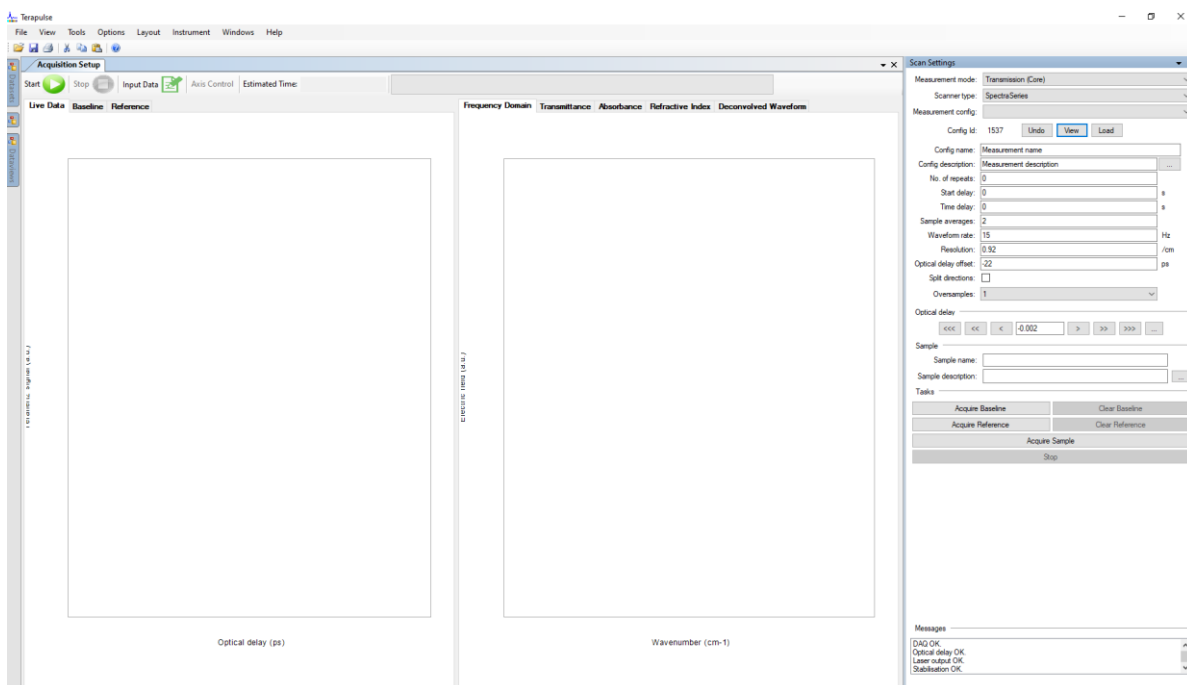


Figure 3.1-10: Main measurement screen within TeraPulse software.

When using the reference devices provided by TeraView, a ~30% cut in the signal, as well as a dip in the beginning of the spectrum should be expected when an acceptable alignment has

been achieved. Below in fig 3.1-11 (a) and (b) are examples of an aligned signal with and without the 1mm pinhole respectively. Once the signal is passing through the pinhole successfully, it can be removed, and the top section (laser) of the alignment stages can be further adjusted to increase the signal amplitude. A rule of thumb for aligning the THz PCAs in the system are to always use the pinholes when adjusting the THz stage, and to never use the pinholes when adjusting the top stage. Further, the top stage will mainly change the amplitude of the signal, while the bottom stage will have a much more drastic effect on the overall shape of the pulse.

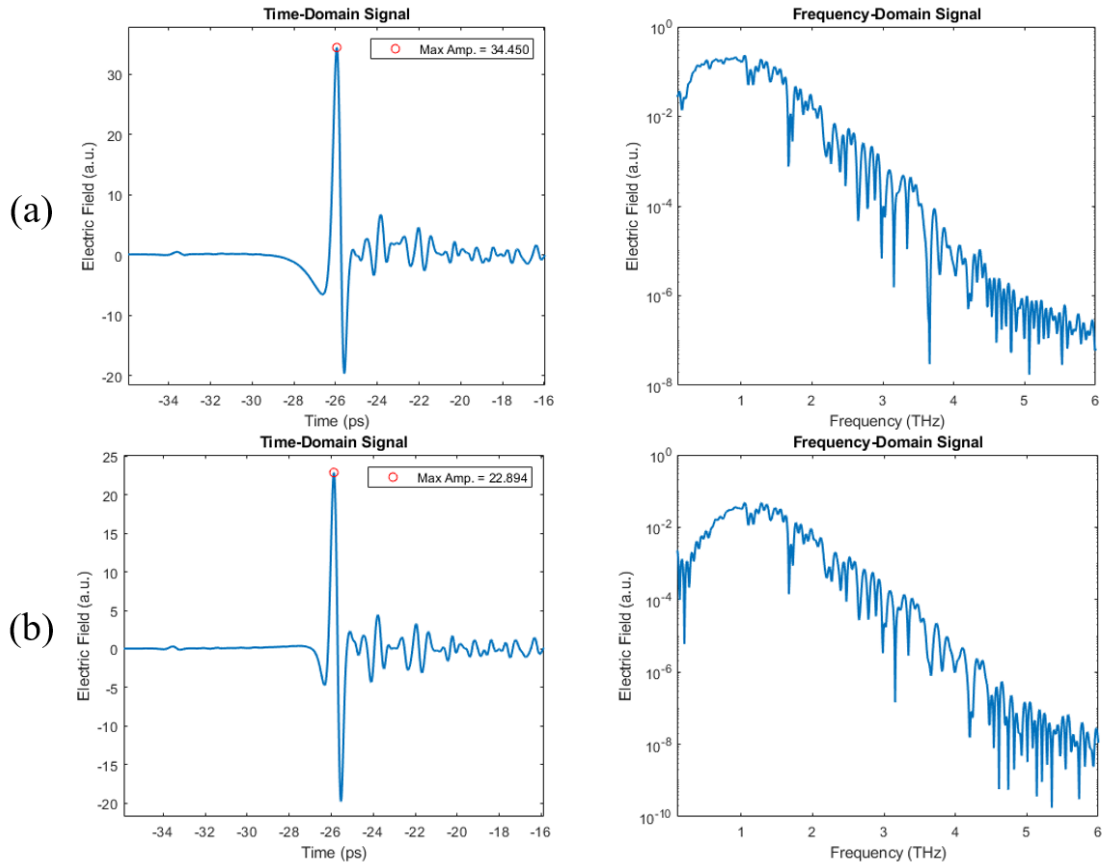


Figure 3.1-11: (a) time and frequency domain plots of aligned reference emitter with no pinhole. (b) same emitter and alignment with 1mm pinhole in signal path

After completing the alignment with the 1mm pinhole, removing it, and optimizing the laser position again, the 0.5mm pinhole can be placed in the system and the same steps can be repeated. Again, ~30% decrease in signal amplitude from the 1mm pinhole should be observed when using the 0.5mm pinhole, along with a more drastic dip in the beginning of the spectrum. Using these general rules, any THz PCA can be aligned using the TeraAlign system. It is important to note that the rule of a 30% decrease in signal strength between each pinhole is only valid for the reference emitters provided by TeraView, for the devices fabricated and measured in this thesis, 50-60% reduction in signal is typical, which is a value that was found experimentally through many alignment trials.

### **3.2 LT-GaAs THz PCA Voltage and Power Study**

One major factor that effects the measured THz pulse amplitude and spectrum is the DC bias voltage as well as the incident laser power. Typically, a laser power of 6mW at the emitter and 5mW at the detector is used. In order to further understand the effect of changing powers and voltages, multiple measurements at various powers and voltages under the same alignments are performed. To vary the laser power, a continuously variable glass attenuator is placed in the path of the beam directly before the input of the fiber port.

The experimental procedure for this study consists of first obtaining a good alignment of the emitter of interest, in the case of the following data, the standard bowtie electrode shape, with no cutout features is used. Once the alignment is achieved, the chosen variable can be changed and measurements can be taken at each point. All measurements shown in this work use 1800 averages to ensure the minimum amount of random fluctuations of the signal and spectrum.

First, in the case of varying laser power, increments of 0.5mW are taken, starting at 0.5mW and increasing to the standard 6mW value. At each point the peak value of the pulse is recorded.

Below. These values have been normalized to the maximum and plotted to show the effect of incident laser power on the resulting THz pulse.

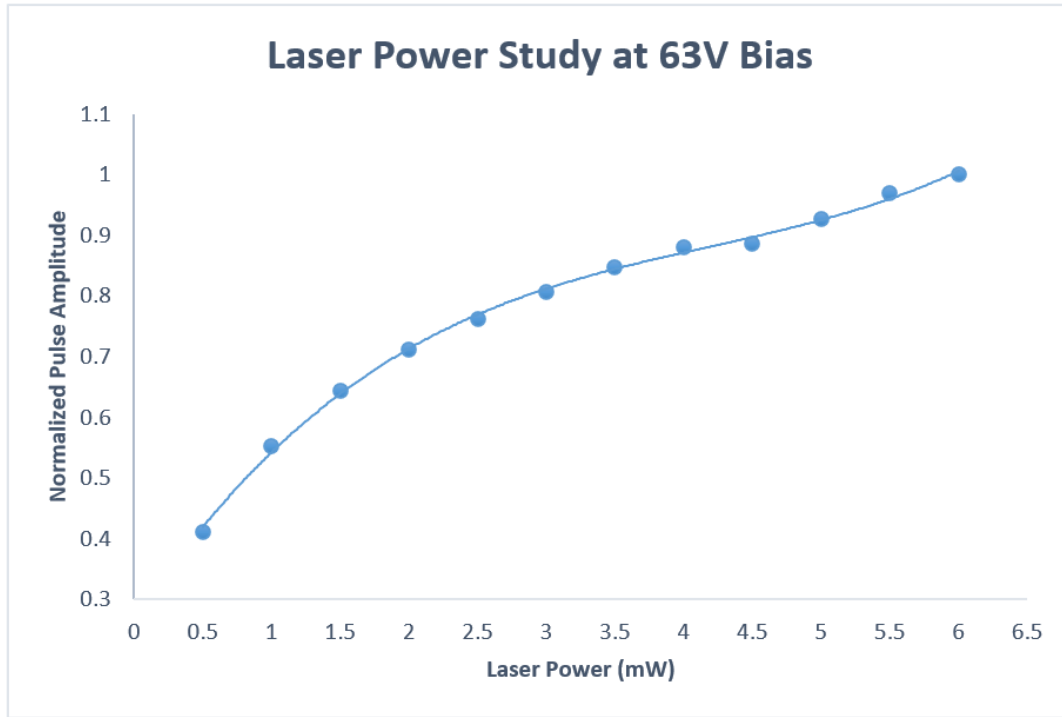


Figure 3.2-1: Normalized pulse amplitude vs laser power from 0.5mW to 6mW.

It can be seen from the plot that as the laser power increases, the pulse amplitude immediately begins to approach a linear region, starting at 3.5mW of incident power. While the device does not show saturation even at 6mW, the power is not increased past this point to avoid damage to the device.

In a similar way, the DC bias voltage applied to the devices can also be varied. The bias voltage accelerates the free carriers created by the incident laser, and has a drastic effect on the amplitude of the THz pulse. The voltage of the DC bias voltage is also an important factor to consider when measuring devices of materials other than LT-GaAs, such as the BP devices

fabricated by Dr. Churchill's group, the measurements of which were performed as part of this thesis work, seen in Appendix B. In the case of these devices, using the same bias voltage as the LT-GaAs devices can burn the more sensitive BP flakes, rendering the devices dead before any measurements can happen. For this study, the DC bias voltage factor is input into the TestPanel software as 0.1, and varied by 0.2 up to 1.5, which is the maximum used for all measurements. It should be noted that these voltage factors are the just the inputs to the system. There is a transformer that multiplies the voltage factors by 42, meaning at a system voltage factor of 1.5, the emitter will see 63V. In the same fashion as the power study, each measurement will have its peak value recorded, then the data is normalized to the maximum and plotted to show the trend voltage has on the pulse amplitude. From this data, it can be concluded that the voltage has a near linear effect on the pulse amplitude. Again, the voltage is not increased past 63V to prevent damage to the devices.

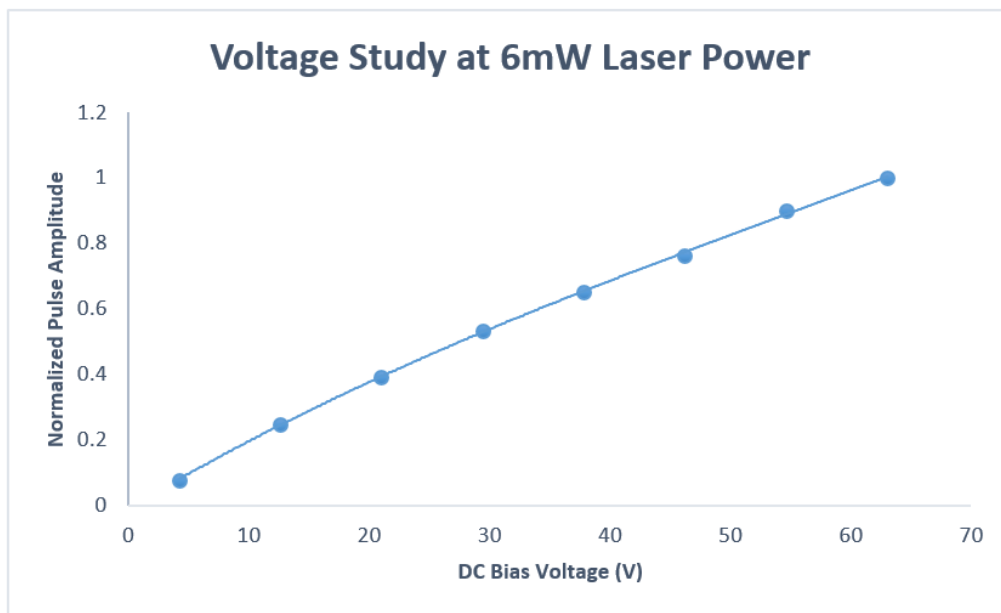


Figure 3.2-2: Normalized pulse amplitude vs DC bias from 4.2V to 63V

Overall, the voltage of the DC bias and magnitude of incident laser power play a vital role in the performance of the THz PCAs. In terms of alignment, ensuring that both values are at their maximum values (63V and 6mW) makes achieving a good alignment easiest, as the pulse will be well above the noise level. However, as previously mentioned, when aligning devices that cannot handle high laser powers or bias voltages, alignments become much more difficult as differentiating between system noise level and the THz pulse becomes challenging.

### 3.3 LT-GaAs THz PCA Polarization Study

The polarization of the LT-GaAs THz PCAs in this work is also an important factor to understand. In general, dipole antennas will result in linearly polarized emissions. As these PCAs are dipole antennas, they will have linear polarized THz pulses as well. Although the polarization of these antennas is mainly in the directions from one electrode tip to the other, there is some amount of radiation in the opposite direction, that is, parallel to the transmission lines. Further, the detector in the TeraAlign system is also linearly polarized, making it critical to ensure that the LT-GaAs antennas being characterized are oriented such that their major polarization is aligned.

In order to quantify both polarizations, a quartz crystal with a thickness of 1mm, which interacts with the THz pulse at ~3THz in order to rotate the polarization to measure both horizontal and vertical polarizations. Quartz is a uniaxial birefringent crystal that will rotate the polarization of radiation at a specific frequency according to equation 3.3-1 [53]:

$$t = \frac{\lambda}{2 * (n_e - n_o)} \quad \text{Equation 3.3-1}$$

In this equation,  $n_e$  and  $n_o$  are the refractive indices of the extraordinary and ordinary axes respectively which are given in [53],  $t$  is the thickness of the quartz, and  $\lambda$  represents the wavelength that the quartz will rotate.



Table 2: Refractive indices of x-cut Quartz

Refractive Indices at 3 THz		
Material	$n_o$	$n_e$
Quartz	2.132	2.181

To isolate each individual polarization, wire grid polarizers are used. The specific wire grid polarizers used in this work are from Microtech Instruments, model G50x20, which allow ~97% of the transmission to pass when the polarization is perpendicular to the wires, and ~2% to pass when the polarization is parallel to the wires with a bandwidth of ~0.05-3 THz. Wire grid polarizers are widely used in THz transmission experiments as shown in [54]–[56]. In this experiment, horizontal polarization refers to the main polarization direction, when the device is aligned with the polarization of the detector, while vertical refers to being rotated 90 degrees from the main polarization.

In the setup shown below, the first wire grid polarizer isolates either the horizontally or the vertically polarized THz pulse. Next, the quartz crystal can be oriented to either pass the signal with no change to the polarization, or rotate it by 90 degrees, essentially changing it from horizontal to vertical, or the reverse. A 3D printed mount is used to hold the quartz crystal within the TeraAlign pinhole mount while allowing for rotation. The second wire grid polarizer is used to further clean the signal entering the detector to ensure only horizontal polarized radiation is read out and will never be rotated. In terms of location of the wire grid polarizer within the system, polarizer 1 sits directly after the emitter, while polarizer 2 sits directly before the detector.

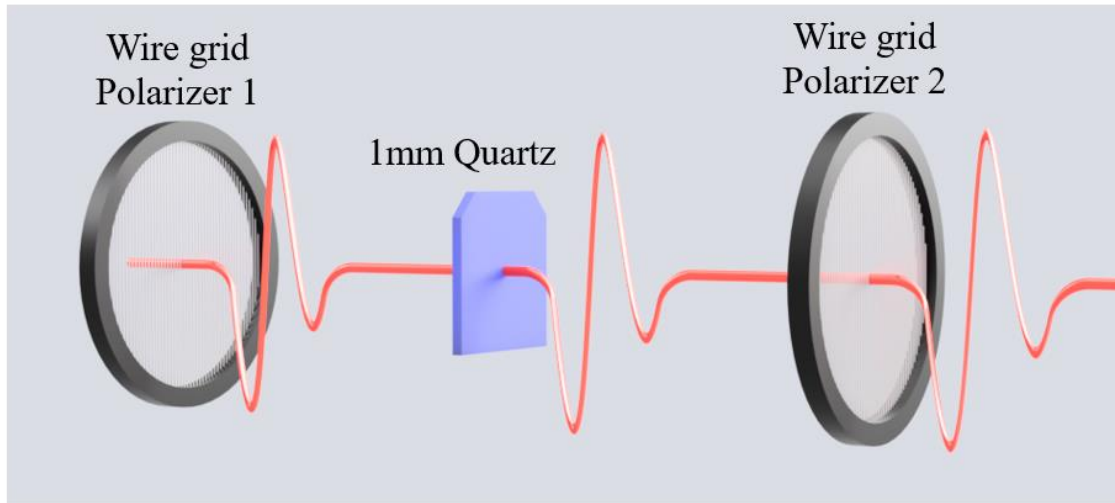


Figure 3.3-1: Render of experimental setup for polarization study.

To obtain the presented data, two experiments are performed for each electrode shape of LT-GaAs emitter, as well as on the commercial device from TeraView. First, wire grid polarizer 1 is rotated to pass the horizontally polarized portion of the THz pulse. The quartz crystal is then rotated to the axis that does nothing to the signal. Finally, wire grid polarizer 2 cleans the signal further and the detector measures the isolated horizontally polarized THz pulse. To isolate and measure the vertical polarization, the wire grid polarizer is rotated by 90 degrees so that it now passes only the horizontal portion of the THz pulse. Next, the quartz crystal is oriented so that it rotates the polarization of the signal; this is done so that the detector will be able to measure it. Now that the signal has been rotated back to horizontal, wire grid polarizer 2 further cleans the signal, and the detector measures it. These two experiments are repeated for each electrode shape and the resulting spectrums are plotted.

In all cases, the blue shaded bands in fig 3.3-2 represent the approximate areas affected by the quartz rotator. The difference in spectral magnitude between the horizontal and vertical

polarizations in all cases is nearly 2 orders of magnitude. These results verify that all the LT-GaAs emitters, including the commercial device from TeraView are heavily linear polarized in the direction perpendicular to the transmission lines, that is, from one electrode to the other.

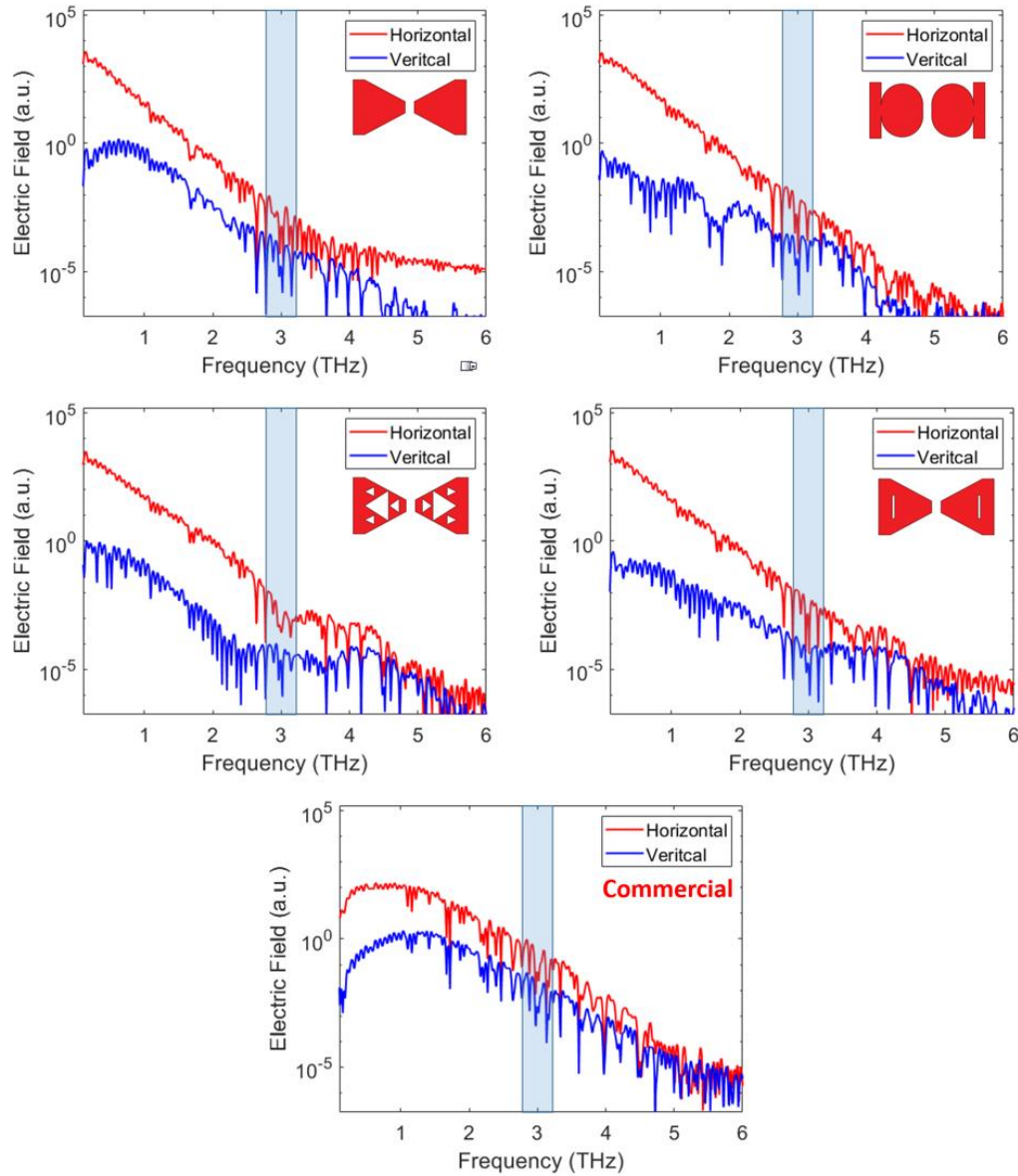


Figure 3.3-2: Polarization data for all four LT-GaAs electrode shapes and commercial emitter.

### 3.4 LT-GaAs THz PCA Electrode Shape Comparison

So far, the effects of different DC bias voltages and incident laser powers, as well as the quantification of the horizontal and vertical polarization magnitudes have been presented. Here, a comparison and analysis of the time domain and spectrum of each THz PCA electrode shape will be shown. In all following cases, the procedure consists of achieving the best possible alignment for each emitter, then taking a measurement with 1800 averaged samples and plotting against all shapes to determine the differences in pulse amplitude and shape, as well as bandwidth for each PCA design. For all PCAs multiple alignments are done, and the best case for each is selected to be presented. For alignment, each device is aligned with the aid of a 1mm and 0.5mm brass pinhole to ensure that the signal is centered, and that THz frequencies are being emitted.

When viewing the data in fig 3.4-1, the first thing to take note of is that in the case where there is no pinhole shows the pulse amplitude of all four emitters fabricated in this work outperforming the commercial emitter in terms of pulse amplitude, but not spectrum. This leads to the conclusion that there low frequency components outside of the THz band contributing to the overall pulse amplitude, but due to the spectrum only being calculated from 0.1 to 6.5 THz, they are not shown, leading to the large performance gap between the four emitters and the commercial emitter in the spectrum. Moving to the second row of the figure, the 1mm pinhole cuts the blocks frequencies below 0.175 THz, in doing this the commercial emitter is now outperforming all other emitters in terms of pulse amplitude and spectrum, although the gap between spectral performance is now closing. Finally, in the bottom row, showing measurements with the 0.5mm pinhole in the path of the THz signal, the commercial emitter further outperforms all other emitters in terms of time and spectrum. Overall, this solidifies the conclusion that there are some low frequency components contributing to the pulse amplitude of the fractal, bowtie, circular, and slotted LT-

GaAs THz PCAs. These low frequency components also reduce the optical to THz conversion efficiency, which explains the gap in spectral magnitude between the commercial emitter, and the other four shapes.

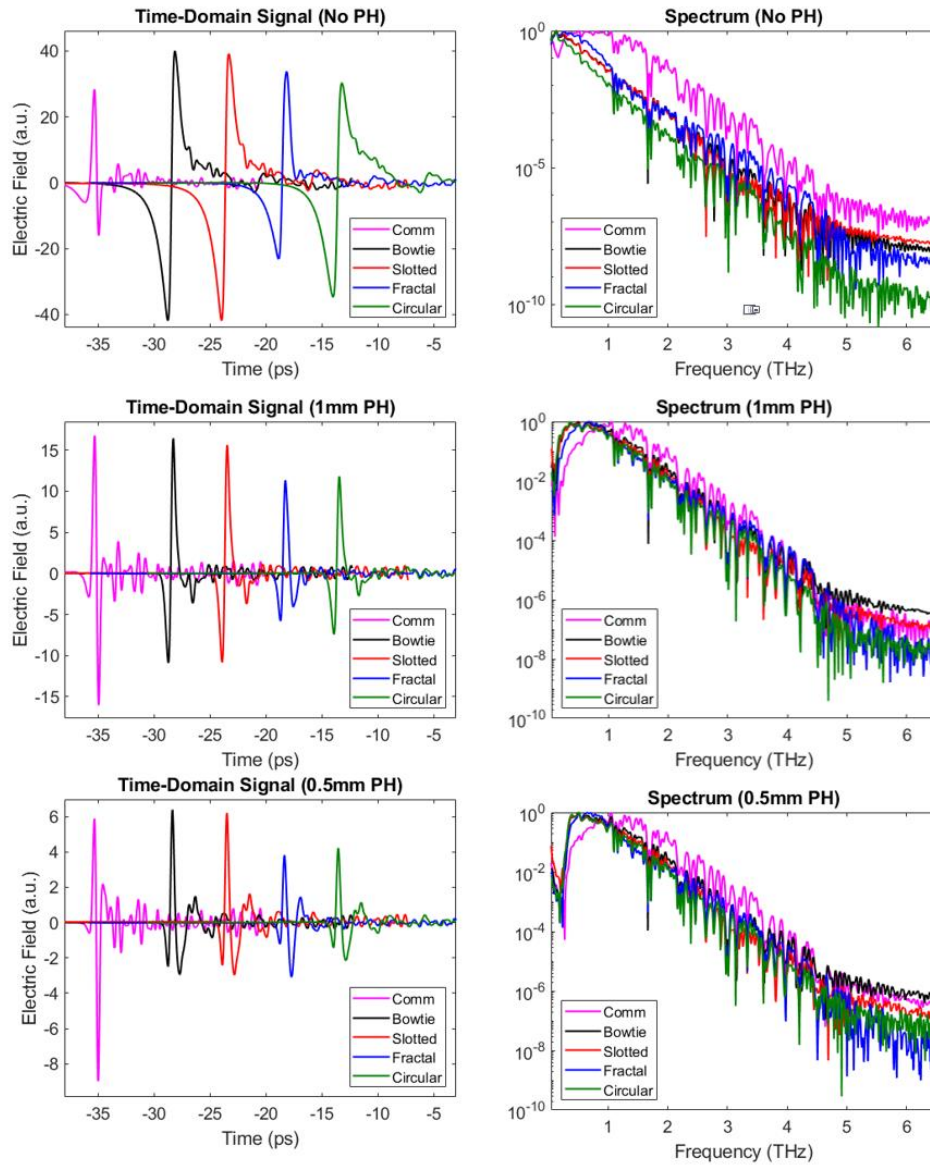


Figure 3.4-1: Time domain and spectrum data from all four electrode shapes including commercial emitter.

Further, ignoring the commercial emitter and focusing on the four emitters fabricated as part of this thesis, it can be seen in all figures that the standard bowtie, with no cut out features, outperforms all other shapes across the board. The ranked performance of the remaining emitters in order is slotted, circular, and finally fractal. The fractal emitter has the most complicated electrode feature shape, which results in lower tolerances for fabrication defects, which could contribute to the lack of real-world performance.

To further study the bandwidth of the four THz PCA electrode shapes, the designs were simulated using COMSOL Multiphysics in order to extract the resulting surface photocurrent pulse caused by the incident laser on the LT-GaAs surface, as well as the S11 parameter to better understand the effect of electrode shape on the bandwidth of each antenna. The results of these experiments have been published and discussed in detail in [18].

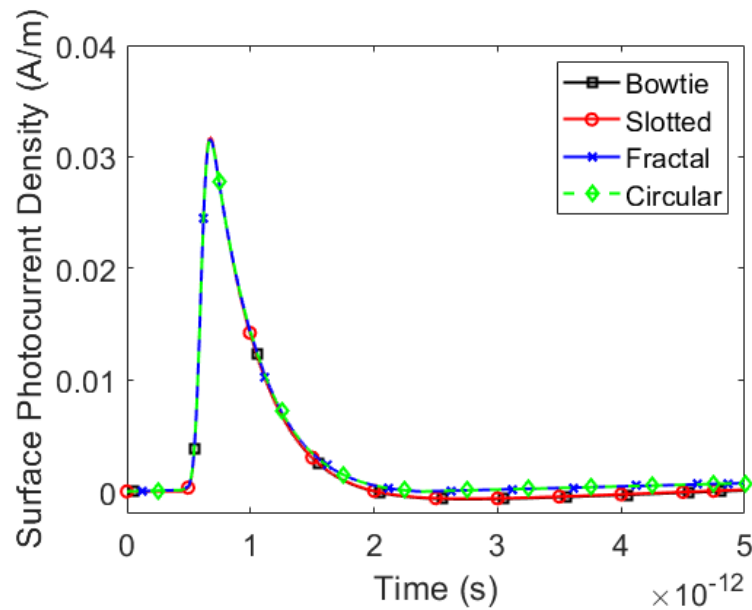


Figure 3.4-2: Simulated surface photocurrent density for all four electrode shapes [18].

The figure above clearly shows that the electrode shape has very little effect on the resulting surface photocurrent density. This is an expected result due to the identical gap, or active area, dimension across all 4 designs.

Further, the S11 parameters, as well as the spectral representation of the above surface photocurrent densities were simulated for all four designs and plotted together for comparison. It is important to note that the THz signal in fig 3.4-3 below is experimentally measured, while the S11 and photocurrent are computationally modeled.

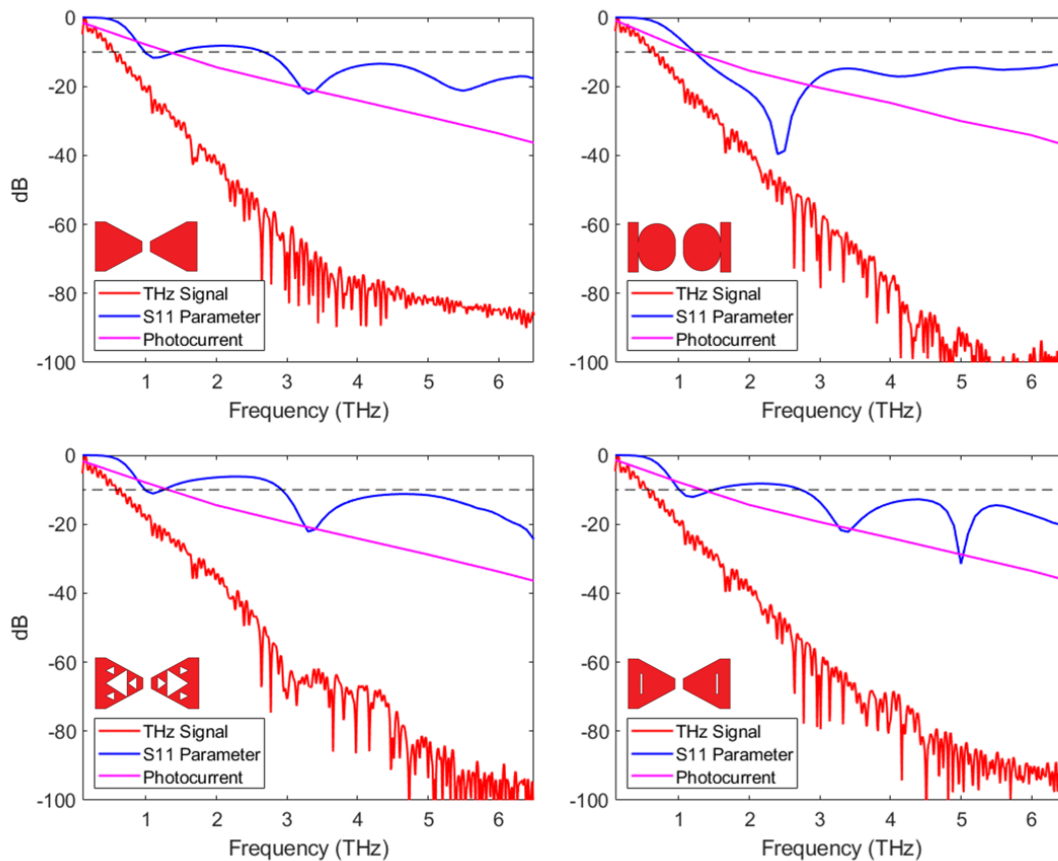


Figure 3.4-3: Simulated and experimental results of spectrum, S11, and photocurrent study for all four electrode designs of THz PCAs as reported in [18].

The plot reveals that the circular electrodes provide the widest bandgap of all electrode designs, with a value under -10dB beginning at ~1.2 THz and extending past 6 THz. While the S11 parameter seems to dictate the resulting spectrum in the beginning of the measurements, as the surface photocurrent drops off, the spectrum also falls to the system noise level in all devices.

### **3.5 LT-GaAs THz PCA Measurement Summary**

In summary, the effect of DC bias voltage, the quantification of polarization directions, as well as a comprehensive study of the THz pulse time domain and spectrum between the four presented electrode designs and TeraView provided LT-GaAs based commercial emitter has been presented and analyzed.

First, incident laser power reaches a linear region in terms of increasing pulse amplitude at ~4.5mW. For DC bias voltage, the entire testing range performed linearly in increasing the pulse amplitude, and a max voltage of 63 V. Next, using wire grid polarizers and a quartz half-wave rotator, the horizontal and vertical polarizations of the THz pulses from each device are isolated. This data shows that all 4 devices, and the commercial antenna are heavily linearly polarized in the direction of the DC bias field, that is, from one electrode to the other, showing around 2 orders of magnitude difference in spectrum between polarizations.

Finally, a comparison of each electrode shape shows that the performance of the bowtie antenna is greater than the four other designs in real-world measurements. However, computational analysis shows the largest bandwidth belonging to the circular electrode design. From the measurement analysis it can also be concluded that there is more low frequency contributions in the THz pulses of the four emitters fabricated for this work than in the commercial device from TeraView



## Chapter 4: LT-GaAs THz Array Feed Network and PCA design

### 4.1 Antenna Array Background

Antenna arrays are devices consisting of many individual antennas connected to interact with each other as to perform as a single device. There are many applications where antenna arrays are advantageous compared to single element antennas. In the communication industry, specifically 5G communication in the microwave and millimeter wave frequency bands, where signal strength and blocking is a major concern, the ability to beam steer and scan using phased arrays is a critical step in developing successful communication systems [57]–[59]. Imaging and radar system take advantage of antenna arrays to speed up scan times, improve resolution, and the accuracy of detection [60]–[62]. One major advantage to using phased antenna arrays over a single antenna is the speed at which a beam can be steered and scanned. While a conventional antenna would need to be physically redirected, either by moving the device, or using mirrors to steer the emission, a phased antenna array can change the angle of its beam on the order of microseconds by manipulating the antenna feed to specific elements within the array [63].

All of the array work discussed in this thesis will be of two element arrays, with all work being done experimentally. In terms of theory for a two-element antenna array. The electric field at any point can be calculated by finding the electric field at that point for a single element and multiplying it by the array factor for the array. The array factor for a two element array is function of the geometry and phase of the excitation [64]. The normalized array factor (AF) can be calculated using equation 4.1-1.

$$AF = \cos \left[ \frac{1}{2} (\beta d \cos(\theta) + \alpha) \right] \quad \text{Equation 4.1-1}$$

Where  $\beta$  is the wavenumber,  $d$  is the distance between the two elements, and  $\alpha$  is the difference in phase between the two excitations. In the case of the optical feed of THz PCAs, the phase of excitation has a direct relationship to the path length of the beam from the laser to the PCA, which has been carefully adjusted to ensure both elements have identical phases. This requires careful control of path lengths when using separate beams to excite array elements.

## **4.2 THz PCA Array Feed Network Approaches and Challenges**

As THz band devices will seemingly play a major role in the development of next generation communication systems, it follows that the development of efficiently fed THz antenna array must happen. THz PCAs face a unique challenge when it comes to creating these arrays in the form of the feed network. In lower frequency bands, such as millimeter wave arrays, the size of the antenna allows for the design of feed networks to be integrated using the same technology that creates the actual antennas. For example, in the case of a phased array of patch antennas, the feed network connecting each element can be formed using traditional lithography techniques, electrically connecting and feeding each element within the array [65]–[67]. This is not the case for THz PCAs, which use an optical feed network, consisting of some type of optical pump to feed the antenna elements due to the nature of photoconductive devices. There are several approaches to feeding an array of THz PCAs, from using an array of micro lenses, flood exposing the entire array, to scanning the optical pump between individual elements [68]–[71]. One critical point of all feed networks designed for THz PCA arrays is the efficiency at which the optical energy can be delivered to the active area of the array elements. As discussed throughout this thesis, when exciting a single antenna element, all the incident power is focused into the antenna gap between the electrodes. In the case of an antenna array, efficiently delivering the optical power to each element becomes difficult due to the size and spacing of the elements.

One approach is optical beam scanning to each element within an array, to essentially select individual channels within the array. This can be particularly useful in the case of THz imaging systems, where each element in the array can serve as a pixel, and an optical pump can quickly scan the entire array, drastically speeding up the time of image acquisition [72]. This approach can be useful in the case of a characterization system that does not utilize a particularly high-power laser, making flood exposure and micro lens array feeds less attractive. This feed technique is most useful in imaging systems, rather than in a communication application, as sequentially probing individual elements of the array means the device is not capable of true beam-steering. However, this approach can be improved by using special light modulators (SLM) to form beam fronts and create multi focal points of light to excite multiple elements at once as seen in [72], [73].

Flood exposure of THz PCA arrays is another approach to feeding. This technique is the simplest of any feed network. By creating a laser spot size that encompasses the entirety of the THz PCA array, all elements are simultaneously excited. However, due to the most THz PCAs being in the micro to nano scale, much of the optical pump power is incident on non-active areas of the substrate. This can be alleviated by creating densely packed nano arrays of THz PCAs to optimize the efficiency of the optical absorption into the gaps of each element as seen in [69].

Finally, micro lens arrays can be used to further improve the efficiency of flood exposed THz PCAs. By using an array of micro lenses aligned with the gaps of each element, a larger area of light can be focused into the gaps of each antenna. This approach is more practical for THz PCA arrays on the micro scale as discussed in [35]. This feed design does require the fabrication and alignment of a micro lens array to the gaps of each antenna, which adds complexity to device, but can be implemented into existing time domain THz spectroscopy systems without the need to add additional optics besides the lens array.

### 4.3 LT-GaAs THz PCA Array Design and Fabrication

The arrays fabricated as part of this thesis work follow an identical fabrication process to as the single element PCAs. Using EBL, thermal evaporation, and wire bonding realize the devices. Beyond this the arrays use identical chip carriers and fit into the same mounting bracket as the single element PCAs. All devices consist of two identical dipole elements, using the bowtie design with no cutouts. Below in fig 4.3-1, the full design of the arrays, as well as a zoomed section focused on the active areas can be seen.

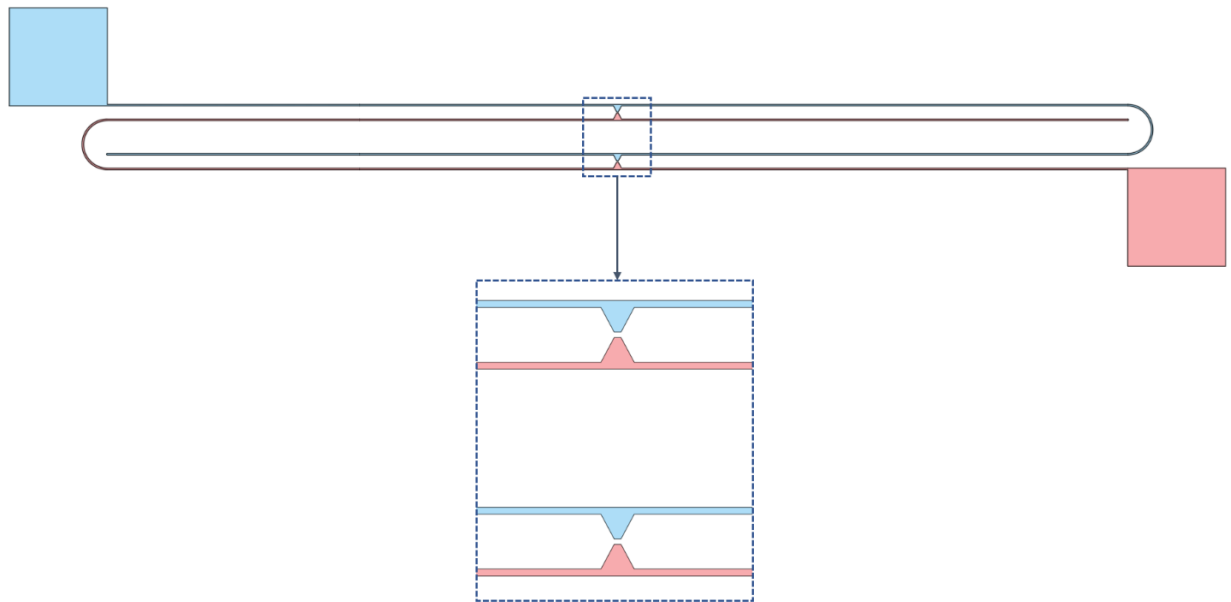


Figure 4.3-1: Two element THz PCA array.

Here, the blue and red shaded areas represent the positive and negative polarities of the DC bias voltage, in no particular order. As seen, the elements share a DC bias voltage and common ground. Three different element spacings were fabricated and measured, being 300  $\mu\text{m}$ , 150  $\mu\text{m}$ , and 75  $\mu\text{m}$ , which correspond to  $\lambda$ ,  $\lambda/2$ , and  $\lambda/4$  at 1 THz. The shared signal and ground allows for the same PCB to be used between the single element PCAs and arrays, however, in a later design,

the DC bias signal was split and a new PCB design as well as peripheral switch board was designed to allow for each element to be turned on and off, which aids in alignment verification. The switch board and dual signal PCBs can be seen below in fig 4.3-1 (a) and (b), respectively.

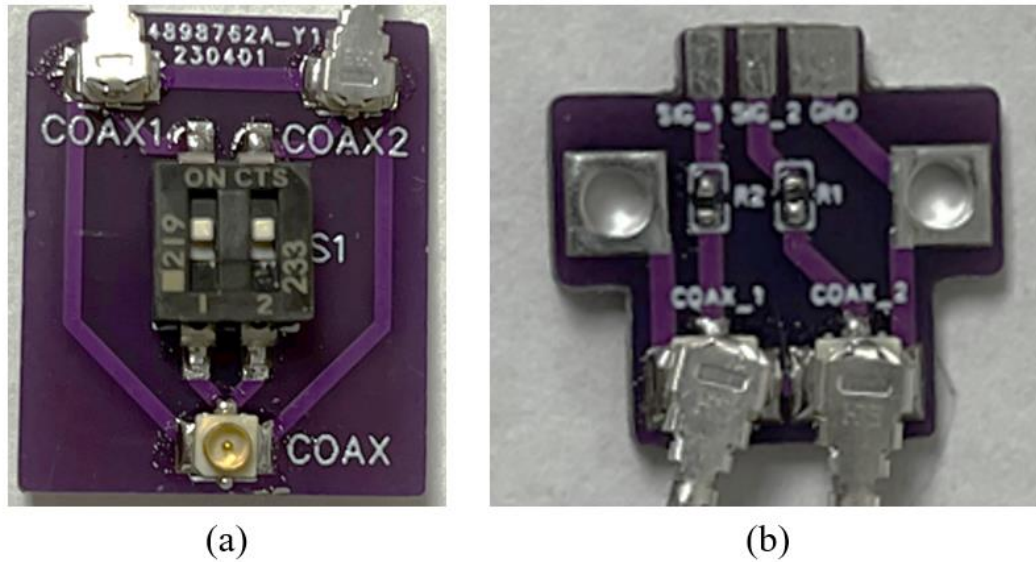


Figure 4.3-2: (a) Switch board PCB. (b) Dual bias array PCB.

The switch board in (a) sits between the TeraAlign system and the array, receiving the input from the TeraAlign system through the U. FL connector labeled COAX, then splitting it into two signal lines, which are then connect to COAX\_1 and COAX\_2 on the device PCB in (b) where the split signal pad delivers the bias voltage to each element. The DIP switch on the switch board lets the user select which element of the array to turn on. This greatly aids in verifying that both elements of the array are being excited, as opposed to just a single element. The CAD for the separate DC bias voltage PCA array can be seen below with signal and ground pads labeled.

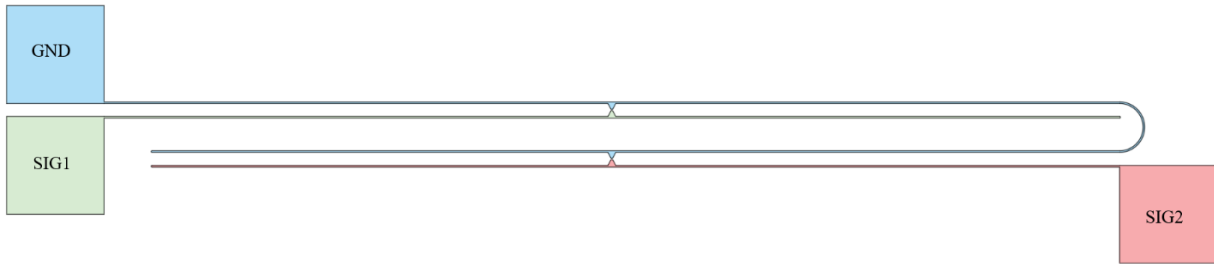


Figure 4.3-3: CAD model of dual bias voltage array

#### 4.4 Beam Splitting Feed Network Design

In the case of the THz PCAs in this work, a novel feeding approach consisting of several mirrors, and two 50:50 beam splitters are used to create two co-parallel beams with identical path lengths. First, a simulation of the setup was designed using 3DOptix online software, the render of the simulated system can be seen below in fig 4.4-1.

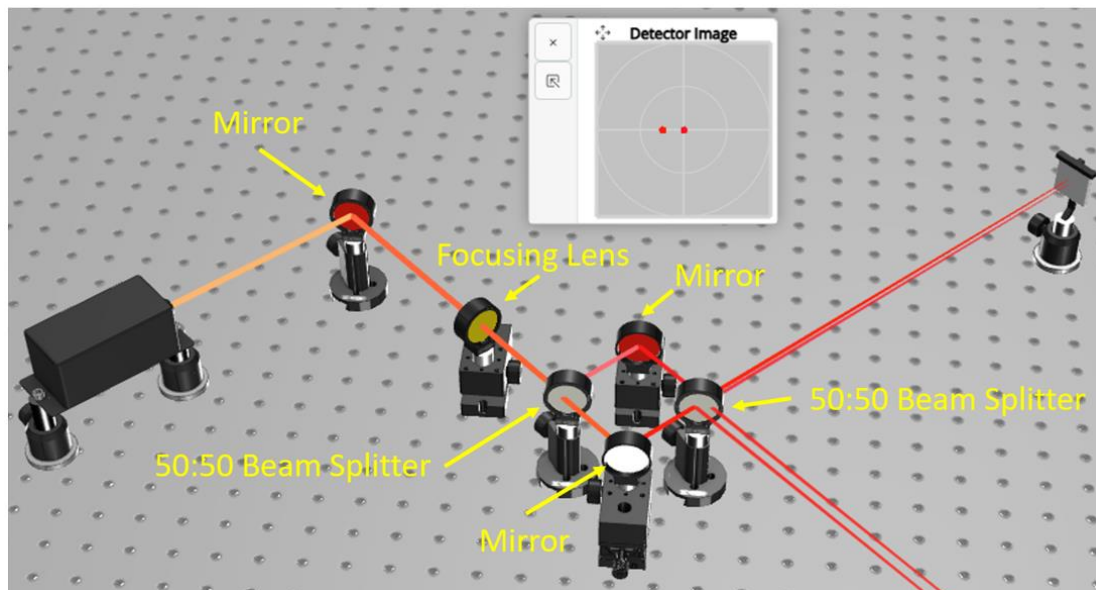


Figure 4.4-1: Simulated beam-splitting array feed setup

In this setup, the beam path begins on the far left with the laser source. From here it is reflected using a mirror into the first beam splitter. The setup above shows a focusing lens in the laser path between the first mirror and beam-splitter; however, this focusing lens is moved to various places within the setup to aid alignment, which will be covered later. After the first splitter splits the beam, two mirrors reflect both beams into a second beam-splitter, which results in two sets of co-parallel beams, one set of which will be used to excite the THz PCA array. The detector screen shows the two focal spots of the laser as they would be seen by the PCA array.

The first important feature of this setup are the translational stages on which the two mirrors between the beam-splitters are mounted. This allows for motion along a single axis, shortening or lengthening the distance between the two mirrors. This is critical to the feed setup as it allows for the path lengths of the two beams to be independently controlled, and in turn, the phase of the excitation. The specific stages used are model MT1B from Thorlabs, which have a  $149.4\text{ }\mu\text{m}$  per turn translation resolution. Further, all mirrors are secured in 2 axis kinematic mounts to allow for individual beam steering for alignment. Below in fig 4.4-2 is an image of the actual setup implemented within the TeraAlign system with examples of the beam paths drawn in.

In this setup, (1) and (2) are the 50:50 beam splitters. (3) and (4) are the two main mirrors mounted on translation stages to control path length and steer each beam. (5) is a variable attenuator to correct for differences in the power between beams, as the 50:50 beam splitters are not extremely precise. (6) is a mirror used to redirect both beams back toward the PCAs. Each of the alignment mirrors, (3) and (4) can be adjusted using the kinematic mount knobs to steer the two beams, which allows for separate alignment of the beams to the array elements. The lens labeled (7) has a focal length of 500mm and is used to focus both beams to smaller focal spots before they pass through the aspherical NIR lens that is part of the TeraAlign system. The reason

for focusing the beams before hitting the NIR lens is that if the NIR lens is used to focus the beams, they their spots will converge to a single point in the focal plane, which will make alignment of the beams to separate elements impossible. Using a secondary lens to focus the beams and reduce their spot sizes before the NIR lens allows for the NIR lens to be utilized slightly outside of its focal place, allowing for separation of the two beams on the surface of the PCA arrays. This concept is shown below in fig 4.4-3.

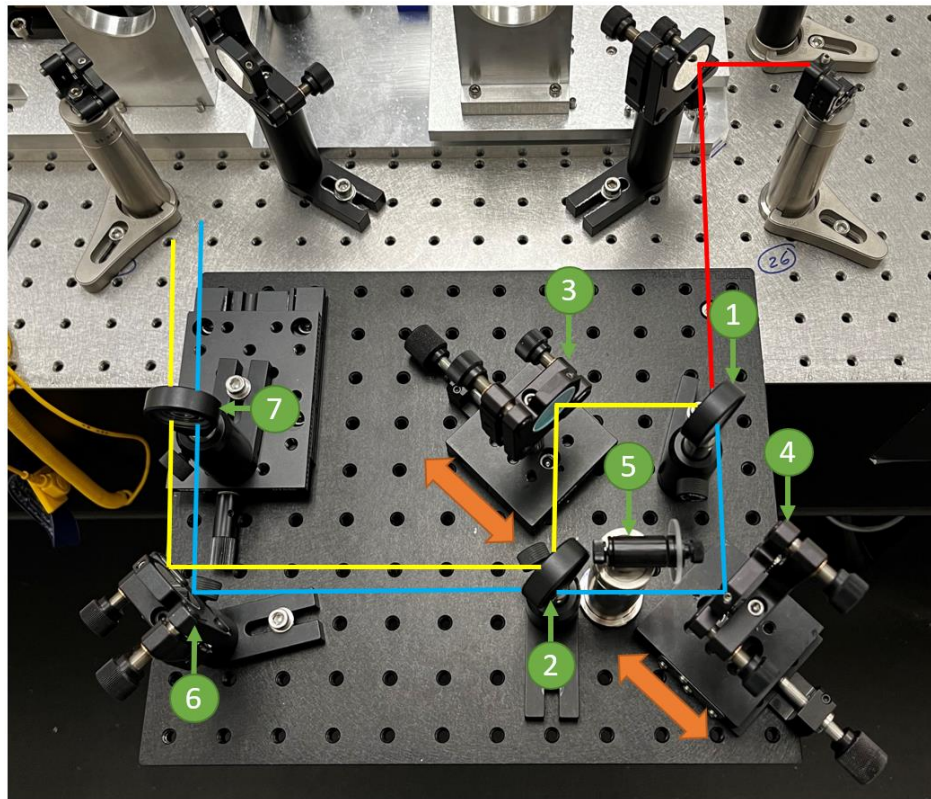


Figure 4.4-2: Beam-splitting THz PCA array feed network.

In this setup, when no pre-focusing lens is used (left), the resulting beams are focused until they converge on plane 1. Moving the PCA along the z-axis until it lies within plane 2 allows for some beam movement in both setups, however, by using the 500mm EFL lens shown on the right,



the spot size at plane 2 can be drastically reduced as compared to no lens, which allows for more concentrated power when aligned to the gap of each array element.

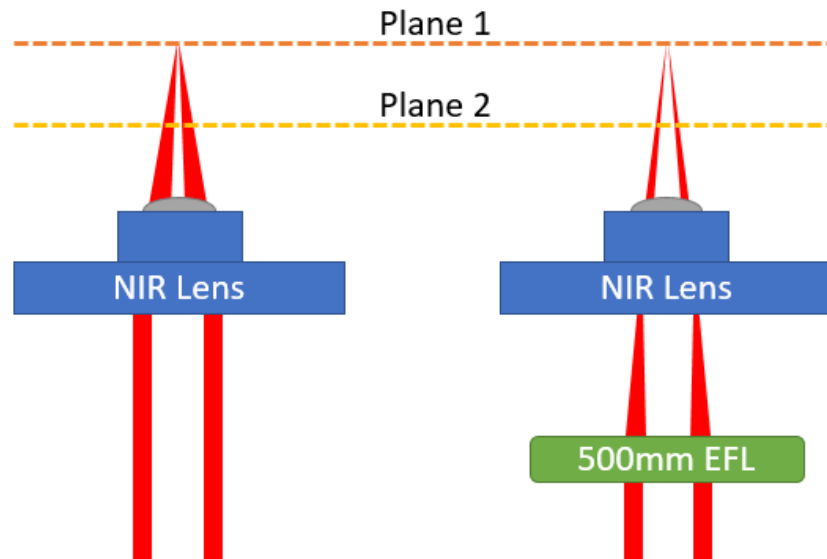


Figure 4.4-3: NIR lens with and without 500mm EFL lens

#### 4.5 THz PCA Array Alignment Procedure

The alignment procedure for the arrays measured in this work shares similar concepts to the procedure used for aligning a single element, however, because the top section of the stacked alignment stages used to align the single element PCAs moves the NIR lens with respect to the PCA, in turn moving both beams at once, it cannot be used for array alignment. Instead, the two mirrors that sit between the beam splitters in the array feed network take the place of the top section of the alignment stages. Further, the brass pinholes become less useful in the case of arrays. This is because during array alignment, it is necessary to at times block one beam and focus on aligning to a single element, and if the pinhole is used to align a single element, that element is now

occupying the center of the system, when ideally the combined THz beam formed by the interaction of both elements should be centered.

To begin array alignment, a reference device should first be placed in the system. This can be any single element THz PCA. With this device in the system, both beams should be aligned to the gap, periodically blocking one beam to ensure that both beams are aligned and contributing equally to the signal. This is done by using the kinematic mirror mounts to align the beam to the gap, in conjunction with the reflection setup using a beam splitter and card as described in section 3.1.2. The 500mm EFL lens should be placed somewhere before the NIR lens in the beam path, this position is not critical, and will need to be adjusted through the alignment procedure, but estimating a distance of 350-450mm before the NIR lens will allow for successful alignment. Further, it is critical to ensure that the pulse obtained from both beams are occurring at the same time. This can easily be achieved by blocking the laser of one beam, recording the time at which the pulse crosses the x-axis, then switching to blocking the other beam and recording where that pulse crosses the x-axis. If the pulses are not aligned, adjusting the translation stages under the alignment mirrors will shift the beam left or right along the x-axis. This movement will slightly misalign the beam from the gap while moving the pulse, so small movements should be made iteratively while readjusting the alignment between each change of the translation stage. Once both beams are creating similar amplitude signals crossing the x-axis at the same time, the THz section of the alignment stages can be used to center the signal in the system using the aid of the 1mm and 0.5mm pinholes. At this point, the reference device can be removed, and the PCA array can be mounted in the system. From here, the beam splitter and card used to view the incident beam should remain in the system at all times. When aligning a single element, the PCA will be in the focal plane of the NIR lens, so the refraction caused by inserting and removing the beam splitter

does not affect the position of the beam enough to misalign the beam, however, in the array setup, the PCA array is out of the focal plane of the NIR lens, meaning the refraction caused by the beam splitter drastically changes the position of the incident location of the beam on the PCA array. This is accounted for by leaving the beam splitter in the path of the beam for the entire alignment process, including when measurements are taken. In this case, the reflection setup is only used to ensure that there is separation between the beam spots, as they will be too focused from the 500mm EFL lens to see the antenna electrodes. Below is an example of what is seen during array alignment on the card.

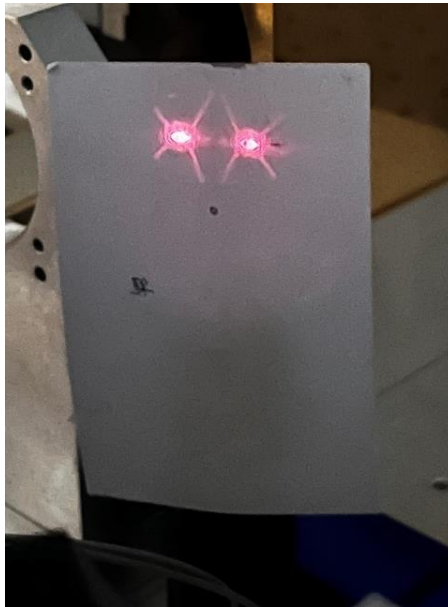


Figure 4.5-1: Card reflection during array alignment.

Two distinct focal spots can be seen on the card, the spacing of which is exaggerated due to passing through multiple lenses before being projected. The spot separation is 150-microns on the surface of the PCA array.

Once the array is mounted in the system, the top stage of the stacked alignment stages can be used to sweep both beam along the surface of the array until a signal can be viewed. Once found, the top stage will no longer be used and the kinematic mirror mounts will do the remainder of the alignment. From this point on the alignment consists of making small adjustments to the beam alignment mirrors to search for the second element, while periodically looking at the reflection card to ensure the beams are not overlapped. This process is not as straight forward as aligning a single element, and required many iterations of searching for the second element. The most important thing to note while aligning is work with a single beam, always blocking the other beam when moving one. If both beams are active it becomes extremely difficult to ensure that the signal seen is coming from the beam that is being aligned. The PCBs designed for adding an on/off function to the antenna elements shown in section 4.3 greatly aid in this process. Only having one active element at a time ensures that the beams are exciting separate elements. Once both elements are excited, no beams should be blocked, and the signal from the array can be viewed and recorded. This alignment procedure is very much trial and error based, and future work will be required to refine and improve the feed network and alignment procedure. In the early stages of array fabrication and measurements, the dual bias PCBs were not used, and there was doubt as to whether the beams were correctly aligned, which will be covered in the following section.

#### **4.6 THz PCA Array Measurements**

As previously mentioned, three dimensions of arrays have been fabricated for this work. The sole change through each design is the gap-to-gap spacing of the two elements. In all cases, 1 THz is used as the base frequency, with spacings of  $\lambda$ ,  $\lambda/2$ , and  $\lambda/4$  have been used, which correspond to distances of 300, 150 and 75-microns, respectively. The initial results for all three dimensions were done using the shared bias and ground design. While able to produce THz signals,

there is some doubt as to whether the alignments of the beams are incident on separate elements, or if there is overlap between excitations. These concerns led to the design and fabrication of the split bias design, and new device and switch board PCBs. Below in fig 4.6-1 are the initial results for the three shared bias and ground THz PCAs, showing the individual element signals, isolated simply by blocking one beam at a time, and taking a measuring, as well as the array signal when both beams are incident on the array. I should be noted that the amplitude of any array shown here will be lower than the single elements measurements shown in chapter 3 due to the 6-fold decrease in power at the gap from the array feed network.

To begin, the top row of plots, which show measurements of the 75-micron array, show an extremely close relationship between the full array signal, and that of element 2. At first this led to the conclusion that one element of the array was dominating the overall performance, due to multiple alignments resulting in the same trend. This also created concern that the alignment to element 2 was much better than element 1, attempts to increase the signal of element 1 were unsuccessful by moving the laser. However, if the THz pulse is adjusted using the bottom alignment stage, by attempting to optimize the element 1 signal through a pinhole, it was found that while element 1 was increased, it greatly reduced the amplitude of element 2, and the array signal now tracked element 1. This led to the conclusion that pinhole alignments to single element signals was not a useful alignment technique, leading to all measurements being done with no pinhole. Further, attempting to improve the pulse shape of one element always resulted in the other element suffering.

In the case of the 150-micron array, a similar scenario is observed. Again, element 1 has significantly lower pulse amplitude and spectral magnitude, and the array signal closely follows that of the larger element, in this case element 2. Compared to the 75-micron array, the difference

in signal amplitude between the two elements is smaller. This leads to a slight increase in array strength compared to the individual element, where at the peak of element 2, a maximum of  $\sim 1.5$  is reached, while the array reaches  $\sim 2.1$ .

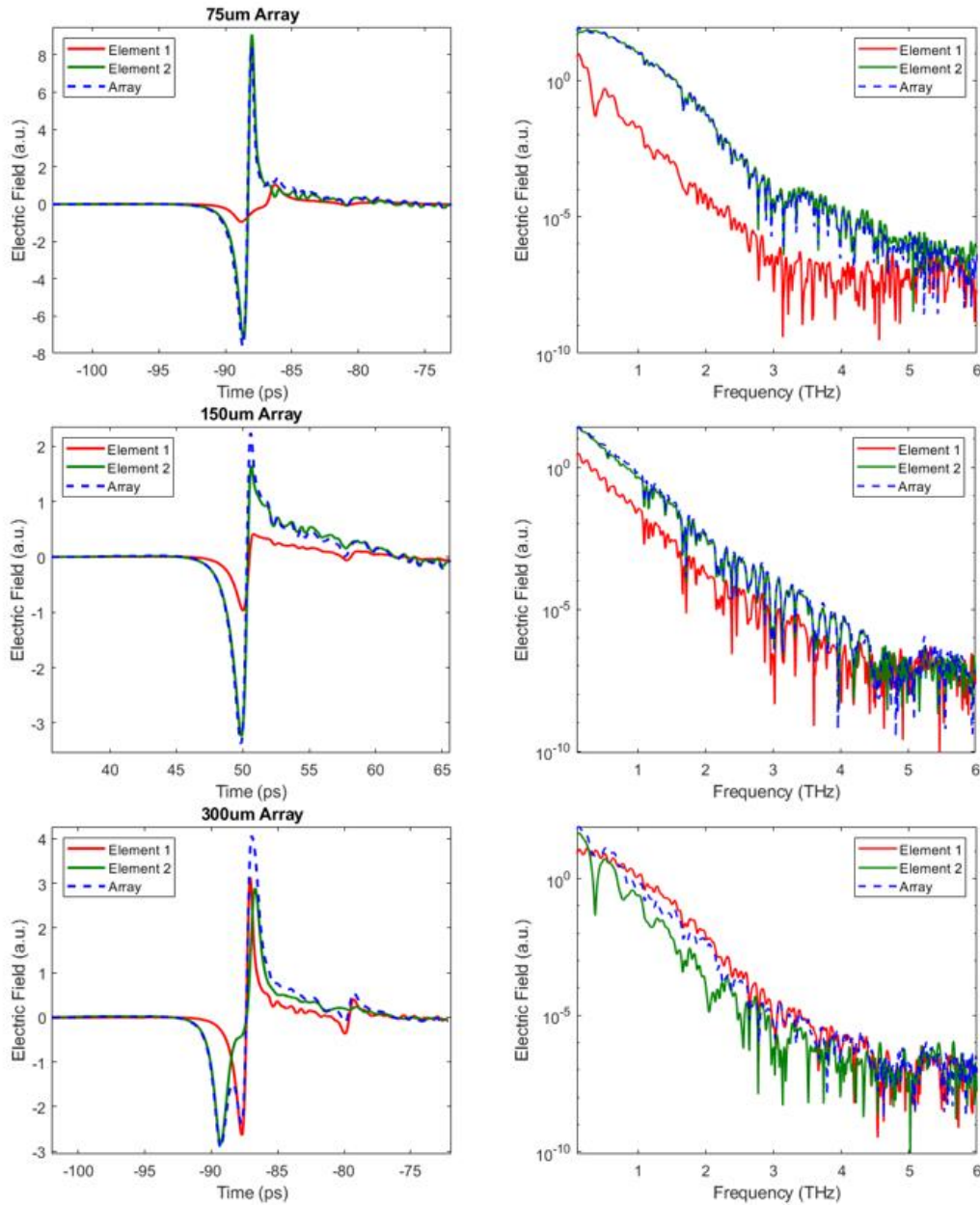


Figure 4.6-1: Time domain and Spectrum of THz PCA Arrays.

Finally, alignments of the 300-micron array were able to balance the signal between the two elements in a way that creates an obvious combination of the two signals for the array. This is most visible at the negative peaks of the pulse, where the array signal tracks both of the pulses, creating a double negative peak. Ideally, the positive and negative peaks of the individual elements would be aligned in time. In this case, the positive peaks are aligned, and attempts to alter the beam path distance to align the negative peaks simply results in divergence of the positive peaks. For a single element, the shape of the THz pulse can be manipulated by adjusting the THz alignment stage, but as mentioned previously, attempts to adjust this stage to favor one element will drastically reduce the other.

The conclusion drawn from these measurements is that validation of by element excitation is extremely difficult with a shared bias voltage. Even when blocking beams to attempt to isolate individual elements, it cannot be concluded with certainty that this really shows the signal from each element, as there could be overlap in the exposure. The design of an array with separate bias voltages allow the user to block individual beams and turn off one element at a time, which allows for carefully alignment to a single elements without any influence by the other.

First validation of the new PCB and switchboard were required to ensure that the on/off function and splitting of the bias voltage worked as intended, the results of which are shown below in fig 4.6-2. Here, both coax boards from the switchboard are measured while on, and while off for a reference device. Note that even when off, there is a very small leakage in both switches, which is why a spectrum and pulse are still seen when off. However, this pulse is over 200 times smaller than the pulse with the switch on, which provides enough reduction to make alignment validation possible. The superimposed figures indicated by the blue arrow are the zoomed signal of the switch in the off position.

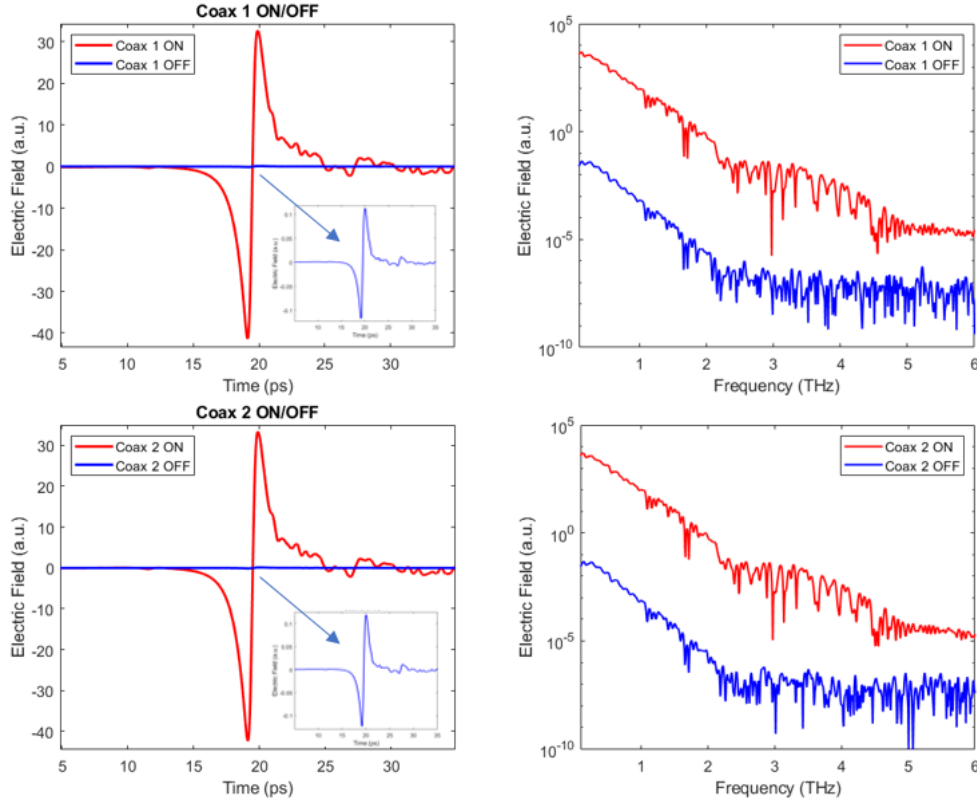


Figure 4.6-2: Split bias switch function validation measurements.

Once validated, the new PCA array designs were fabricated and connected to the dual bias PCB for measurements. Using the on/off function, much better alignments, with confidence that both elements are being excited by separate beams are obtained. This is done using the same alignment procedure as previously used, however with the new PCBs, first one beam is blocked, then one element is turned off. After this, the remaining beam can be aligned to the active element, with no certainty that the other element is contributing no significant signal. After the signal is aligned well, it can be turned off, the other element turned on, and the beam that is being blocked can be switched. The same procedure is repeated with the remaining element, resulting in a well



aligned array. After both elements have been aligned, the full array can be activated, and no beams are blocked. The results for this procedure can be seen below in fig 4.6-3.

In these plots, each element is contributing nearly equally to the overall array signal, and has been experimentally validated to ensure that both elements are being individually excited with no overlap of excitation between beams. Starting with the top of fig 6.6-3, the 75 micron spaced dual bias array is shown. In this case, there is a slight misalignment of the peaks, both positive and negative due to differences in the pulse width between each element. Because the array signal is a combination of both element pulses, this results in a wider array signal than either of the individual elements. This is true for all three cases shown.

In the case of the 150-micron spaced array, similar results can be seen, where both element 1 and element 2 have similar pulse amplitudes, resulting in an array signal with a higher amplitude than either element. An important note is that the spectrum of the 150-micron array is significantly wider than the 75- or 300-micron spaced arrays. This is most likely due to the substrate used during the fabrication process. The 150-micron array was fabricated first, on a different section of wafer than the 75- or 300-micron arrays, which were fabricated simultaneously on the same wafer piece. This results in the 75- and 300-micron arrays having similar performances due to the substrate characteristics likely being more similar to each other than the substrate of the 150-micron array.

Finally, the 300-micron array results follow suit with the other two arrays, with equally contributing elements resulting in a larger, but wider overall array signal. The spectrum and amplitude of all three dual bias arrays is significantly lower than any single element antennas measured in this work due to the lack of laser power that can be provided to each element in the beam splitting feed network used in all cases shown.

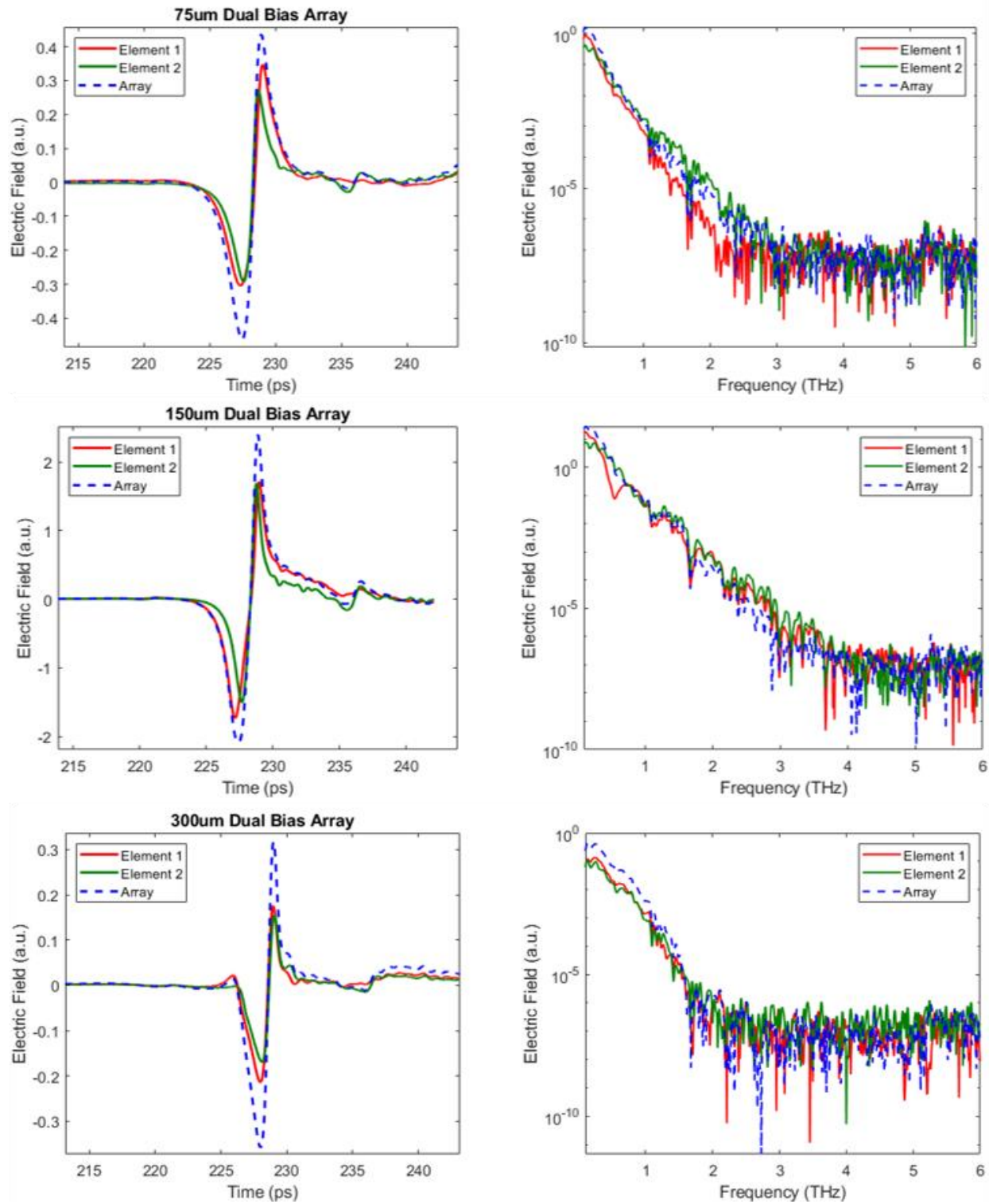


Figure 4.6-3: Time domain and Spectrum of Dual Bias THz PCA Arrays.

## 4.7 THz PCA Array Conclusions

In conclusion. Many novel approaches have been seen throughout the literature for feeding THz PCA arrays, including flood exposure, special light modulation, sequential excitation, and the use of micro lens arrays. The approach taken in this work designed a beam splitting feed network that allows for individual control of the position and path length of two separate parallel beams.

The alignment procedure used for this setup is much more challenging than the single element antennas, requiring some trial and error along with many iterations of beam movements. The pinholes used for single element measurements become less useful in an array situation due to the spacing of the elements from each other. Further, validation of excitation to each element by a single beam was doubted in the initial measurements, leading to the development of a dual bias array, and implementation of a peripheral switchboard to allow array elements to be turned on and off.

The large difference in signal amplitude between the 150 micron array, and the 75 and 300 micron arrays could be due to multiple reasons. First, as stated previously, both the 75 and 300 micron arrays were fabricated on the same piece of wafer, while the 150 micron array had been fabricated previously on a different section of the same wafer. This leaves the possibility that the carrier dynamics are different in the separate pieces, leading to gaps in performance under the same bias voltage and laser power. The similar pulse amplitudes of the 75 and 300 micron arrays point toward this conclusion. Further, alignment is always a factor in the overall signal shape, amplitude, and bandwidth. While multiple alignments have been done for each device, there is the possibility that better alignments would be able to increase the pulse amplitude.

Overall, the measurements of the alignment verified dual bias arrays show that the overall signal is in fact a combination of both elements pulses, which increases amplitude resulting in a

wider signal; however, future work must be done to study the effect of more than two elements using the described beam splitting feed network. Additional two element array measurements can be seen in Appendix C.

## Chapter 5: Conclusions and Future Work

In conclusion, this thesis presents the fabrication and measurement of several electrode shapes of LT-GaAs THz PCAs. The fabrication process for all LT-GaAs reference antennas utilizes electron beam lithography to pattern electrode designs into PMMA coated LT-GaAs. This process is followed by resistive thermal evaporation of 5/50nm of Cr/Au followed by acetone lift-off to complete the on chip portion of the devices. Each antennas is then adhered to a chip carrier with clear nail polish, followed by electrically connecting it to the carrier through ultrasonic wire bonding using 1 mil aluminum bonding thread. In this work, 4 electrode designs were fabricated: bowtie, fractal, slotted, and circular. Early fabrication attempts used etching to achieve the slotted and fractal electrode features that were overexposed during the EBL step, but it was found that proximity effect correction software was able to effectively eliminate the overexposure, and successfully pattern all features with high dimensional accuracy. Two element arrays were also fabricated and measured with three different spacings of electrodes: 300-micron, 150-micron, and 75-micron.

All devices were measured using an open bench time-domain spectroscopy system called the TeraAlign system developed by TeraView. The optical pump used in measurements is a 780 nm femtosecond pulsed laser with ~86 mW of power. The pump power at the emitter and detector is 6 mW and 5 mW respectively. The TeraAlign system is comprised two stacked alignment stages, one for emitter, and one for detector, that allows for precise alignment of the incoming laser beam to the gap of the antenna, as well as alignment of the emitted THz pulse from emitter to detector. All measurements taken using the TeraAlign system are averaged over 1800 samples to reduce the effect of system noise. Further, for single element THz PCAs, two brass pinholes with 1mm and 0.5mm diameter are used as high-pass filters with cutoff frequencies of 0.175 THz and 0.35 THz

respectively. This allows or low frequency components of the signals to be removed so that the THz frequencies can be better studied. Beyond this, the pinholes aid in ensuring that the THz signal is centered in the system, as well as serve as an alignment quality control tool. The alignment of each device, both laser and THz pulse is a critical step in ensuring reliable data collection.

The single element device measurements established trends related to the effect DC bias voltage and incident laser power have on the resulting signal. It was found that for DC bias voltage, the THz pulse increased mostly linearly through the entire test range. For incident laser power, the pulse increased linearly after ~3.5 mW of power. In both cases, the variable not being studied was kept constant at its standard testing value, which for all devices is 6mW of laser power, and 63V DC bias. Next, wire grid polarizers and a  $\lambda/2$  quartz crystal acting as a rotator were used to measure the horizontal and linear polarization of all four electrode shapes in the single element devices. It was found that there was ~2 orders of magnitude lower signal in the vertical polarization when compared to horizontal. This verified the linear polarization of all devices. It is important to note that the detector used in all measurements is also highly linearly polarized in the horizontal direction. Finally, a comparison of the signal strength between all 4 electrode shapes, as well as a LT-GaAs based commercial emitter designed and fabricated by TeraView was done. These results showed that the bowtie emitter out performed all other electrode shapes for emitters fabricated as part of this work. Further, when no pinhole is used, the pulses of all 4 electrode shapes have nearly double the peak-to-peak amplitude of commercial emitter. However, when using the pinholes, which cut out the low frequencies, the commercial emitter begins to surpass all other emitters. This leads to the conclusion that some low frequency components are majorly contributing to the THz pulse in the bowtie, slotted, circular, and fractal emitters.

As previously mentioned, 3 different electrode spacings of 2-element arrays were fabricated and measured as part of this thesis. Each of the 3 arrays shared a common DC bias signal and ground. A beam-splitting feed network was designed and implemented into the TeraAlign system to allow for two co parallel beams to be independently aligned to the gaps of the two elements. The alignment procedure is much more difficult than in single element measurements, which initially led to doubts as to if both elements in the arrays were being excited. This resulted in a new array design, in which the two elements do not share the same bias voltage. A new antenna PCB as well as a peripheral switch board were designed and implemented in order to allow each element to be turned on and off at will. The on/off function of each element allowed for verification of alignment with much higher confidence levels than the previous design. Measurements of the separate DC bias array clearly show that the resulting THz pulse is a combination of the individual signals from each element, resulting in a higher amplitude, but slightly lower spectrum amplitude due to widening of the combined signal. Further, due to limited laser power, the incident power at each array elements is  $\sim 1\text{mW}$ , which greatly affects the overall pulse amplitude.

The future work of this project has many routes. First, there are many more electrode shapes that could be fabricated and measured in order to increase the bandwidth, as well as increase the signal amplitude of the PCAs. While the bowtie performed the best out of the 4 shapes in this work, each shape has a unique signal shape and spectrum. Next, increasing the number of elements in the PCA array is the next step in studying the properties of these devices. This presents the challenge of feeding. Many novel solutions to array feeding are presented in the literature, but finding a scalable feed network design as the number of elements in the arrays increase will require significantly more time and effort.

## Bibliography

- [1] A. Shafie, N. Yang, C. Han, J. M. Jornet, M. Juntti, and T. Kurner, "Terahertz Communications for 6G and Beyond Wireless Networks: Challenges, Key Advancements, and Opportunities," *IEEE Network*, pp. 1–8, 2022, doi: 10.1109/MNET.118.2200057.
- [2] M. Z. Chowdhury, Md. Shahjalal, S. Ahmed, and Y. M. Jang, "6G Wireless Communication Systems: Applications, Requirements, Technologies, Challenges, and Research Directions," *IEEE Open Journal of the Communications Society*, vol. 1, pp. 957–975, 2020, doi: 10.1109/OJCOMS.2020.3010270.
- [3] B. Ji *et al.*, "Several Key Technologies for 6G: Challenges and Opportunities," *IEEE Communications Standards Magazine*, vol. 5, no. 2, pp. 44–51, Jun. 2021, doi: 10.1109/MCOMSTD.001.2000038.
- [4] M. El-Shenawee, N. Vohra, T. Bowman, and K. Bailey, "Cancer detection in excised breast tumors using terahertz imaging and spectroscopy," *Biomedical Spectroscopy and Imaging*, vol. 8, no. 1–2, pp. 1–9, Jan. 2019, doi: 10.3233/BSI-190187.
- [5] T. Chavez, N. Vohra, J. Wu, K. Bailey, and M. El-Shenawee, "Breast Cancer Detection With Low-Dimensional Ordered Orthogonal Projection in Terahertz Imaging," *IEEE Transactions on Terahertz Science and Technology*, vol. 10, no. 2, pp. 176–189, Mar. 2020, doi: 10.1109/TTHZ.2019.2962116.
- [6] M. Yamashita *et al.*, "Laser THz emission microscope as a novel tool for LSI failure analysis," *Microelectronics Reliability*, vol. 49, no. 9, pp. 1116–1126, Sep. 2009, doi: 10.1016/j.microrel.2009.07.047.
- [7] J. True, C. Xi, N. Jessurun, K. Ahi, and N. Asadizanjani, "Review of THz-based semiconductor assurance," *OE*, vol. 60, no. 6, p. 060901, Jun. 2021, doi: 10.1117/1.OE.60.6.060901.
- [8] J. F. Federici *et al.*, "THz imaging and sensing for security applications—explosives, weapons and drugs," *Semicond. Sci. Technol.*, vol. 20, no. 7, p. S266, Jun. 2005, doi: 10.1088/0268-1242/20/7/018.
- [9] H.-B. Liu, H. Zhong, N. Karpowicz, Y. Chen, and X.-C. Zhang, "Terahertz Spectroscopy and Imaging for Defense and Security Applications," *Proceedings of the IEEE*, vol. 95, no. 8, pp. 1514–1527, Aug. 2007, doi: 10.1109/JPROC.2007.898903.
- [10] Y. He, Y. Chen, L. Zhang, S.-W. Wong, and Z. N. Chen, "An overview of terahertz antennas," *China Communications*, vol. 17, no. 7, pp. 124–165, Jul. 2020, doi: 10.23919/J.CC.2020.07.011.
- [11] N. M. Burford and M. O. El-Shenawee, "Review of terahertz photoconductive antenna technology," *OE*, vol. 56, no. 1, p. 010901, Jan. 2017, doi: 10.1117/1.OE.56.1.010901.



- [12] M. C. Beard, G. M. Turner, and C. A. Schmuttenmaer, "Subpicosecond carrier dynamics in low-temperature grown GaAs as measured by time-resolved terahertz spectroscopy," *Journal of Applied Physics*, vol. 90, no. 12, pp. 5915–5923, Dec. 2001, doi: 10.1063/1.1416140.
- [13] S. Gupta *et al.*, "Subpicosecond carrier lifetime in GaAs grown by molecular beam epitaxy at low temperatures," *Appl. Phys. Lett.*, vol. 59, no. 25, pp. 3276–3278, Dec. 1991, doi: 10.1063/1.105729.
- [14] R. B. Kohlhaas *et al.*, "637  $\mu$ W emitted terahertz power from photoconductive antennas based on rhodium doped InGaAs," *Applied Physics Letters*, vol. 117, no. 13, p. 131105, Sep. 2020, doi: 10.1063/5.0020766.
- [15] K. Kuznetsov *et al.*, "Improved InGaAs and InGaAs/InAlAs Photoconductive Antennas Based on (111)-Oriented Substrates," *Electronics*, vol. 9, no. 3, Art. no. 3, Mar. 2020, doi: 10.3390/electronics9030495.
- [16] D. V. Lavrukhin *et al.*, "Strain-Induced InGaAs-Based Photoconductive Terahertz Antenna Detector," *IEEE Transactions on Terahertz Science and Technology*, vol. 11, no. 4, pp. 417–424, Jul. 2021, doi: 10.1109/TTHZ.2021.3079977.
- [17] J. S. Batista, H. O. H. Churchill, and M. El-Shenawee, "Black phosphorus photoconductive terahertz antenna: 3D modeling and experimental reference comparison," *Journal of the Optical Society of America B*, vol. 38, no. 4, Mar. 2021, doi: 10.1364/JOSAB.419996.
- [18] Z. Uttley, J. Santos Batista, B. Pirzada, and M. El-Shenawee, "Experimental and Computational Analysis of Broadband THz Photoconductive Antennas," *International Journal of Antennas and Propagation*, vol. 2023, p. e6682627, Feb. 2023, doi: 10.1155/2023/6682627.
- [19] F. Ganikhanov, G. Lin, W. Chen, C. -S. Chang, and C. Pan, "Subpicosecond carrier lifetimes in arsenic-ion-implanted GaAs," *Appl. Phys. Lett.*, vol. 67, no. 23, pp. 3465–3467, Dec. 1995, doi: 10.1063/1.115248.
- [20] C. Tannoury, M. Billet, C. Coinon, J.-F. Lampin, and E. Peytavit, "Low-temperature-grown gallium arsenide photoconductors with subpicosecond carrier lifetime and photoresponse reaching 25 mA/W under 1550 nm CW excitation," *Electronics Letters*, vol. 56, no. 17, pp. 897–899, 2020, doi: 10.1049/el.2020.1116.
- [21] X. Liu *et al.*, "Mechanism responsible for the semi-insulating properties of low-temperature-grown GaAs," *Appl. Phys. Lett.*, vol. 65, no. 23, pp. 3002–3004, Dec. 1994, doi: 10.1063/1.112490.
- [22] E. S. Harmon, M. R. Melloch, J. M. Woodall, D. D. Nolte, N. Otsuka, and C. L. Chang, "Carrier lifetime versus anneal in low temperature growth GaAs," *Appl. Phys. Lett.*, vol. 63, no. 16, pp. 2248–2250, Oct. 1993, doi: 10.1063/1.110542.
- [23] J. Miao, L. Zhang, and C. Wang, "Black phosphorus electronic and optoelectronic devices," *2D Mater.*, vol. 6, no. 3, p. 032003, May 2019, doi: 10.1088/2053-1583/ab1ebd.

- [24] F. H. L. Koppens, T. Mueller, P. Avouris, A. C. Ferrari, M. S. Vitiello, and M. Polini, “Photodetectors based on graphene, other two-dimensional materials and hybrid systems,” *Nature Nanotech*, vol. 9, no. 10, Art. no. 10, Oct. 2014, doi: 10.1038/nnano.2014.215.
- [25] M. H. Doha and this link will open in a new window Link to external site, “Two-Dimensional Black Phosphorus for Terahertz Emission and Near-Field Radiative Heat Transfer,” Ph.D., University of Arkansas, United States -- Arkansas, 2021. Accessed: Apr. 15, 2023. [Online].
- [26] P. C. Debnath, K. Park, and Y.-W. Song, “Recent Advances in Black-Phosphorus-Based Photonics and Optoelectronics Devices,” *Small Methods*, vol. 2, no. 4, p. 1700315, 2018, doi: 10.1002/smtd.201700315.
- [27] G. Long *et al.*, “Achieving Ultrahigh Carrier Mobility in Two-Dimensional Hole Gas of Black Phosphorus,” *Nano Lett.*, vol. 16, no. 12, pp. 7768–7773, Dec. 2016, doi: 10.1021/acs.nanolett.6b03951.
- [28] K. Wang *et al.*, “Ultrafast Nonlinear Excitation Dynamics of Black Phosphorus Nanosheets from Visible to Mid-Infrared,” *ACS Nano*, vol. 10, no. 7, pp. 6923–6932, Jul. 2016, doi: 10.1021/acsnano.6b02770.
- [29] F. Xia, H. Wang, and Y. Jia, “Rediscovering black phosphorus as an anisotropic layered material for optoelectronics and electronics,” *Nat Commun*, vol. 5, no. 1, Art. no. 1, Jul. 2014, doi: 10.1038/ncomms5458.
- [30] R. Schuster, J. Trinckauf, C. Habenicht, M. Knupfer, and B. Büchner, “Anisotropic Particle-Hole Excitations in Black Phosphorus,” *Phys. Rev. Lett.*, vol. 115, no. 2, p. 026404, Jul. 2015, doi: 10.1103/PhysRevLett.115.026404.
- [31] M. H. Doha *et al.*, “Integration of multi-layer black phosphorus into photoconductive antennas for THz emission,” *Journal of Applied Physics*, vol. 128, no. 6, p. 063104, Aug. 2020, doi: 10.1063/5.0016370.
- [32] Q. Feng, F. Yan, W. Luo, and K. Wang, “Charge trap memory based on few-layer black phosphorus,” *Nanoscale*, vol. 8, no. 5, pp. 2686–2692, Jan. 2016, doi: 10.1039/C5NR08065G.
- [33] R. J. Suess *et al.*, “Mid-infrared time-resolved photoconduction in black phosphorus,” *2D Mater.*, vol. 3, no. 4, p. 041006, Oct. 2016, doi: 10.1088/2053-1583/3/4/041006.
- [34] R. J. Suess, M. M. Jadidi, T. E. Murphy, and M. Mittendorff, “Carrier dynamics and transient photobleaching in thin layers of black phosphorus,” *Appl. Phys. Lett.*, vol. 107, no. 8, p. 081103, Aug. 2015, doi: 10.1063/1.4929403.
- [35] C. W. Berry, M. R. Hashemi, and M. Jarrahi, “Generation of high power pulsed terahertz radiation using a plasmonic photoconductive emitter array with logarithmic spiral antennas,” *Appl. Phys. Lett.*, vol. 104, no. 8, p. 081122, Feb. 2014, doi: 10.1063/1.4866807.

- [36] V. Rathinasamy, R. R. Thipparaju, N. F. B. Edwin, and S. Mondal, "Interdigitated photoconductive terahertz antenna for future wireless communications," *Microwave and Optical Technology Letters*, vol. 64, no. 12, pp. 2189–2196, 2022, doi: 10.1002/mop.33034.
- [37] N. M. Burford, M. J. Evans, and M. O. El-Shenawee, "Plasmonic Nanodisk Thin-Film Terahertz Photoconductive Antenna," *IEEE Transactions on Terahertz Science and Technology*, vol. 8, no. 2, pp. 237–247, Mar. 2018, doi: 10.1109/TTHZ.2017.2782484.
- [38] M. Bashirpour, M. Forouzmehr, S. E. Hosseinienejad, M. Kolahdouz, and M. Neshat, "Improvement of Terahertz Photoconductive Antenna using Optical Antenna Array of ZnO Nanorods," *Sci Rep*, vol. 9, no. 1, Art. no. 1, Feb. 2019, doi: 10.1038/s41598-019-38820-3.
- [39] M. D. Levenson, N. S. Viswanathan, and R. A. Simpson, "Improving resolution in photolithography with a phase-shifting mask," *IEEE Transactions on Electron Devices*, vol. 29, no. 12, pp. 1828–1836, Dec. 1982, doi: 10.1109/T-ED.1982.21037.
- [40] R. J. Blaikie, D. O. S. Melville, and M. M. Alkaisi, "Super-resolution near-field lithography using planar silver lenses: A review of recent developments," *Microelectronic Engineering*, vol. 83, no. 4, pp. 723–729, Apr. 2006, doi: 10.1016/j.mee.2006.01.056.
- [41] D. Melville and R. Blaikie, "Super-resolution imaging through a planar silver layer," *Opt Express*, vol. 13, no. 6, pp. 2127–2134, Mar. 2005, doi: 10.1364/opex.13.002127.
- [42] J. A. Rogers, K. E. Paul, R. J. Jackman, and G. M. Whitesides, "Generating ~90 nanometer features using near-field contact-mode photolithography with an elastomeric phase mask," *Journal of Vacuum Science & Technology B: Microelectronics and Nanometer Structures Processing, Measurement, and Phenomena*, vol. 16, no. 1, pp. 59–68, Jan. 1998, doi: 10.1116/1.589836.
- [43] Y. Chen, "Nanofabrication by electron beam lithography and its applications: A review," *Microelectronic Engineering*, vol. 135, pp. 57–72, Mar. 2015, doi: 10.1016/j.mee.2015.02.042.
- [44] W. (Walter) Hu, K. Sarveswaran, M. Lieberman, and G. H. Bernstein, "Sub-10 nm electron beam lithography using cold development of poly(methylmethacrylate)," *J. Vac. Sci. Technol. B*, vol. 22, no. 4, p. 1711, 2004, doi: 10.1116/1.1763897.
- [45] J. Randall, J. Owen, J. Lake, and E. Fuchs, "Next generation of extreme-resolution electron beam lithography," *Journal of Vacuum Science & Technology B*, vol. 37, p. 061605, Nov. 2019, doi: 10.1116/1.5119392.
- [46] J. Santos Batista, "Computational Modeling of Black Phosphorus Terahertz Photoconductive Antennas using COMSOL Multiphysics with Experimental Comparison against a Commercial LT-GaAs Emitter," University of Arkansas, 2021. [Online]. Available: <https://scholarworks.uark.edu/etd/4153>

- [47] E. Seo, B. K. Choi, and O. Kim, "Determination of proximity effect parameters and the shape bias parameter in electron beam lithography," *Microelectronic Engineering*, vol. 53, no. 1, pp. 305–308, Jun. 2000, doi: 10.1016/S0167-9317(00)00320-8.
- [48] M. Eissa, T. Mitarai, T. Amemiya, Y. Miyamoto, and N. Nishiyama, "Fabrication of Si photonic waveguides by electron beam lithography using improved proximity effect correction," *Jpn. J. Appl. Phys.*, vol. 59, no. 12, p. 126502, Nov. 2020, doi: 10.35848/1347-4065/abc78d.
- [49] W. Yao *et al.*, "Efficient Proximity Effect Correction Using Fast Multipole Method With Unequally Spaced Grid for Electron Beam Lithography," *IEEE Trans. Comput.-Aided Des. Integr. Circuits Syst.*, vol. 42, no. 1, pp. 218–228, Jan. 2023, doi: 10.1109/TCAD.2022.3171441.
- [50] C.-L. Lee, S.-W. Chien, and K.-Y. Tsai, "Model-based proximity effect correction for helium ion beam lithography," in *Novel Patterning Technologies 2018*, SPIE, Mar. 2018, pp. 269–280. doi: 10.1117/12.2297691.
- [51] C.-H. Liu, P. C. W. Ng, Y.-T. Shen, S.-W. Chien, and K.-Y. Tsai, "Impacts of point spread function accuracy on patterning prediction and proximity effect correction in low-voltage electron-beam–direct-write lithography," *Journal of Vacuum Science & Technology B*, vol. 31, no. 2, p. 021605, Mar. 2013, doi: 10.1116/1.4790655.
- [52] MircoChem, "PMMA Data Sheet," 2001. [https://kayakuam.com/wp-content/uploads/2019/09/PMMA\\_Data\\_Sheet.pdf](https://kayakuam.com/wp-content/uploads/2019/09/PMMA_Data_Sheet.pdf) (accessed Apr. 10, 2023).
- [53] A. Yariv and P. Yeh, *Optical Waves in Crystals*. in Propagation and Control of Laser Radiation. Wiley. Accessed: Apr. 14, 2023. [Online]. Available: [https://einstein.nju.edu.cn/upload/kindeditor/file/20210703/20210703141032\\_9661.pdf](https://einstein.nju.edu.cn/upload/kindeditor/file/20210703/20210703141032_9661.pdf)
- [54] Z. C. Chen, M. H. Hong, and T. C. Chong, "Fabrication and Characterization of Broadband Terahertz Wire-Grid Polarizer," *Journal of Nonlinear Optical Physics and Materials*, vol. 19, pp. 827–833, Jan. 2010, doi: 10.1142/S0218863510005765.
- [55] R. M. Hendrix, J. R. Middendorf, J. S. Cetnar, J. A. Deibel, and E. R. Brown, "Broadband characterization of THz frequency high fill-factor substrate-based wire-grid polarizers with high extinction ratios," in *2014 39th International Conference on Infrared, Millimeter, and Terahertz waves (IRMMW-THz)*, Sep. 2014, pp. 1–2. doi: 10.1109/IRMMW-THz.2014.6956414.
- [56] T. Dong-Bin, Z. Huai-Wu, L. Wei-En, W. Qi-Ye, S. Yuan-Qiang, and W. Zhi-Guo, "Double Wire-Grid Terahertz Polarizer on Low-Loss Polymer Substrates," *Chinese Phys. Lett.*, vol. 27, no. 10, p. 104210, Oct. 2010, doi: 10.1088/0256-307X/27/10/104210.
- [57] A. H. Naqvi and S. Lim, "Review of Recent Phased Arrays for Millimeter-Wave Wireless Communication," *Sensors*, vol. 18, no. 10, Art. no. 10, Oct. 2018, doi: 10.3390/s18103194.

- [58] J. Helander, K. Zhao, Z. Ying, and D. Sjöberg, "Performance Analysis of Millimeter-Wave Phased Array Antennas in Cellular Handsets," *IEEE Antennas and Wireless Propagation Letters*, vol. 15, pp. 504–507, 2016, doi: 10.1109/LAWP.2015.2455040.
- [59] W. Hong, K.-H. Baek, and S. Ko, "Millimeter-Wave 5G Antennas for Smartphones: Overview and Experimental Demonstration," *IEEE Transactions on Antennas and Propagation*, vol. 65, no. 12, pp. 6250–6261, Dec. 2017, doi: 10.1109/TAP.2017.2740963.
- [60] D. Rutledge and M. Muha, "Imaging antenna arrays," *IEEE Transactions on Antennas and Propagation*, vol. 30, no. 4, pp. 535–540, Jul. 1982, doi: 10.1109/TAP.1982.1142856.
- [61] G. L. Charvat, L. C. Kempel, E. J. Rothwell, C. M. Coleman, and E. L. Mokole, "A Through-Dielectric Ultrawideband (UWB) Switched-Antenna-Array Radar Imaging System," *IEEE Transactions on Antennas and Propagation*, vol. 60, no. 11, pp. 5495–5500, Nov. 2012, doi: 10.1109/TAP.2012.2207663.
- [62] C. Ma, T. S. Yeo, Q. Zhang, H. S. Tan, and J. Wang, "Three-Dimensional ISAR Imaging Based on Antenna Array," *IEEE Transactions on Geoscience and Remote Sensing*, vol. 46, no. 2, pp. 504–515, Feb. 2008, doi: 10.1109/TGRS.2007.909946.
- [63] L. Stark, "Microwave theory of phased-array antennas—A review," *Proceedings of the IEEE*, vol. 62, no. 12, pp. 1661–1701, Dec. 1974, doi: 10.1109/PROC.1974.9685.
- [64] C. Balanis, *Antenna Theory Analysis and Design*, 3rd ed. Accessed: Apr. 16, 2023. [Online].
- [65] K. Y. Kapusuz and U. Oguz, "Millimeter wave phased array antenna for modern wireless communication systems," in *2016 10th European Conference on Antennas and Propagation (EuCAP)*, Apr. 2016, pp. 1–4. doi: 10.1109/EuCAP.2016.7481805.
- [66] N. Ojaroudiparchin, M. Shen, and G. F. Pedersen, "Low-cost planar MM-wave phased array antenna for use in mobile satellite (MSAT) platforms," in *2015 23rd Telecommunications Forum Telfor (TELFOR)*, Nov. 2015, pp. 528–531. doi: 10.1109/TELFOR.2015.7377522.
- [67] Z. Briqech, A.-R. Sebak, and T. A. Denidni, "Low-Cost Wideband mm-Wave Phased Array Using the Piezoelectric Transducer for 5G Applications," *IEEE Transactions on Antennas and Propagation*, vol. 65, no. 12, pp. 6403–6412, Dec. 2017, doi: 10.1109/TAP.2017.2730239.
- [68] X. Li and M. Jarrahi, "A 63-Pixel Plasmonic Photoconductive Terahertz Focal-Plane Array," in *2020 IEEE/MTT-S International Microwave Symposium (IMS)*, Aug. 2020, pp. 91–94. doi: 10.1109/IMS30576.2020.9224022.
- [69] N. T. Yardimci and M. Jarrahi, "High Sensitivity Terahertz Detection through Large-Area Plasmonic Nano-Antenna Arrays," *Sci Rep*, vol. 7, no. 1, Art. no. 1, Feb. 2017, doi: 10.1038/srep42667.

- [70] A. Brahm *et al.*, “Multichannel terahertz time-domain spectroscopy system at 1030 nm excitation wavelength,” *Opt. Express, OE*, vol. 22, no. 11, pp. 12982–12993, Jun. 2014, doi: 10.1364/OE.22.012982.
- [71] B. Pradarutti *et al.*, “Terahertz line detection by a microlens array coupled photoconductive antenna array,” *Opt. Express, OE*, vol. 16, no. 22, pp. 18443–18450, Oct. 2008, doi: 10.1364/OE.16.018443.
- [72] R. Henri *et al.*, “Fabrication and Characterization of an  $8 \times 8$  Terahertz Photoconductive Antenna Array for Spatially Resolved Time Domain Spectroscopy and Imaging Applications,” *IEEE Access*, vol. 9, pp. 117691–117702, 2021, doi: 10.1109/ACCESS.2021.3106227.
- [73] W. L. Chan, H.-T. Chen, A. J. Taylor, I. Brener, M. J. Cich, and D. M. Mittleman, “A spatial light modulator for terahertz beams,” *Appl. Phys. Lett.*, vol. 94, no. 21, p. 213511, May 2009.
- [74] K. L. Vodopyanov *et al.*, “Terahertz-wave generation in quasi-phase-matched GaAs,” *Appl. Phys. Lett.*, vol. 89, no. 14, p. 141119, Oct. 2006, doi: 10.1063/1.2357551.
- [75] C. Kittel, *Introduction to solid state physics*, 8th ed. Hoboken, NJ: Wiley, 2005.

## Appendix A: LT-GaAs Optical Pump THz Probe Measurements

Dr. Han performed measurements of the carrier density, carrier lifetime, and mobility of the LT-GaAs samples used throughout the fabrication process in this work under the direction of Dr. Mittendorff within the department of physics at the University of Duisburg-Essen in Duisburg, Germany. The optical pump THz probe system used for these measurements is shown below and follow a similar process to that found in [12].

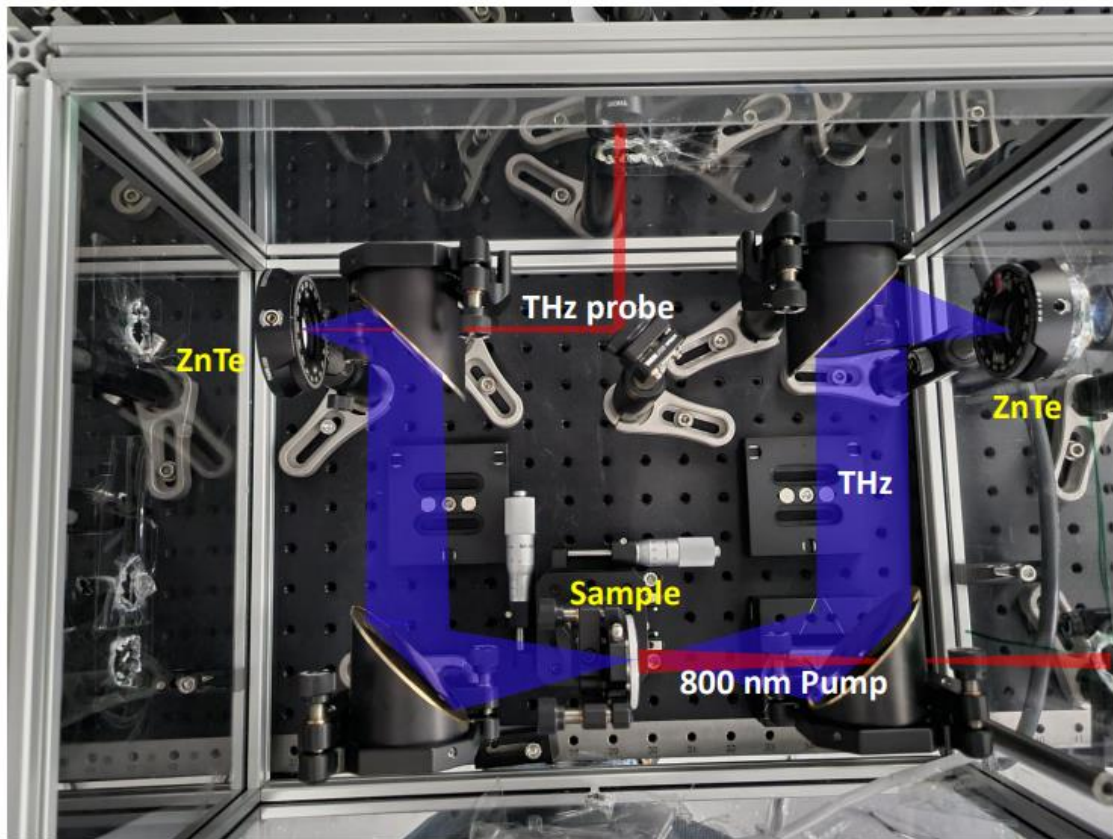


Figure A-1: Optical Pump THz Probe System Setup.

The results per wafer from the pump probe system are shown below. The Drude model is used to calculate the carrier lifetime and mobility based on these results and will be briefly explained later.

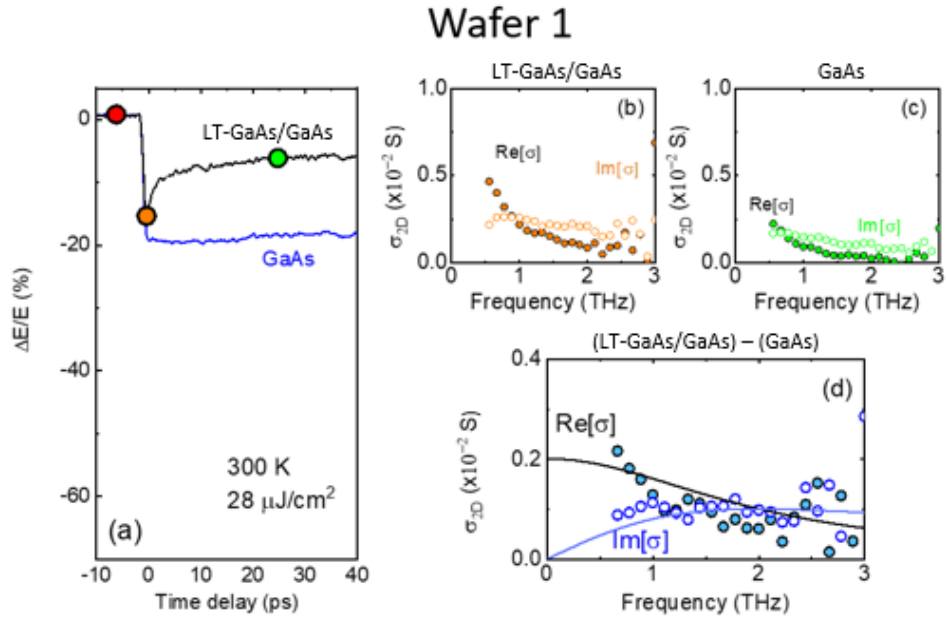


Figure A-2: LT-GaAs wafer 1 pump-probe results.

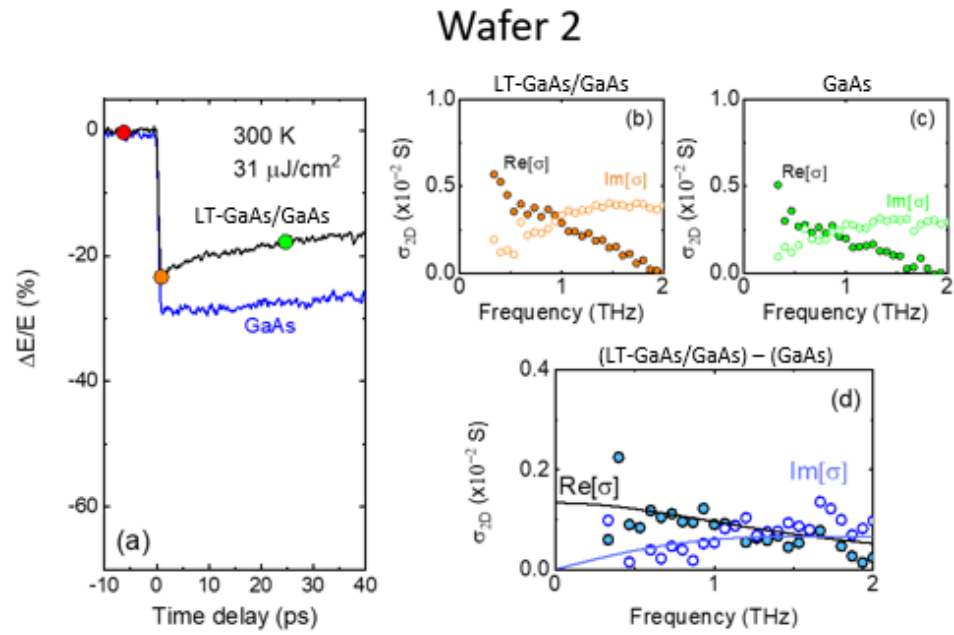


Figure A-3: LT-GaAs wafer 2 pump-probe results.



From the data collected during the pump probe experiments in (a) of both figures, the complex conductivity can be extracted by taking the fast fourier transform (FFT) of both blue (GaAs alone) and black (LT-GaAs sample grown on GaAs) curves, then using the following equation for conductivity of thin films given as:

$$\frac{E_{pump}}{E_0} = \frac{1 + n_{GaAs}}{1 + n_{GaAs} + Z_0 \sigma_{2D}} \quad \text{Equation A-1}$$

Where  $n_{GaAs}$  is the refractive index of GaAs in the THz range given as 3.6 in [74], and  $Z_0$  is the well-known impedance of free space,  $377\Omega$ . Using equation A-1, the real and imaginary values for conductivity can be found, and are plotted in (b) and (c) of both figures. The difference between the two curves is taken to isolate the conductivity of the LT-GaAs layer, shown as the blue data in (d) of both figures.

Next, the Drude model for optical conductivity using both real and imaginary values can be used to calculate the carrier concentration,  $n$ , and carrier lifetime  $\tau$  using equation A-2.

$$\sigma_{2D} = \frac{ne^2}{m^*} \cdot \frac{\tau}{1 - j\omega\tau} \text{ (S)} \quad \text{Equation A-2}$$

Where  $m^*$  is the effective mass of GaAs given as  $0.066m_e$  in [75]. Once  $\tau$  is found, the mobility can be calculated using equation A-3.

$$\mu = \frac{\tau e}{m^*} \left( \frac{cm^2}{Vs} \right) \quad \text{Equation A-3}$$

The resulting parameters for wafers one and two are presented in the table below.

Table 3: LT-GaAs Pump Probe Results

	<b>n (1/cm<sup>2</sup>)</b>	<b>Mobility (cm<sup>2</sup>/(V*s))</b>	<b>Carrier Lifetime (ps)</b>
<b>Wafer 1</b>	$5.9 \times 10^{12} \pm 6 \times 10^{11}$	$2100 \pm 350$	0.7
<b>Wafer 2</b>	$3.1 \times 10^{12} \pm 2 \times 10^{11}$	$2650 \pm 220$	1.5

## Appendix B: Black Phosphorus THz PCA Measurements

This main focus of this work was to fabricate and measure LT-GaAs references devices so with an identical design to BP devices in order to compare the performance of the two materials. All fabrication work related to BP emitters was completed by Dr. Hugh Churchill's group, while the measurements of these devices were done using the TeraAlign system and are part of this thesis work. Two separate devices are measured here, with the results shown below. It should be noted that the incident laser power used in all cases is 3 mW, which is half that of LT-GaAs. This is done as BP is a much more sensitive material, and higher laser powers increases the risk of damaging the devices. For the bias voltage, the device begins at 0.24 V, which corresponds to 10 V after the transformer, and is swept in increments of 5 V after the transformer up to ~30 V, which is about half that of LT-GaAs device, which are biased at 63 V. This is again done in order to preserve the devices and lower the risk of destroying them. Further, no pinhole measurements are done due to the majority of the output spectrum being under 1 THz, causing the pinholes to cut the majority of the signal, making alignment extremely difficult.

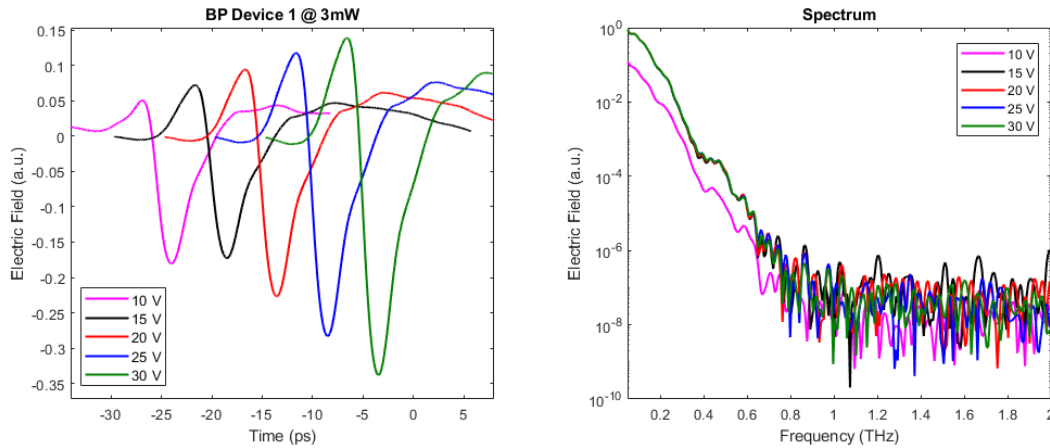


Figure B-1: Time domain and spectrum of BP device 1.

In the plot above it can be seen that the time-domain signal of the BP devices behave similarly to that of LT-GaAs devices, increasing approximately linearly through the range of bias voltages tested. In spectrum, the 10 V measurement is substantially smaller than all other measurements, which are all nearly identical, laying on top of each other. This shows that beginning at 15 V, increasing the bias voltage makes very little difference in the spectrum of the device. The spectrum of the BP device 1 does not reach 1 THz in any measurements. Below, the second BP device can be seen plotted in the same way as device 1.

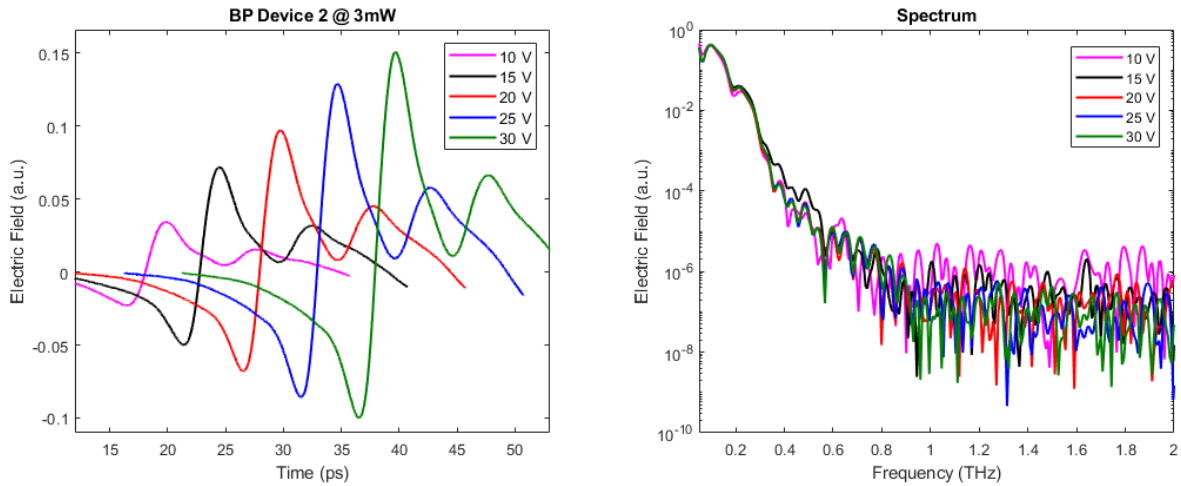


Figure B-2: Time domain and spectrum of BP device 2.

Like the first BP device, a near linear relationship is observed in the time-domain signal of the BP devices. However, in this case, the 10 V bias measurement does not have a substantially lower spectrum. Overall, the current BP devices are not performing at the same level as LT-GaAs, even with the lower bias voltage and laser power.

## Appendix C: Additional LT-GaAs Antenna Array Measurements

In order to provide more comprehensive data relating to the two element arrays described in this work, additional devices were fabricated and measured to see if consistent results would be observed. Below, three sets of plots can be seen showing measurements of the same three array spacings outlined earlier, that is, 75-, 150-, and 300-microns.

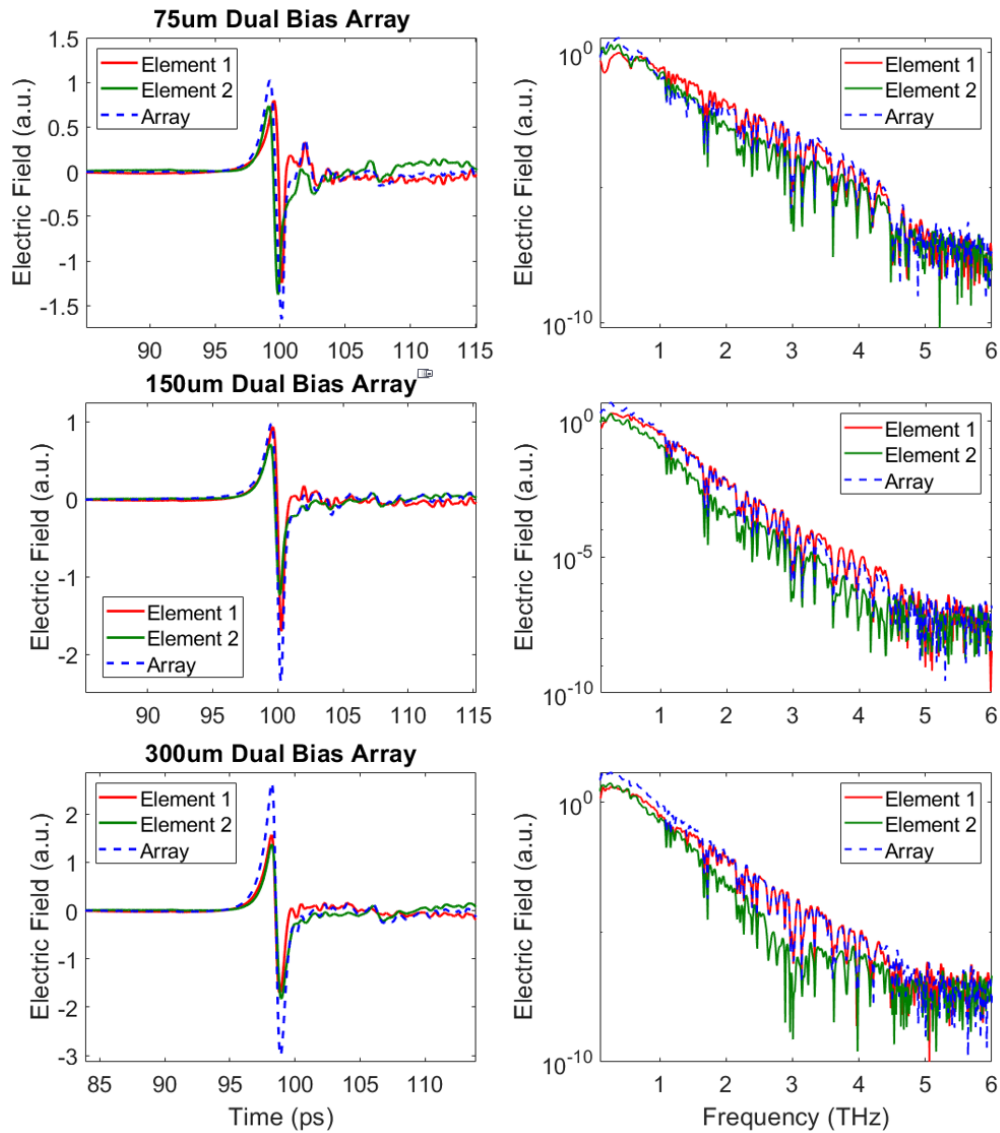


Figure C-1: Time domain and spectrum of THz Arrays.

This figure shows a similar result to what was discussed in chapter 4 of this thesis. It can be observed that in all cases, the array signal is greater than that of the individual elements. However, in the case of these measurements, the signal amplitudes are much closer to each other than what was shown previously. This further supports the conclusion that the difference in amplitude between the devices previously was due to differences in material. All of the devices shown above in figure C-1 were fabricated from the same material as the devices in chapter 4 of this work.